CONJUGATE HEAT TRANSFER AND THERMO-STRUCTURAL ANALYSIS OF THE ACTIVELY COOLED MULTI-STAGE CONICAL NOZZLE AND HYPERSONIC LOW-REYNOLDS DIFFUSER OF THE NEW ARC-HEATED WIND TUNNEL (AWHT-II) OF THE UNIVERSITY OF TEXAS AT ARLINGTON

by

DAVID R CAMPBELL

Presented to the Faculty of the Graduate School of

The University of Texas at Arlington in Partial Fulfillment

of the Requirements

for the Degree of

MASTER OF SCIENCE IN AEROSPACE ENGINEERING

THE UNIVERSITY OF TEXAS AT ARLINGTON

MAY 2017

Acknowledgements

I would like to first thank my supervising Professor Dr. Luca Maddalena for giving me the opportunity to work on such a complex and prestigious project, for continuously challenging me to do better and become a stronger engineer, and for mentoring me in the complex realm of hypersonic aerodynamics and testing. To Dr. Stefano Gulli, thank you for being such a great colleague, for performing independent review of all my work, for being a supportive mentor at the Aerodynamics Research Center, and for putting up with me the past three years. To Dr. Fabrizio Vergine, thank you for educating me in fluid dynamics and challenging me to prove the validity of my work, and also being a friend and mentor at the Aerodynamics Research Center. I would also like to thank Kermit Beird, for his support in initial design, for his budgetary estimations, for reviewing all my manufacturing drawings, and for being a mentor for me for years in manufacturing and machining. Lastly I would like to thank my family, especially my mother and father. While it was a long and tumultuous ride, it is because of your guidance and support that I was able to achieve everything that I have at this point. I love you and thank you for sticking through it all with me.

May 19, 2017

Abstract

CONJUGATE HEAT TRANSFER AND THERMO-STRUCTURAL ANALYSIS OF THE ACTIVELY COOLED MULTI-STAGE CONICAL NOZZLE AND HYPERSONIC LOW-REYNOLDS DIFFUSER OF THE NEW ARC-HEATED WIND TUNNEL (AWHT-II) OF THE UNIVERSITY OF TEXAS AT ARLINGTON

David Campbell, MS

The University of Texas at Arlington, 2017

Supervising Professor: Dr. Luca Maddalena

Arc-heated wind tunnels are the primary test facility for screening and qualification of candidate materials for hypersonic thermal protection systems (TPS). Via an electric arc that largely augments the enthalpy (by tens of MJ/kg) of the working fluid (Air, Nitrogen, CO2 in case of Mars-entry studies) passed through a converging-diverging nozzle at specific stagnation conditions, different regimes encountered in entry and re-entry hypersonic aerothermodynamics can be simulated.

Because of the high-enthalpies (and associated temperatures that generally exceed the limits required by the thermo-structural integrity of the facility) the active cooling of the arc-heated wind tunnel's parts exposed to the working gas is

critical. This criticality is particularly severe in these facilities due to the time scales associated with their continuous operation capabilities (order of minutes).

This research focuses on the design and the conjugate heat transfer and resultant thermo-structural analysis of a multi-segment nozzle and low-Reynolds, hypersonic diffuser for the new arc-heated wind tunnel (AHWT-II) of the University of Texas at Arlington. Nozzles and hypersonic diffusers are critical components that experience highly complex flows (non-equilibrium aerothermochemistry) and high (local and distributed) heat-flux loads which significantly augment the complexity of the problems associated with their thermal management.

The proper design and thermo-mechanical analysis of these components are crucial elements for the operability of the new facility.

This work is centered on the design considerations, methodologies and the detailed analysis of the aforementioned components which resulted in the definition of final parts and assemblies that are under manufacturing at this writing. The project is jointly sponsored by the Office of Naval Research (ONR) and the Defense Advanced Research Project Agency (DARPA).

Table of Contents

List of Illustrations

List of Tables

Chapter 1 Brief Overview of Hypersonic Flows and the Need for Arc-Heated Wind Tunnels

Hypersonic vehicles and planetary entry and re-entry probes are exposed to a complex flow regime that requires experimental screening and qualification. These vehicles require consideration of not only aerodynamics but also thermal management due to the high stagnation enthalpy (and thus vehicle surface temperatures) as observed in the reference system of the vehicle. In these conditions, the flow is generally in complex forms of thermo-chemical non-equilibrium.

To protect entry, re-entry and hypersonic cruise vehicles from the extreme heat loads of the hypersonic flight regime, these vehicles necessitate appropriate Thermal Protection Systems (TPS), protective materials that mitigate the heat flux and the heat load into the body of the vehicle by multiple means of rejection or resistance. The aero-thermodynamic effects experienced by these vehicles are not easy to simulate due to the complex flow physics. Lack of modeling and uncertainties even in the most accurate computational fluid dynamics analysis can result in catastrophic failure in practice.

Shown in Figure 1.1 the X-15, the first hypersonic vehicle, achieved a maximum speed of Mach 6.7 during its flight testing regime and paved the way for understanding of hypersonic flow and their thermo-structural effects. After its fastest hypersonic flights the X-15 showed extensive degradation and failure in

some cases of the Inconel skin, as shown in Figure 1.2, which was intended to withstand the aerodynamic heating. As such, facility simulation of fluid kinetics

Figure 1.1: X-15 after launch from B-52 with rockets ignited [1].

Figure 1.2: X-15 Lower Pylon damage due to localized heat flux [2].

and chemistry of hypersonic flow was required to legitimize designs and candidate materials before full scale testing. Beginning in the 1950's the United States began developing facilities for experimentally characterizing hypersonic flow and validating vehicle designs. While no single facility can fully simulate all aspects of hypersonic flight, certain facilities are capable of simulating one or more of the primary flow considerations involved in hypersonic flight. Facilities such as shock tunnels can simulate aerodynamic characteristics of models, but due to their short run times (milliseconds) they are incapable of analyzing thermo-structural conditions experienced during atmospheric entry or extended hypersonic flight. To simulate the long duration high enthalpy flows (aerothermal heating) experienced

by vehicles while in the hypersonic regime, there is one primary facility type that has been prevalent in experimental investigation and verification of materials for thermal protection systems.

Arc-heated wind tunnels (AHWT) embody the fundamental ground test facility for experimental qualification of TPS materials. Indeed, extremely high enthalpies, duplicating re-entry heating, are possible in arc jets. However this facility type is limited in dynamic pressure. These facilities may produce flow contaminants or have non-uniform flow characteristics due to coring effects (centerline enthalpy higher than the surrounding as exiting the nozzle) that has to be taken into consideration, case by case, depending on the scope and the type of a specific investigation [3]. Even with these considerations, arc-heated wind tunnels serve as the primary method for screening and qualification of materials due to the capacity of the systems to provide the high enthalpy for an extended period of time on the order of tens of minutes.

Arc-heated wind tunnel facilities can range extensively in enthalpy and size. One of the largest facilities in the world is the CIRA Scirocco Plasma Wind Tunnel (PWT) which is capable of nozzle exit velocities of up to 7 km/sec at an enthalpy of 70 MJ/kg [3]. Scirocco is equipped with a 5.5 meter long segmented constricted type arc heater with an internal flow cavity diameter of 0.11 meters and it is capable of mass flows ranging between 0.2 kg/sec and 3.5 kg/sec with a plenum pressure up to 87 bar, which produces stagnation temperatures between 2,000 and 10,000

Kelvin [4]. The other arc heater at CIRA is named Ghibli and is equipped with a 2 MW segmented constrictor arc heater with stagnation heat fluxes ranging between 0.2 MW/m^2 and 1.3 MW/m^2 at mass flow rates of air 0.043-0.112 kg/sec and stagnation pressures 3-175 mbar [5]. The size and operational range of the Ghibli facility is very similar to the sizing of the arc-heated wind tunnel upgrade underway at the University of Texas at Arlington. There are two facilities in Germany at the DLR research center, L2K and L3K, which are 1 MW and 6 MW facilities respectively; L2K is a huels-type arc-heater capable of cold wall heat flux of 2 MW/m^2 and pitot-tube pressures up to 16 kPa, while the L3K is segmented constrictor arc-heater capable of cold wall heat flux up to 4 MW/ m^2 at pitot-tube pressures up to 35 kPa and total temperatures 4000-7000 K [4]. There are other smaller facilities in Japan and France, but the rest of the major facilities around the world are in the United States and operated by NASA and the Air Force.

The arc-heater L-CAT owned by Boeing is the only commercially owned facility in the United States, and the rest of the arc-heaters are owned and operated by the government. The major facilities that operate Arc heaters are the NASA Ames arc-jet complex, NASA Langley, and Arnold Engineering Development Center (AEDC). The Ames arc-jet complex consists of 4 arc-heaters, the Aerodynamic Heating Facility (AHF), the Interactive Heating Facility (IHF), the Turbulent Flow Duct facility (TFD), and the Panel Test Facility (PTF), with the largest power supply for the facility being capable of producing 75 MW for 30

minutes or 150 MW for 15 seconds [4]. The Interactive Heating Facility, the largest facility at Ames, is a 60 MW arc-heater capable of run times up to an hour for stagnation and flat plate test specimen configurations [4]. The Panel Test Facility uses a semi-elliptic nozzle to develop flow for test panels, and is powered by a 20 MW arc-heater that can operate for up to 20 minutes; the turbulent flow duct is also powered by a 20 MW arc heater and is designed to test flat surfaces (not flat panels at an angle) [4]. Finally, the Aerodynamic Heating Facility can be connected using either a 20 MW huels type or a segmented constrictor arc-heater, and is capable of ascent and high speed flight conditions as well as catalycity studies, and has a rotating multi-specimen arm capable of efficiency of operation [4]. The NASA Langley arc-heater is a 2.1 MW huels-type system with four interchangeable nozzles ranging from 5 cm to 50 cm; the enthalpy range of the Langley facility is 2790-27900 kJ/kg and combined with the nozzle results in heat fluxes from 17-1700 W/cm^2 [6]. The Hypersonic Materials Environmental Test System (HYMETS) at NASA Langley is a 400 kW arc-heated wind tunnel capable of bulk enthalpies between 6.4 MJ/kg and 18.4 MJ/kg, and the working fluid can be changed to simulate Earth re-entry or Martian atmospheric entry [7]. The HYMETS arc-heater is similar in operational range to the upgrade to the University of Texas at Arlington arc-heated wind tunnel as well as the Ghibli facility, but the sample sizes are limited to around an inch. The AEDC facility consists of three arc-heaters, H1, H2 and H3. H1 and H3 are segmented arc-heaters while H2 is a huels-type arc-

heater. H1 is a 24 MW arc-heater that is capable of plenum pressures of 120 atm, providing high operating pressures and stagnation enthalpies; H3 is a 50% larger scale version of H1 capable of double the power and mass flow rate, with plenum pressures up to 150 atm [4]. The H3 facility is generally designed for full-scale samples for missiles and re-entry vehicles. H2 is capable of Mach 5-9 with pressure altitudes up to 120 atm and run times over 20 minutes [4]. While the range and capacities of these facilities is extensive, all of the government owned facilities were built decades ago, and as such upgrades have been performed to accommodate modern technology and instrumentation.

Arc-heated wind tunnels superheat high pressure fluid to a specific stagnation enthalpy and pass it through a converging-diverging nozzle to accelerate the flow. By energizing the flow entering the nozzle of the test system, the flow at the exit of the nozzle can closely emulate the hypersonic flow regime at a wide range of velocities and altitudes of flight based upon the input energy to the system (electrical power at the net of the cooling losses), the stagnation pressure, the nozzle Mach number and the test section pressure. The combination of these choices results in the establishment of flow conditions for a specific arc-heated wind tunnel test.

Due to the substantial enthalpy of the flow contained within an arc-heated wind tunnel, between 5-70 MJ/kg, significant cooling is required to maintain material structural integrity and system reusability [3]. As such, the systems are

generally made of metals with high thermal conductivity to improve thermal distribution within the material, and actively cooled by fluids. Copper alloys are common internal material on nozzles due to their ability to transfer heat and avoid hot spots through dissipation, and water (or de-ionized water) is commonly used as a cooling fluid due to its high thermal conductivity and abundancy.

This research focuses on the design and the conjugate heat transfer and resultant thermo-structural analysis of a multi-segment nozzle and low-Reynolds, hypersonic diffuser for the new arc-heated wind tunnel (AHWT-II) of the University of Texas at Arlington. Nozzles and hypersonic diffusers are critical components that experience highly complex flows (non-equilibrium aerothermochemistry) and high (local and distributed) heat-flux loads which significantly augment the complexity of the problems associated with their thermal management. The proper design and thermo-mechanical analysis of these components are crucial elements for the operability of the new facility.

This work is centered on the design considerations, methodologies and the detailed analysis of the aforementioned components which resulted in the definition of final parts and assemblies that are under manufacturing at this writing. The project is jointly sponsored by the Office of Naval Research (ONR) and the Defense Advanced Research Project Agency (DARPA).

Chapter 2

Overview of the University of Texas at Arlington Arc-Heated Wind Tunnel

The current 1.6 MW Arc-heated wind tunnel facility at the University of Texas at Arlington is comprised of the arc-heater, test section, diffuser, vacuum tank, vacuum pump, ejector pump and silencer. The various systems are shown in Figures 2.1 and 2.2 respectively.

Figure 2.1: UT Arlington arc-heated wind tunnel facility, indoor components.

Figure 2.1 shows the arc-heater and test section, with the cooling pipes to the arc-heater visible along the ground (stainless braided lines and solid stainless pipes), the working gas injection line (bright orange line on the left running to the arc-heater body) and the power supply lines hanging on the left side of the system (brown lines on the left). Figure 2.2 shows the cooling-system centrifugal pump and motor (bottom left), the cooling fluid supply tank (middle left, silver), the large vacuum tank (center, blue), the Halmar 1.6 MW DC power supply (right, white), and the silencer (far right, light brown).

Figure 2.2: UT Arlington arc-heated wind tunnel; current outdoor components.

The arc-heater body is a Thermal Dynamics F-5000 Huels-type arc-heater donated to the University by the United States Air Force Arnold Engineering Development Center (AEDC). The arc-heater was originally designed for a

nominal 2 MW power supply, and was upgraded at AEDC to increase the power rating to 3 MW [9]. The cross-sectional view of the Thermal Dynamics F-5000 arc-heater is shown in Figure 2.3. The internal bodies of the arc-heater including the anode, cathode and plenum bodies are made of Beryllium Copper, with the outer housings being composed of Brass. The anode and cathode bodies are electrically isolated using a boron nitride insulator [9]. A rotating electric arc is generated within the anode body near the plenum entrance and moves circumferentially along the body based upon the vortical fluid flow and local electrical resistance of the anode which varies with heating. The arc does not normally directly interact with the cathode body and instead is concentrated at the cathode tip at the base of the cathode barrel although at times the arc will jump to the cathode body temporarily,

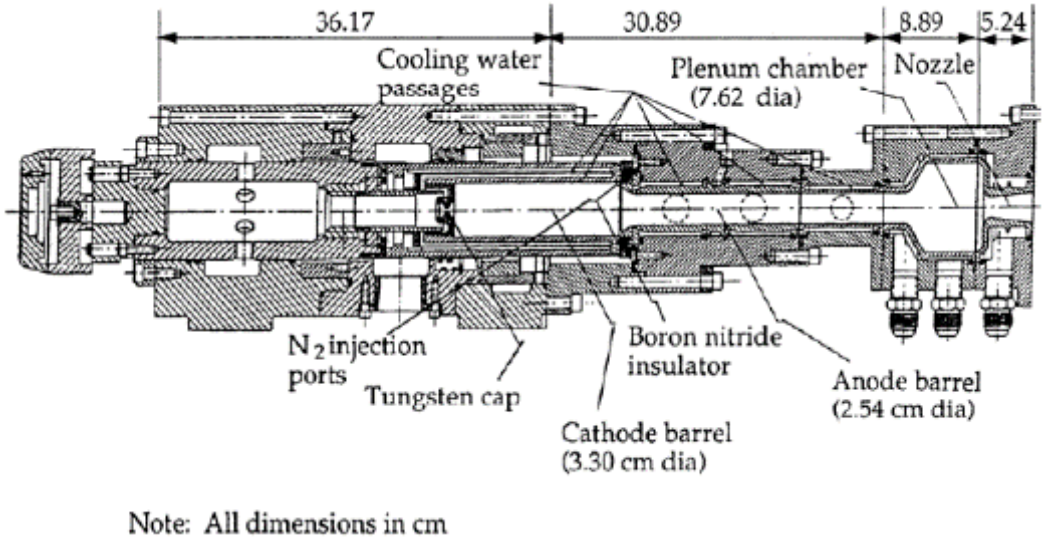

Figure 2.3: Cross Sectional View of Thermal Dynamics F-5000 arc-heater [10].

which is acceptable because the cathode section is electrically floating. The anode section, along with the downstream components, are grounded [10]. The tip of the

cathode, to which the arc is generated from the anode body, is made of thoriated tungsten to withstand the high temperatures of the electric arc generated at a localized point since the arc is constantly concentrated at this location. While the thoriated tungsten does help withstand the high temperature of the isolated arc connection point, there is still degradation over time, which is one of the sources of flow contaminants mentioned in the introduction. To assist in the stabilization and rotation of the arc the working fluid, nitrogen, is tangentially injected through a swirl plate at the anode-cathode interface to create a strong vortical flowfield [8].

The current arc-heater system is capable of operating with mass flow rates between 0.07-0.18 kg/sec for run times of up to 200 seconds [9]. These upper and lower limits are defined based upon the range within which the arc remains stable even with the effects of the vortical flowfield, and is strongly based upon the range of pressure and stagnation enthalpies that the system can support without damaging primary internal components. The arc-heater also has the capability to inject other fluids downstream of the primary tangential injection plate in the anode barrel to create fluid mixtures preceding the plenum and nozzle segment. The most common fluid injected downstream to create a mixture is oxygen- by injecting the proper mass flow rate of oxygen the partial pressures of nitrogen and oxygen can be established to simulate atmospheric conditions. Other gases however can also be injected to simulate the effects of hydrocarbon or hydrogen supersonic combustors [9].

A 1.6 MW DC Halmar (the company is now Robicon) power supply was purchased to power the arc-heater at UT Arlington. The power supply converts 2400 volt AC input to a steady state voltage of 2000 volts at 800 amps [10]. It is capable of providing a maximum DC voltage of 2650 volts [9]. The plasma interface board, the main control board for the Halmar, makes dynamic adjustments to hold the arc steady by regulating current, which is not naturally stable, within ±1 percent of full-scale output within the intended system operating range [9]. To initiate the flow through the nozzle and establish the arc, the system uses a lower power setting and Argon injection initially instead of Nitrogen due to its lower ionization potential. Upon the establishment of the stable arc, the flow is switched to Nitrogen or the fluid mixture, and the power of the system is increased to the necessary value to simulate the flow intended for the test.

The current test section of the AHWT is an axially cylindrical pressure vessel with a diameter and length of 76.2 centimeters [9]. The current test section is water cooled by coils soldered to the surface of the test section due to its small volume [10]. The radiative and convective heat fluxes through the system result in significant heating of the test section, thus requiring cooling. The flow then enters two constant area diffusers before entering a 4.25 m^3 vacuum tank, to a supersonic ejector pump. The cooling of the system is critical and utilizes a 340 psi, 400 GPM centrifugal pump distributed to the anode, cathode, plenum, nozzle, test section and diffuser entrance. The cooling fluid is pumped through a primary Alfa-Laval

M10MFM plate heat exchanger, which exchanges heat with a secondary low pressure cooling fluid loop connected to an air-water chilling tower present at the Aerodynamics Research Center [9].

The current facility design is limited by several factors. The capacity for the system to reduce back pressure creates limitations on attainable test conditions (low Mach and 1 inch test article). Additionally, the size of the test section limits non-intrusive diagnostics and test durations

Upon the award of a grant by the Office of Naval Research and the Defense Advanced Research Project Agency to Prof. Maddalena' s research group, the facility upgrade was initiated to largely improve the performance envelope and capabilities of the entire system. For the upgrade to the AHWT facility at UT Arlington, the systems that will remain are the arc-heater body, the centrifugal pump, the Alfa-Laval M10MFM plate heat exchanger, and the chilling tower that serves the main compressor of the aerodynamics research center as well. The original nozzle, the test section, the diffuser, the vacuum tank and the vacuum pump will be removed and replaced with updated assemblies that will increase the facility operational envelope. A model of the new facility (AHWT-II) is shown in Figure 2.4. The current nozzle will be replaced by a three-stage conical nozzle assembly capable of nominal Mach 2.5, Mach 4, and Mach 6.5 flows. These nozzle segments

combine into the full nozzle assembly, shown in Figure 2.5.

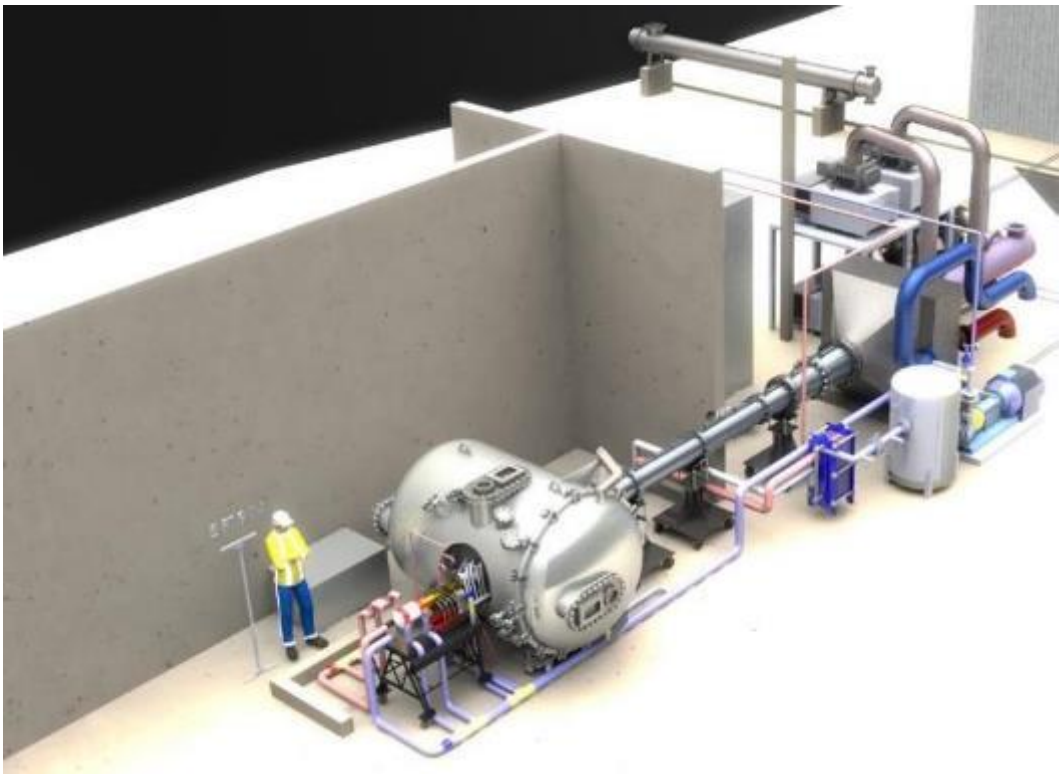

Figure 2.4: Upgraded arc-heated wind tunnel facility assembly.

The current test section will be replaced by a 1.8 meter diameter, 2 meter length transverse test section with multiple lateral and stagnation viewports, as well as a sliding rail and rotary test sample systems which allow for multiple sample tests, along with characterization of the flow during each run. The size of the test section was carefully chosen to remove the requirement for an active cooling system, since the newly actively-cooled flanges for the nozzle will be able to intercept the large majority of the radiative heat.

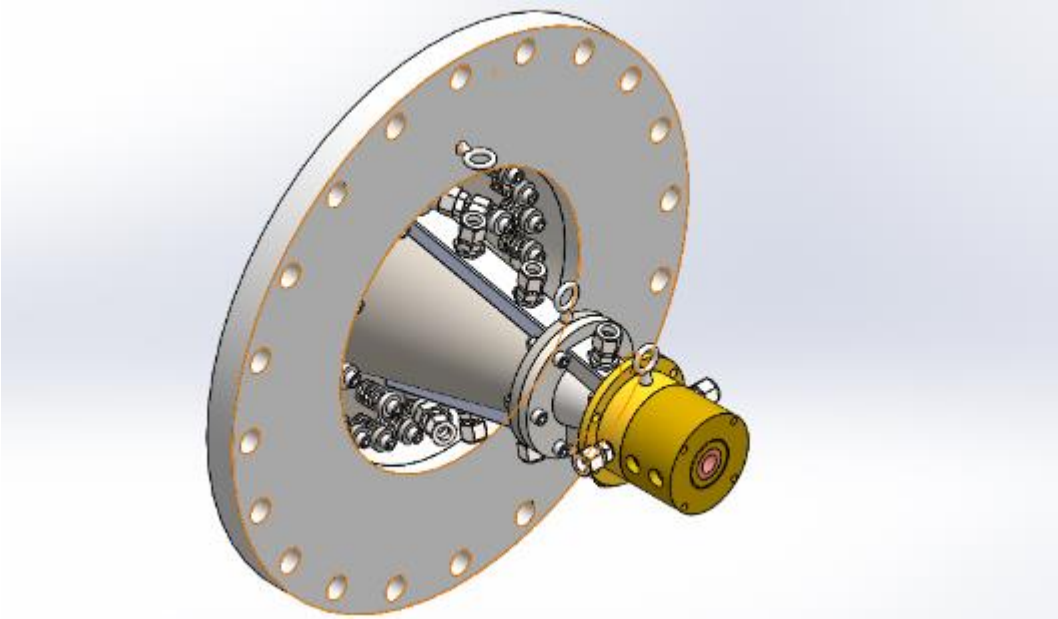

Figure 2.5: Three-stage configuration of the Conical Nozzle Assembly.

The original straight pipe diffuser will be replaced by a converging diverging diffuser system with catch cone, throat and exit segments designed for pressure recovery to assist in the vacuum system. The new hypersonic diffuser assembly is shown in Figure 2.6. The diffuser is divided into segments as shown to allow for manufacturability of the system.

The diffuser will lead into a working gas-to-liquid tube heat exchanger with a secondary heat exchanger attached to the existing chilling tower. Once the flow temperature is reduced to near ambient temperature by the heat exchanger, the flow will then pass into a vacuum manifold and processed by a vacuum-pump system. The updated system will be nominally capable of sustaining test-section nominal pressures equivalent to an altitude of 50 km or above.

Figure 2.6: UT Arlington AHWT-II upgraded diffuser assembly.

The comparison with some other arc-heated wind tunnels in the United States the current facility nominal performance in an altitude/enthalpy (velocity) map is shown in Figure 2.7.The shakedown of the new facility, once assembled, will allow to determine the operational envelope of the upgrade facility (AHWT-II) .

Upon the establishment of the primary, nominal, performance requirements of the facility, the modeling of selected off-design conditions was considered for analysis. The models shown in Figures 2.5 and 2.6 were developed very carefully to match the requirements of the internal geometry and necessary cooling fluid systems that will be discussed in great detail in the subsequent chapters.

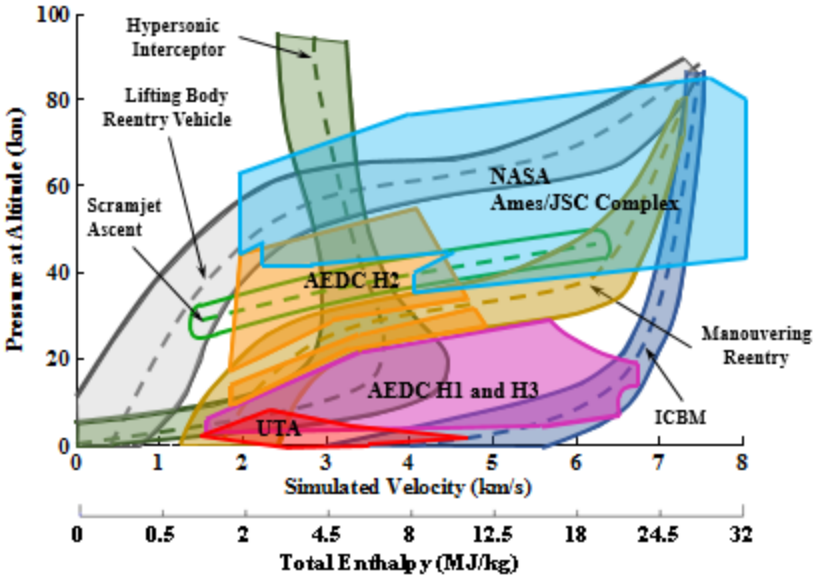

Figure 2.7: Nominal Theoretical Altitude/Velocity Map of the old UT Arlington Arc heated wind tunnel respect to some other arc heated wind tunnel facilities (used with permission of Prof. Maddalena's research group).

Once the CAD models were developed, the assemblies were used for the analysis using Solidworks Flow Simulation. The details of the solver are briefly described in Chapter 3.

Chapter 3

Solidworks Flow Simulation: Governing Equations, Boundary Condition and Numerical Solution Techniques

To solve fluid systems of both laminar and turbulent flow, Solidworks Flow Simulation solves the Navier-Stokes equations [11]. The conservation of mass and the momentum equation (one vectorial or equivalently 3 scalar equations) are not sufficient alone to solve the flow as the number of unknowns is larger than the number of equations. Specifically an equation of state as well as specific thermophysical properties of the fluids must be included. The solution of the aforementioned system of equations is univocally determined by the application of case-dependent appropriate boundary and initial conditions.

Solidworks Flow Simulation is capable of simulating both laminar and turbulent flows. The difference between the laminar and turbulent equations is the inclusion of the Reynold's Stress tensor (which is null in laminar flows). The decision upon whether laminar or turbulent flow has to be considered at a specific location or cell is based upon localized Reynolds numbers, calculated using the local velocity, a characteristic length and the kinematic viscosity. While for the laminar case, the general Navier-Stokes equations, in their essential form, can be directly used coupled with the fluid state equation, the turbulent case requires a modification to the equations to incorporate the effects of turbulence. Specifically, in this case the Favre-averaged Navier-Stokes equations are used for turbulent

flows. As the averaging process introduces additional unknowns, new equations are needed (the closure problem). Flow Simulation uses formulations based on turbulence kinetic energy and a length scale, specifically the $k-\varepsilon$ model [11].

The equations for conservation of mass, momentum and energy used in the calculations of Flow Simulation for the low speed case of a Newtonian Fluid, as listed in the Solidworks Flow Simulation technical reference [11], are as follows:

$$\frac{\partial \rho}{\partial t}+\frac{\partial}{\partial x_i}(\rho u_i)=0 \tag{1}$$

$$\frac{\partial}{\partial t}(\rho u_i)+\frac{\partial}{\partial x_j}\left(\rho u_i u_j\right)+\frac{\partial p}{\partial x_i}=\frac{\partial}{\partial x_j}\left(\tau_{ij}+\tau_{ij}^R\right)+S_i \tag{2}$$

$$\frac{\partial \rho H}{\partial t}+\frac{\partial \rho u_i H}{\partial x_j}=\frac{\partial}{\partial x_i}\left(u_j\left(\tau_{ij}+\tau_{ij}^R\right)+q_i\right)+\frac{\partial p}{\partial t}-\tau_{ij}^R\frac{\partial u_i}{\partial x_j}+\rho\varepsilon+S_i u_i+Q_H \tag{3}$$

H, which represents the enthalpy of the flow is quantified by

$$H=h+\frac{u^2}{2} \tag{4}$$

Equations (1)-(3) represent the equations of continuity, momentum and energy for non-chemically-reacting fluids that are relevant for the analysis discussed in this thesis (cooling systems) analysis. The substitution of enthalpy H for energy is acceptable for conditions associated with the flow to be simulated since no changes in fluid state, and no chemical reactions are considered to be occurring. These are the standard Navier-Stokes equations used in all CFD analysis for low Mach number simulations that do not consider chemically-reacting flow, but considering the inclusion of turbulence , the system is still has no solution without further

consideration to define the effects of viscous stresses within the turbulent flow. For Newtonian fluids in Solidworks Flow simulation [11] the following expression is used:

$$\tau_{ij} = \mu\left(\frac{\partial u_i}{\partial x_j} + \frac{\partial u_j}{\partial x_i} - \frac{2}{3}\delta_{ij}\frac{\partial u_k}{\partial x_k}\right) \quad (5)$$

The Reynolds stress tensor for turbulent flows follows the Boussinesq assumptions,

$$\tau_{ij}^{R} = \mu_t\left(\frac{\partial u_i}{\partial x_j} + \frac{\partial u_j}{\partial x_i} - \frac{2}{3}\delta_{ij}\frac{\partial u_k}{\partial x_k}\right) - \frac{2}{3}\rho k\delta_{ij} \quad (6)$$

where δ_{ij} is again the Kronecker delta function (equal to unity when $i = j$ and zero in all other cases), μ_t is the eddy viscosity coefficient, and k is the turbulent kinetic energy [11]. The only difference between the shear stress tensor equation and the Reynolds turbulent stress equation is the substitution of the kinematic viscosity value with the eddy viscosity coefficient μ_t, and the inclusion of the turbulent kinetic energy term. The Boussinesq assumption incorporating the $k - \varepsilon$ turbulence model is a common approach where k represents the turbulent kinetic energy and ε represents turbulent dissipation within the fluid. The eddy viscosity coefficient present within the Boussinesq assumption in Solidworks Flow Simulation is defined as

$$\mu_t = f_\mu \frac{C_\mu \rho k^2}{\varepsilon} \quad (7)$$

Where ε is the turbulent dissipation, $C_\mu$is an empirically defined constant within Solidworks Flow Simulation set as $C_\mu = 0.09$ and the turbulent viscosity factor f_μ is defined as

$$f_\mu = \left[1 - e^{(-0.0165R_y)}\right]^2 * \left(1 + \frac{20.5}{R_T}\right) \quad (8)$$

The turbulent Reynolds number is defined as

$$R_T = \frac{\rho k^2}{\mu\varepsilon} \quad (9)$$

And the boundary layer Reynolds number is defined by

$$R_y = \frac{\rho\sqrt{k}y}{\mu} \quad (10)$$

The equations for R_T and R_y account for transition between laminar and turbulent calculations in flows away from and near wall conditions respectively [11]. The turbulent kinetic energy equations however still have no solution without further equations for k and ε, and as such two further transport equations used in Solidworks Flow Simulation are defined as follows:

$$\frac{\partial\rho k}{\partial t} = \frac{\partial}{\partial x_i}(\rho u_i k) = \frac{\partial}{\partial x_i}\left(\left(\mu + \frac{\mu_t}{\sigma_k}\right)\frac{\partial k}{\partial x_i}\right) + S_k \quad (11)$$

$$\frac{\partial\rho\varepsilon}{\partial t} = \frac{\partial}{\partial x_i}(\rho u_i \varepsilon) = \frac{\partial}{\partial x_i}\left(\left(\mu + \frac{\mu_t}{\sigma_\varepsilon}\right)\frac{\partial \varepsilon}{\partial x_i}\right) + S_\varepsilon \quad (12)$$

Here σ_ε and σ_k are empirical parameters defined as $\sigma_\varepsilon = 1.3$ and $\sigma_k = 1$. These represent the local density variations of the flow due to the implementation of the $k - \varepsilon$ turbulence parameters used in Solidworks Flow Simulation. The source terms

of the equation S_k and S_ε represent the local variations due to turbulent viscosity, which are defined by

$$S_k = \tau_{ij}^R \frac{\partial u_i}{\partial x_j} - \rho\varepsilon + \mu_t P_B \tag{13}$$

and

$$S_\varepsilon = C_{\varepsilon 1} \frac{\varepsilon}{k}\left(f_1 \tau_{ij}^R \frac{\partial u_i}{\partial x_j} + \mu_t C_B P_B\right) - C_{\varepsilon 2} f_2 \frac{\rho\varepsilon^2}{k} \tag{14}$$

respectively [11]. $C_{\varepsilon 1}$ and $C_{\varepsilon 2}$ are empirical constants defined as$C_{\varepsilon 1} = 1.44$ and $C_{\varepsilon 2} = 1.92$. The parameter P_B, representing the turbulent buoyancy equation is defined as

$$P_B = -\frac{g_i}{\sigma_B}\frac{1}{\rho}\frac{\partial \rho}{\partial x_i} \tag{15}$$

with g_i as the gravitational acceleration in direction i, and the constants $\sigma_B = 0.9$ and $C_B = 1$ when $P_B > 0$ and 0 in all other cases [11]. The turbulent buoyancy is critical in this case due to the changes in vertical position due to the fluid travel within the segments, which will be shown later to be significant. The functions f_1 and f_2 presented in equation (14) are represented as

$$f_1 = 1 + \left(\frac{0.05}{f_\mu}\right)^3 \tag{16}$$

and

$$f_2 = 1 - e^{(-R_T^2)} \tag{17}$$

The diffusivity of heat flux is defined by the following equation, where the Lewis number is equal to 1, i.e. $Le = 1$:

$$q_i = \left(\frac{\mu}{Pr} + \frac{\mu_t}{\sigma_c}\right)\frac{\partial h}{\partial x_i} \tag{18}$$

Where σ_c is a constant defined as $\sigma_c = 0.9$. The previous equations and explanations provided for equations (1)-(18) are explicitly taken from the Solidworks Flow Simulation Technical Reference, with some additional explanation interspersed throughout the identification [11].

With the Favre-averaged Navier-Stokes equations defined in equations (1)-(18), the next primary consideration is how the boundary layer of the fluid is modeled near the walls of the system.

A laminar/turbulent boundary layer model is used to describe flows in near-wall regions. The model is based on the so-called Modified Wall Functions approach. This model is employed to characterize laminar and turbulent flows near the walls, and to describe transitions from laminar to turbulent flow and vice versa. If the "thick-boundary-layer" contains 6 or more cells across the boundary layer, and in this case the modified wall functions approach is implemented, but instead of the logarithmic velocity profile the full Van Driest profile is used [11]. If the size of the mesh cell near the wall too large an integral boundary layer technique is used, which in this case is called a "thin-boundary layer", containing 4 or less cells across the boundary layer; the Prandtl boundary layer equations are solved along a fluid

streamline covering the walls [11]. If there are 5 cells across the boundary layer, a combination of the two methods is used.

In this analysis the working fluid is liquid water operating at conditions for which the density of fluid is considered to be a function of temperature only. As a result of this assumption, the viscosity and thermal conductivity of the fluid are also considered to be functions of temperature only. The heat transfer within the fluid has already been defined in equation (3), and the diffusive heat flux was previously defined in equation (18). Solid material thermal conductivity however has yet to be defined. In Solidworks Flow Simulation, the following equation is used:

$$\frac{\partial \rho e}{\partial t} = \frac{\partial}{\partial x_i}\left(\lambda_i \frac{\partial T}{\partial x_i}\right) + Q_H \qquad (19)$$

where e is the specific internal energy, Q_H is the specific heat absorption per unit volume, and λ_i are the eigenvalues of the thermal conductivity tensor, where for isotropic materials all the eigenvalues are equal [11]. The heat flux between the solid/fluid interface is calculated based upon the solid surface temperature and the fluid boundary layer characteristics [11].

Combined the equations (1)-(19) from the Solidworks Flow Simulation technical reference quantify the calculations performed within the cooling fluid analysis in the analysis discussed within this thesis. Once the Solver methodology was defined the setup of the simulation proceeded as explained in Chapter 4.

Chapter 4

Solidworks Flow Simulation: Global Conditions, Boundary Conditions and Mesh Development

Upon the completion of the assembly models of both the nozzle and diffuser, the system was prepared for the fluid simulation solver analysis. The Flow Simulation package in Solidworks was utilized. The Flow Simulation software comes with a "Wizard" that establishes initial system parameters, an example of which is shown in Figure 4.1. The wizard tool identifies the type of flow analysis (internal or external) along with whether or not, gravity, radiation, heat conduction,

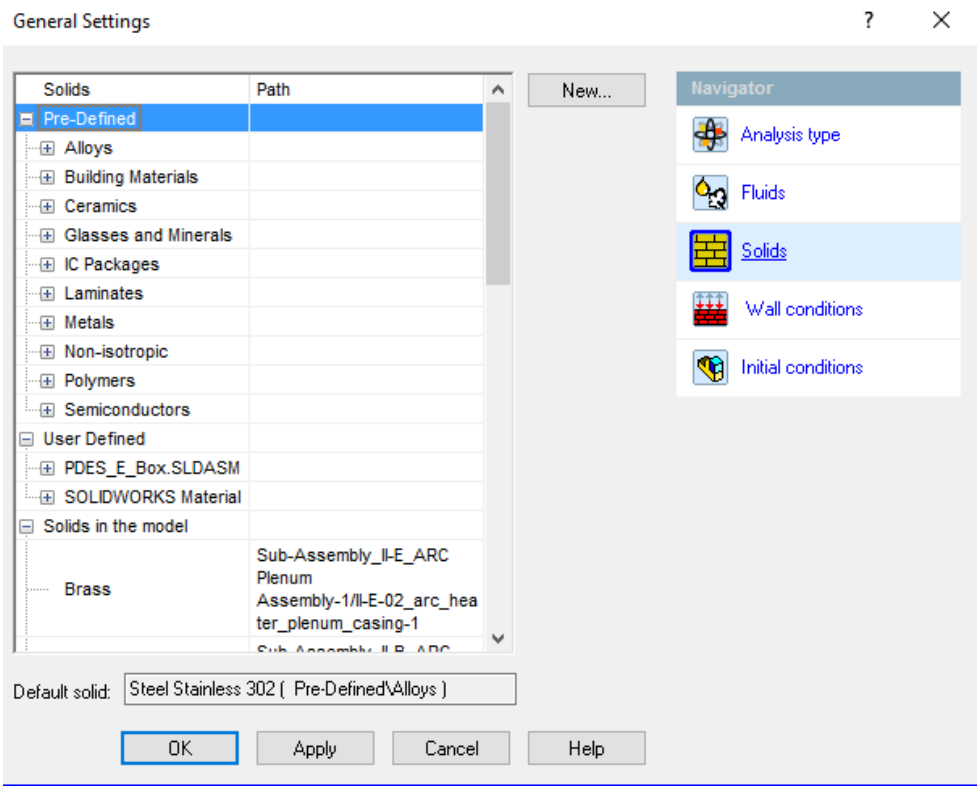

Figure 4.1: Screenshot of Solidworks Flow Simulation Wizard Setup tool menu.

rotation and time dependent factors will be simulated. This is followed by determination of what wall conditions should be set for surfaces at the edge of the domain. In this thermal analysis, the outer surfaces of the system not in contact with the hot internal gases are defined with an adiabatic wall, preventing dissipation of heat from the system. This means that any surface that will be exposed to the air in the operation room will not be allowed to transfer heat. In the real case scenario

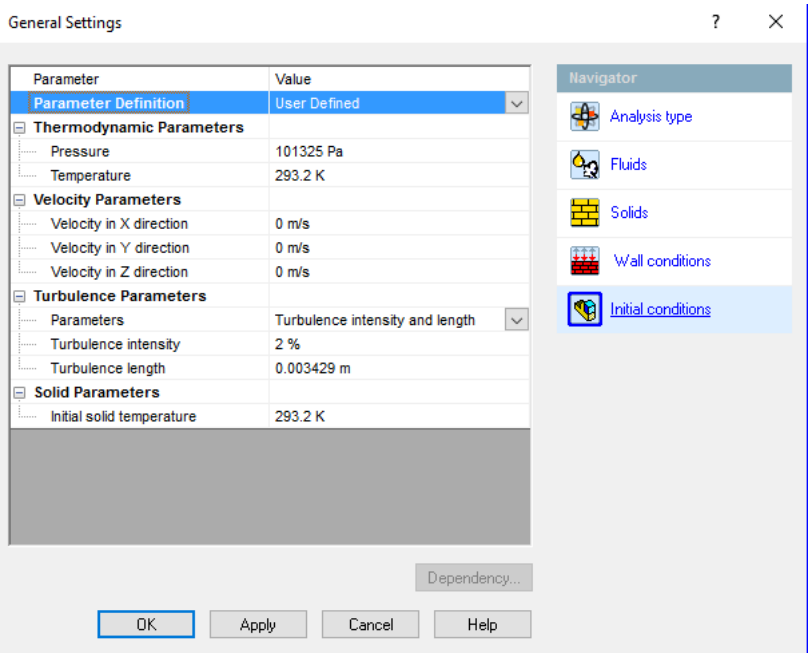

Figure 4.2: Solidworks Flow Simulation Wizard Global initial conditions tab.

there will be free convection within the air surrounding the nozzle and diffuser, but simulation of the outer fluid requires much greater computational requirements and as such the adiabatic condition is considered to be a worst-case scenario for the boundaries of the computational domain. The last step of the wizard is to establish the initial conditions of the system, as shown in Figure 4.2, including the ambient

thermodynamic properties, turbulence parameters, and starting solid temperature. Once the wizard is complete, the setup of the simulation proceeds to creating fluid subdomains, as shown in Figure 4.3 for the final nozzle simulation. First lids are created to "seal" the fluid volume off from the external computational domain. Then the lids are selected within the "insert Fluid subdomain" option and the fluid volume should appear as shown in Figure 4.3. The initial thermodynamic parameters of the fluid (pressure and temperature), any initial velocity and the turbulence parameters of the fluid subdomain are also defined at this time. If the fluid subdomain fails to generate, Solidworks Flow Simulation offers techniques to identify where the "leak" is, where the intended fluid domain is connected with the

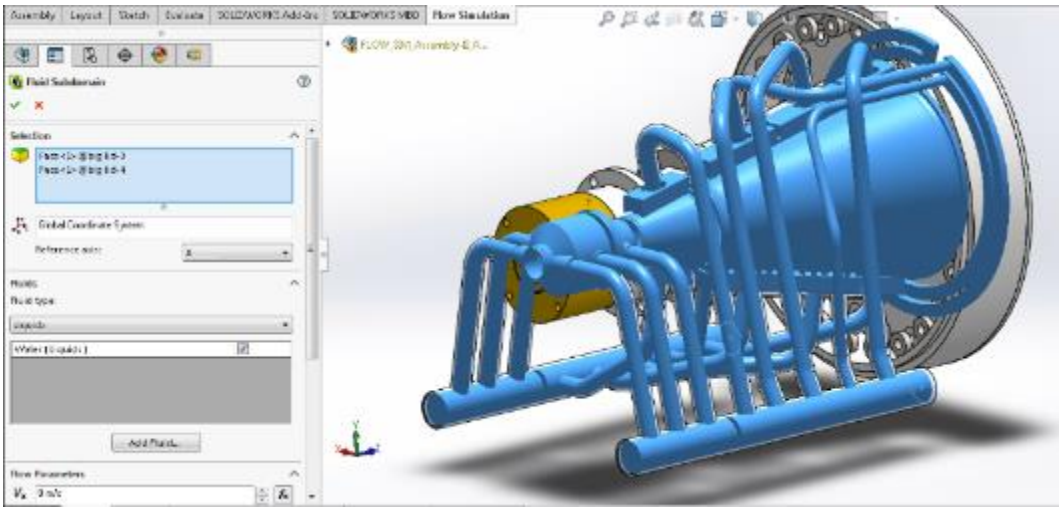

Figure 4.3: Fluid subdomain creation process shown for final nozzle simulation.

rest of the computational domain due to gaps in model bodies.

Once the fluid subdomain has been generated, the next step is to define the materials of all bodies within the system. The parts of the system are individually

selected and assigned a specific material either from the supplied list of materials or from user-defined characteristics. For the case of the nozzle, a material was created to represent the UNS 81500 material that was chosen as the material for the inner copper bodies, as no such material existed in the Solidworks material database for flow simulation. Once the materials are defined, the next step in the simulation setup is to identify the boundary conditions. This is the other place where the lids created to seal off the system become necessary, because they serve as the surface upon which the boundary conditions are implemented. Both the nozzle and diffuser the systems were chosen to have pressure inlet and mass-flow outlet boundary conditions, the menus for which are shown in Figure 4.4. With the boundary conditions of the fluid established, the implemented heat flux to the bodies must be added as heat sources. The heat source option chosen for this analysis was a surface heat flux option that serves as a boundary condition on the internal surfaces. The input surface heat flux values, provided and discussed in Chapter 5 and Chapter 6, assume a 400 K wall temperature, something that is not set as a boundary condition in the Flow Simulation but will be discussed later. The surface heat flux was applied to the internal surfaces of all nozzle and diffuser bodies that are exposed to the flow. In the process of the Flow Simulation wizard the global mesh size is initially

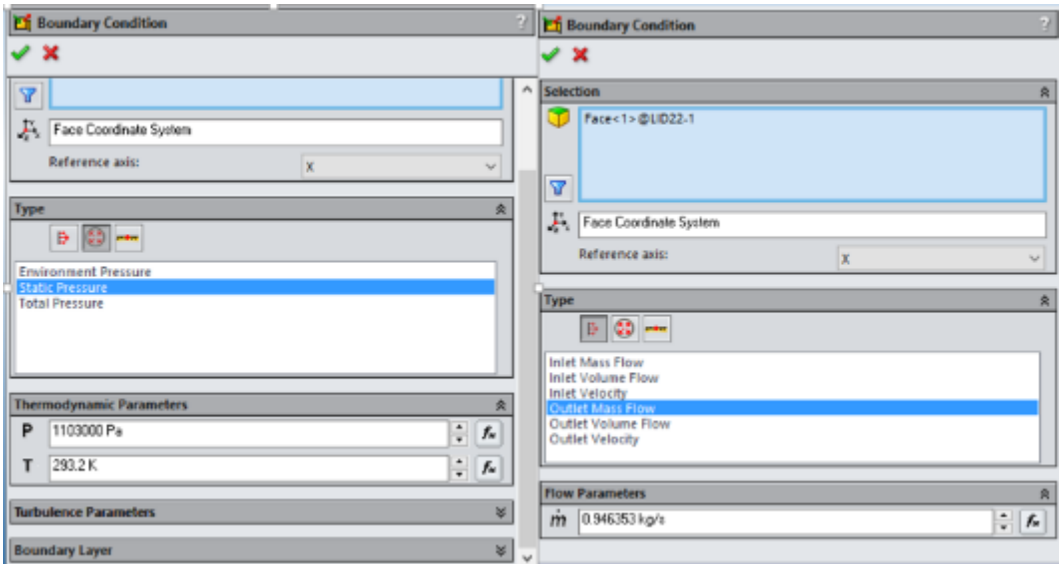

Figure 4.4: Boundary Condition menus for pressure inlet and mass flow outlet.

defined, but there is an option to create increased mesh refinement at locations of interest. As such, surfaces and volumes were selected to increase mesh resolution near the interface between the interior solid bodies and the fluid subdomain. The menus for the local initial mesh settings are shown in Figure 4.5. There are multiple things in this list that must be thoroughly discussed before proceeding. First, in Solidworks Flow Simulation the initial mesh of the system is determined by the level of the initial global mesh defined in the Wizard. From the level chosen, the computational domain is split into a series of equally sized rectangular parallelepiped cells, generating a structured Cartesian based mesh. For cases where the generated mesh cells cross a boundary between two a fluid and a solid, the original parallelepiped cell containing the boundary is split. As per the Solidworks Flow Simulation technical reference manual, each cell intersecting the solid/fluid

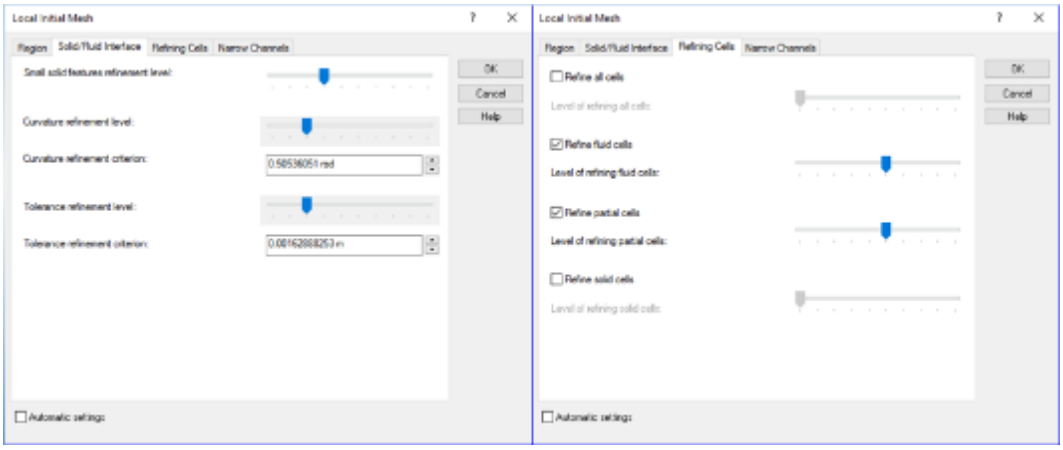

Figure 4.5: Local Initial Mesh Menu and options.

interface is split into 8 equivalent child cells; each of the child cells intersecting with the interface is in turn split into 8 cells for each level of refinement. The specified cell size is based upon the global geometric and local initial mesh refinement definitions. Each level of refinement corresponds to a cell being split into 8 child cells. A level 5 cell, which is implemented in the analysis in later chapters, has up to 8^5 cells generated for each basic mesh cell, if every cell were along the solid/fluid interface. Once this process of refinement of the solid/fluid interface is completed, the next consideration is the geometry of the system at the interface, specifically the interface curvature. This is a parameter listed in the local mesh menu-specifically there is a curvature refinement criterion and a curvature threshold as shown in Figure 4.5. The curvature criterion as defined in the Flow Simulation solver is the maximum angle between the normal to the surface inside one cell and should the value exceed the defined threshold, the cell is split into 8 cells [11]. The tolerance refinement criterion follows effectively the same process

as the curvature criterion [12]. The narrow channel criterion follows the same general principle, except it means that there must be a minimum number of fluid cells in a line normal to the solid /fluid interface, otherwise each of the cells on the line are split into 8 cells [11].

The last point of discussion of the Cartesian mesh in the Solidworks Flow Simulation concerns cells that still contain a solid/fluid boundary after initial mesh refinement. If a cell at this point contains a solid/fluid boundary such as a curved geometric surface, the curved geometry surface is approximated by a set of polygons which vertexes are the surfaces intersection points within the cells edges. As a result the cells near the boundaries are "polyhedrons with both axis oriented and arbitrary oriented plane faces" [11]. The two dimensional representation of this is shown in Figure 4.6. In the simplest case there are only two control volumes in the parallelepiped, one is solid and another is fluid. Now that the explanation of the Cartesian mesh has been discussed, the last step is to explain the goals parameter.

Solidworks Flow Simulation monitors convergence using quantities of interest to the user- this helps accelerate convergence and reduce computational requirements, at a slight loss to overall accuracy in more complex systems. The user may define specific parameters within the flow of primary importance in analysis, such as pressure, mass flow, heat flux, temperature, velocity, and others, and the system will monitor the values and the residuals of these choices as the

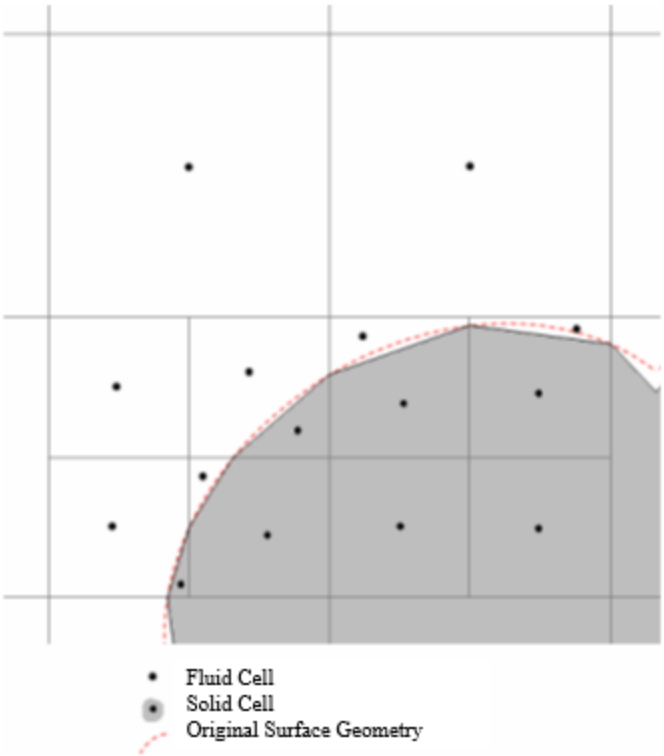

Figure 4.6: Cell decomposition of partial cells near solid/fluid boundary.

simulation iteration progresses. These goals can be set for any point, surface, or volume within the system, and the resultant residual values can be exported from the resultant simulation to determine convergence.

The last discussion about the mesh setup of the Flow Simulation involves the consideration of spatial approximation. For spatial discretization, the cell-centered finite volume method is used. The governing equations are integrated over the control volume resulting from the finite volumes. The conservation laws are discretized for the cells, then the fluxes are approximated based upon whether the cell is an axially (Cartesian system) oriented or arbitrarily oriented, with each classification being approximated differently. For faces common to two adjacent

control volumes, second order implicit approximations are used, and specifically for convective fluxes the upwind scheme is used [11]. The second order upwind scheme is a forward and backward difference equation used for solving hyperbolic partial differential equations. For diffusive terms, the central difference method is used [11]. For the solid/fluid interface the fluxes are approximated in accordance with the boundary conditions and taking into account the curved boundary geometry.

A point to be made involves adaptive mesh refinement, which actually occurs during the simulation. If there are local areas with strong flow gradient adaptive mesh refinement will increase the resolution by performing cell refinement and splitting as previously discussed, within user specified parameters. In areas of low flow gradient adaptive mesh refinement will merge cells to reduce computational needs. This allows for an evolving mesh grid that is refined towards areas of greater uncertainty and possible error.

Next the discussion of the analysis of the Nozzle and diffuser will proceed in Chapter 5 and Chapter 6.

Chapter 5

3-Stage Conical Nozzle: Design, Analysis and Results

The development of the three stage conical nozzle was the first system developed in the AHWT-II upgrade. Upon the receipt of the ONR/DARPA grant, the analytical design of the nozzle system began. The nozzle design to identify sizing and expansion angle was performed by the research group of Prof. Maddalena and the two dimensional sketch of the nozzle profile was provided for conceptual design. The first consideration of the assembly design was the cooling system methodology. Due to the certainty of high fluxes, the system must be actively cooled and the internal body must be able to dissipate the high heat loads. The nozzle body material was chosen to be a copper alloy; after investigation of material choices available with high yield strength and thermal conductivity, the decision was made to proceed with either UNS-C81500 or UNS C-18150, depending on material availability. The former is a copper chromium alloy, the second is a copper zirconium alloy. The copper chromium alloy has a tensile yield strength of 275 MPa and a thermal conductivity of 315 W/m-K, while the copper zirconium alloy has a tensile yield strength of 496 MPa and a thermal conductivity of 323 W/m-K [13]. The minimum requirements for the system allowed for either material to be used, with preference towards UNS-C 18150. Once the internal material was defined, the cooling methodology was analyzed. There were several options initially considered for the flow pathway of cooling, shown in Figure 5.1,

with advantages and disadvantages of each method of cooling. The rectangular slots offer the most ideal cooling circumstance since the cooling circumferentially and the thermal variation is along the axial direction from highest to lowest heat flux

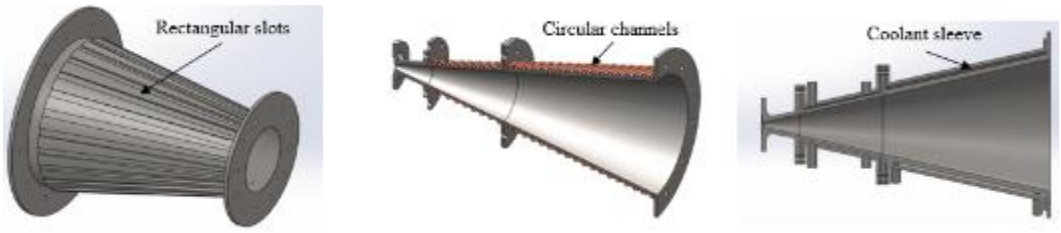

Figure 5.1: Nozzle cooling methods considered in initial design.

region, but the manufacturing is quite expensive and requires a complex manifold on each flange to equivalently distribute the fluid within each axial channel. The circular channels method is cost effective for manufacturing and the tubes can be replaced if necessary, but the conduction between the cooling tubes and the main body is limited by the contact resistance between the two, and the system would require an extensive manifold system with variable ports to appropriately distribute the flow. The third option, the coolant sleeve, requires significant welding to assemble the external cooling sleeve, but the cooling fluid distribution can be established using a series of holes supplied by a manifold system, reducing machining costs. After consideration, the cooling sleeve design was chosen for advanced development.

Upon the decision of the cooling sleeve design, the next step was to establish an axisymmetric heat flux distribution along the nozzle body. While the non-equilibrium, chemically reacting flow analysis was being performed by the

research group of Prof. Serhat Hosder at Missouri S&T, the analysis proceeded with information obtained during a literature research that encompassed arc-heated wind tunnel and nozzle flow characterization reports. This was done for two reasons- first, the verification that the current cooling system capacity to reject the necessary heat of the system needed to be proven. Second, upon receipt of the analysis of the thermo-chemical non-equilibrium heat flux results, the initial analysis would serve as a verification tool for confirming the accuracy of the simulation. During the process of the literature review a technical report on the experimental and numerical investigation of the heat transfer in a rocket nozzle of similar length was found from NASA. The report included a plot of the heat flux decay as a function of axial distance along the nozzle, as shown in Figure 5.2. After analyzing the heat flux decay along the nozzle from the peak point at the throat, this heat flux decay (not the actual value, just the decay trend) was considered to be an ideal initial design criterion for the nozzle cooling distribution analysis due to the geometric similarity. The heat flux curve was developed into a matching curve fit power law as a function of axial distance that was applied to the nozzle design, based upon the peak throat heat flux.

Before beginning the cooling system analysis for the new system, the cooling system characterization of the current AHWT Mach 1.8 nozzle segment was performed by the research group. The temperature rise in the cooling fluid was known from previous testing to be $\Delta T = 3.3K$. The mass flow rate and total

pressure of the system were experimentally determined for the current nozzle segment through a series of tests. The test setup for three separate tests, the flow

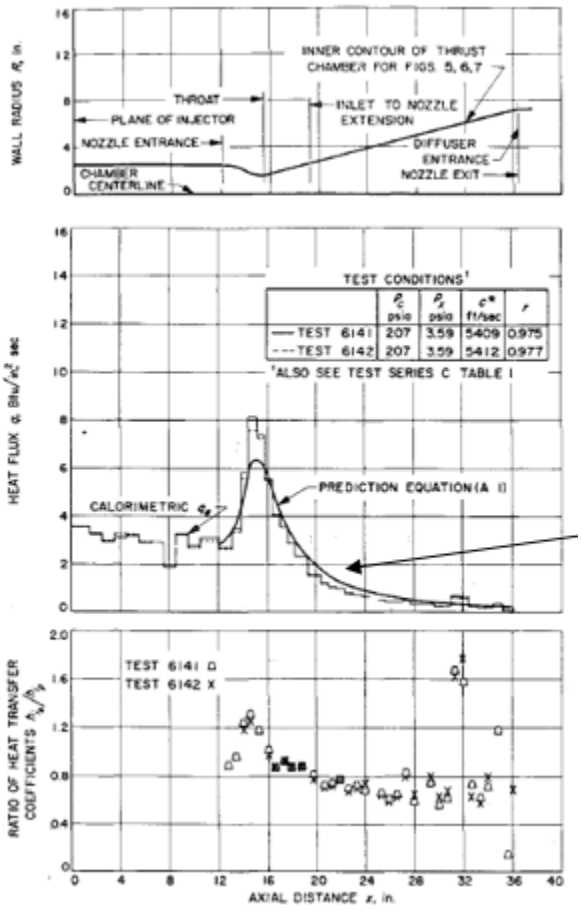

Figure 5.2: Heat flux decay of rocket nozzle used for initial analysis [14].

rate, static pressure and total pressure measurements are shown in Figure 5.3.

From the tests performed for the nominal operation of the system, the cooling fluid mass flow rate through the segment was determined to be approximately 0.95 kg/sec, and the total pressure was determined to be approximately 1.13 MPa. These values were instrumental in the initial analysis and flow distribution of the system,

and the full table of static pressure and mass flow measurements as a function of

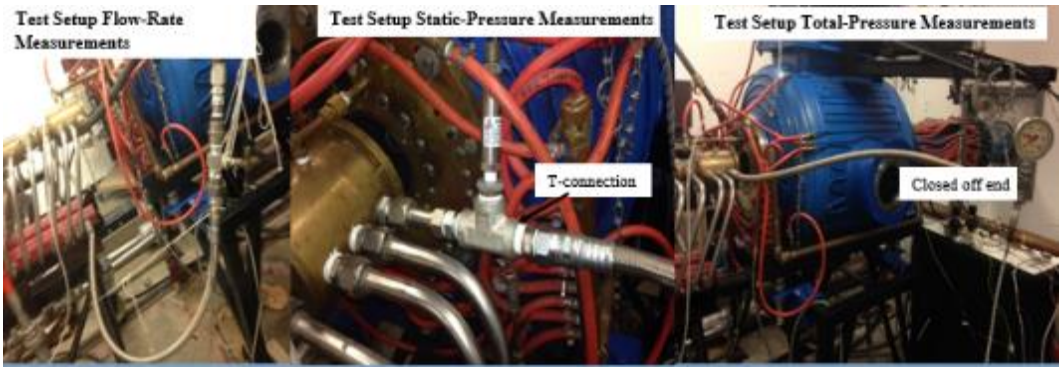

Figure 5.3: Flow Rate, Static Pressure and Total pressure tests on current AHWT Mach 1.8 nozzle.

centrifugal pump frequency settings is shown in Table 5.1.

Table 5.1: Experimental results of Mach 1.8 nozzle cooling fluid characterization.

f_motor (Hz)	Q_nozzle (GPM)	Q_nozzle (m^3/s)	mdot_nozzle (kg/s)	U_Tconnection (m/s)	U_manifold (m/s)
20	5.7	0.00036	0.359614	0.71	1.629
30	9	0.000568	0.567812	1.121	2.573
40	12	0.000757	0.757082	1.494	3.43
50	15	0.000946	**0.946353**	1.867	4.287

f_motor (Hz)	P_in (psi)	P_out (psi)	Ptot_in (psi)	Ptot_out (psi)
20	37.12	38.338	45.993	40.926
30	62.651	62.513	74.842	70.553
40	97.194	95.267	114.946	110.316
50	141.573	**137.507**	164.526	161.395

VALUE USED FOR SIMULATION

Before the cooling system analysis of the new nozzle segments, the choice of the appropriate boundary conditions for the nozzle flow simulations was

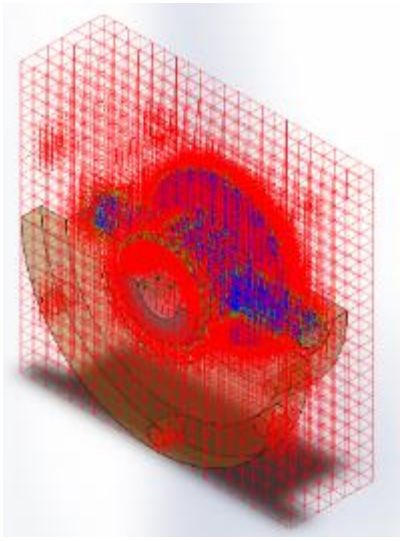

Figure 5.4: Cell mesh for original nozzle body flow simulation setup.

considered. The values of the Mach 1.8 nozzle cooling characterization were implemented in a series of simulations that were set up to consider all options of inlet and outlet boundary conditions. This process was performed for the model of the Mach 1.8 nozzle for comparison. First the nozzle was defined in Flow simulation and meshed as discussed in Chapter 4. The initial mesh of this system is shown in Figure 5.4, where red cells represent solid material, blue cells represent fluid, and green cells represent partial cells that are split into polygonal domains of fluid and solid. Once the simulation was set up it was duplicated for each set of inlet and outlet boundary conditions, and the cases were simulated. The sectional view of the velocity plots is shown for comparison in Figure 5.5. The intention was

to use the Total Pressure inlet condition and the mass flow outlet condition. The final simulation was run with the static pressure at the outlet from the flow

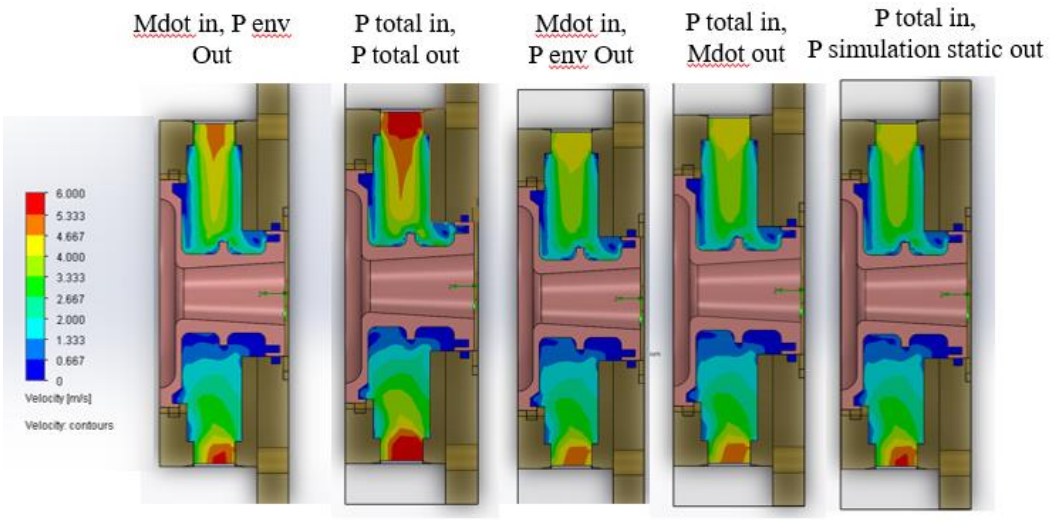

Figure 5.5: Comparison of results between sectional velocity plots for each boundary condition set.

simulation of the Pressure inlet/ mass flow outlet condition. Once the simulations were completed, Table 5.2 was generated to compare the results from the experimental characterization of the Mach 1.8 nozzle.

In the velocity plot comparison of Figure 5.5, it can be seen that the total pressure inlet and mass flow outlet match closely with the mass flow inlet and environmental pressure outlet (which is considered total pressure on an inlet side and a static pressure on an outlet side). The total pressure inlet and simulation static outlet condition also matches in this closely, and the velocity closely matches the manifold value in Table 5.1. These factors did not alone determine the boundary layer choice, but they reinforced the boundary condition setup. The comparison of

outputs from Table 5.2 served as the deciding factor. In the table, the rose colored cells represent the input conditions. The most important considerations were how well the other parameters compared with the experimental cooling fluid characterization. The known temperature rise, along with the static pressure drop across the system were considered, but due to the possibility of losses in the T-fitting used to measure the static pressure losses, none of the simulation values closely matched the pressure drop across the nozzle. As such greater weight was placed upon the proper mass flow rate, the temperature rise in the segment, and the known total pressure at the inlet. The inlet total pressure experimental measurement was considered a much more accurate value due to the stagnation of the flow to the line during testing.

Upon completion of the system boundary condition choice, the analysis of the cooling system requirements to offset the surface heat flux of the new nozzle began with the integral energy equation:

$$\int_{CV} \frac{\partial(\rho h)}{\partial t} dv + \int_{CS_{in}} \rho h_{in} (V_{in} \cdot \hat{n}_{in}) dS_{in} + \int_{CS_{out}} \rho h_{out} (V_{out} \cdot \hat{n}_{out}) dS_{out} = \bar{\dot{q}}_c A_{conical} \quad (20)$$

The analysis in this thesis is steady state, so the first term drops out, and the equivalence of the inlet and outlet areas, combined with the incompressibility of water result in the equation reducing to

$$\dot{m}_{water}(h_{out} - h_{in}) = \dot{m}_{water} \bar{C}(T_{out} - T_{in}) = \bar{\dot{q}}_c A_{conical} \quad (21)$$

Table 5.2: Flow Simulation Boundary Condition Results Comparison.

	Inlet BC	Outlet BC	Ptot Inlet (Pa)	Pstatic Inlet (Pa)	Mdot inlet (kg/sec)	Ptot Outlet (Pa)	Pstatic Outlet (Pa)	Mdot outlet (kg/sec)	Temp Fluid outlet (K)
Min, Pout	0.9463525 kg/sec	950000 Pa	9.750E+05	9.650E+05	0.946353	9.608E+05	9.500E+05	-0.946350	296.51
Pstatic in Mout	972000 Pa	0.9463525 kg/sec	9.816E+05	9.720E+05	0.946352	9.682E+05	9.581E+05	-0.946353	296.52
Ptot in Ptot out	1134200 Pa	1112800 Pa	1.134E+06	1.119E+06	1.185363	1.113E+06	1.097E+06	-1.185362	295.83
Penv in, Penv out	1134200 Pa	1112800 Pa	1.134E+06	1.126E+06	0.893272	1.122E+06	1.113E+06	-0.893270	296.69
Penv in , Penv out (2)	1134200 Pa	950000 Pa	1.134E+06	1.061E+06	2.617353	1.030E+06	9.500E+05	-2.617347	294.38
Penv in, Penv out (3)	976000 Pa	950000 Pa	9.933E+05	9.760E+05	1.270730	9.687E+05	9.500E+05	-1.270731	295.65
Min Wrong Penv out	0.9463525 kg/sec	1103000 Pa	1.128E+06	1.118E+06	0.946353	1.114E+06	1.103E+06	-0.946348	296.52
Min Wrong Ptot out	0.9463525 kg/sec	1103000 Pa	1.117E+06	1.107E+06	0.946353	1.103E+06	1.093E+06	-0.946350	296.51
Ptot in, Mout	1134200 Pa	0.9463525 kg/sec	1.134E+06	1.125E+06	0.946354	1.121E+06	1.110E+06	-0.946353	296.51
Tot in, Static out	1134200 Pa	1112800 Pa	1.134E+06	1.126E+06	0.892932	1.122E+06	1.113E+06	-0.892931	296.68
Tot in Static out	1134200 Pa	950000 Pa	1.134E+06	1.061E+06	2.617483	1.030E+06	9.500E+05	-2.617483	294.38
Totin, sim static out Check of Validity of System (Pstatic input from Ptot in, Mout)	1134200 Pa	1110333 Pa	1.134E+06	1.125E+06	0.942791	1.121E+06	1.110E+06	-0.942786	296.50
Ptotin-delP, mout (REV 2)	1076546 Pa	0.9463525 kg/sec	1.077E+06	1.067E+06	0.946353	1.063E+06	1.053E+06	-0.946353	296.50

The nozzle mass flow rate and Furthermore, by assuming $\bar{C}\Delta T$ to be a constant for each segment for analysis, and normalizing the system with respect to the experimentally determined flow rate of the current Mach 1.8 nozzle segment the equation can be modified to

$$\frac{\dot{m}_{throat}}{\dot{m}_i} = \frac{\bar{q}_{c,throat} A_{throat}}{\bar{q}_{c,i} A_i} \tag{22}$$

By establishing the equation normalizing the mass flow rate to the nozzle throat (the point of the peak heat flux}, the flow distribution available from the current cooling fluid supply can then be distributed equivalently based upon the heat rate through each segment (the heat flux times the surface area). Based upon the heat flux curve shown in Figure 5.2, the surface of the Mach 6 nozzle system was broken down into 2 inch segments and shown in Figure 5.6. These segments were arbitrarily defined to create a quantifiable heat rate and mass flow within a specific band of the nozzle body and similar heat rejection rates for each two segments.

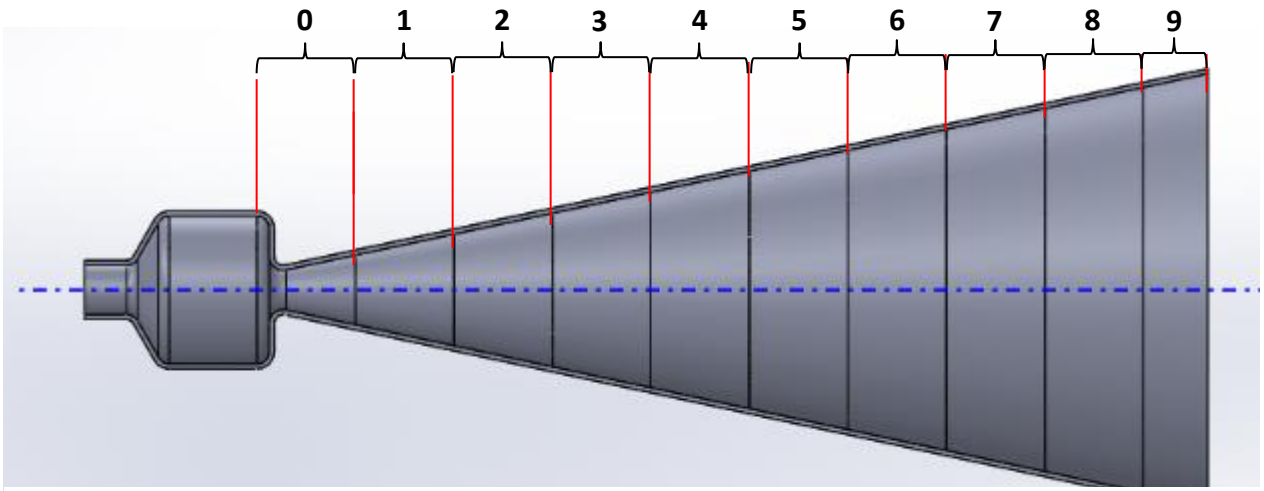

Figure 5.6: Segmentation of the nozzle body for heat rate and cooling fluid analysis.

From the breakdown of the nozzle into segments, the analysis proceeded using equation 22, the heat flux rate from Figure 5.2, and the geometry of the nozzle body to create a table of mass flow ratios with respect to the nozzle throat segment, shown in Table 5.3.

Table 5.3: Mass flow per segment normalized to the mass flow rate of the throat segment.

Segment	Wetted surface (m^2)	qw_ave (W/m^2)	qw/qw_throat	A/A_throat	Mdot/Mdot_throat	Mdot additional (%)	
0-Throat segment	0.006488258	9010750.368	1	1	1		
1	0.007612656	5395678.481	0.598804568	1.173297325	0.702575798		
2	0.011136171	3309029.175	0.367231256	1.716357656	0.630300178	**133%**	**Mach 4**
3	0.0146597	2103219.775	0.233412279	2.259419976	0.527376365		
4	0.018183228	1405067.249	0.155932324	2.802482296	0.436997578		
5	0.021706757	999516.6981	0.110924913	3.345544615	0.371104244		
6	0.025230272	762637.6444	0.084636419	3.888604947	0.329117598		
7	0.028753801	623011.8439	0.06914095	4.431667267	0.306409687		
8	0.032277329	539482.2609	0.059870958	4.974729586	0.297841828		
9	0.017459991	497049.5833	0.055161841	2.69101366	0.148441269	**242%**	**Mach 6**

As it can be seen from the table, the Mach 4 nozzle requires 30% higher flow rate to maintain the same fluid exit temperature than the nozzle throat. The Mach 6 nozzle requires 2.4 times the flow rate to maintain the same temperature rise as the nozzle. To match the segmentation of the nozzle bodies within the cooling fluid analysis, ribs were added to the internal body at locations generally matching the segmentation used in Table 5.3.These ribs served a secondary purpose, to reinforce the nozzle body due to thermal and pressure loading it will experience. The methodology of flow distribution was implemented for the Mach 4 and Mach 6 segments, while the Mach 2 nozzle throat segment used the prior brass casing fluid design to substitute into the current system where the original Mach 1.8 nozzle attached. For distribution of the low to each segment the design implemented a manifold system, such that fluid entered through multiple NPT ports into the system

and was then distributed further among multiple holes within each 2 inch segment. The distribution and identification of the holes through nomenclature used in analysis below, is shown in Figure 5.7. For the Mach 4 segment, the segments 1

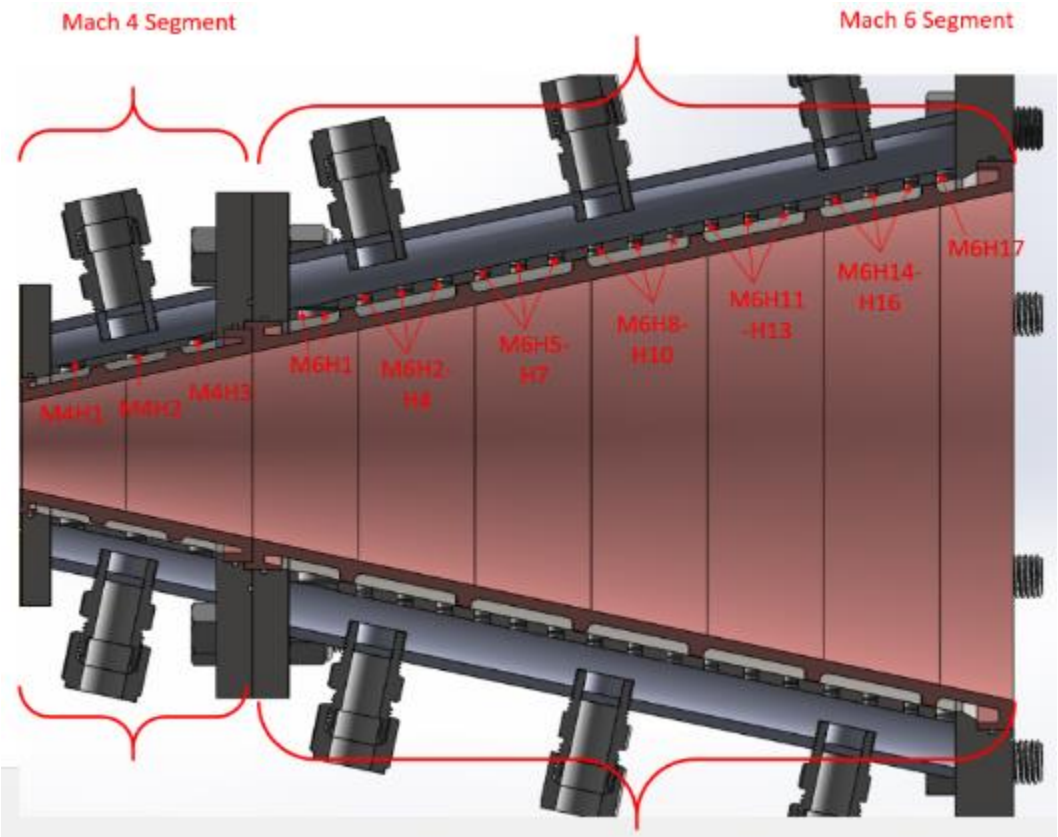

Figure 5.7: Mach nozzle segment breakdown and cooling-hole nomenclature.

and 2 shown in Figure 5.6 are split into three flow channels by two ribs for structural integrity. A single NPT port supplies the Mach 4 nozzle segment, and each cooling channel is supplied from the manifold by one inlet hole in the cooling sleeve body. The Mach 6 body is supplied by three NPT ports and is split into seven segments (6 2 inch segments plus the remaining length), and with exception to the first and last segments (segments 3 and 9 respectively in figure 5.6) each cooling channel is

supplied cooling fluid by three small holes in the cooling sleeve within the segment span, as shown in Figure 5.7. This makes for a total of 17 holes in the Mach 6 segment cooling sleeve that can be used to distribute the flow across the surface of the inner nozzle body.

Based upon the flow distribution for each segment and knowing the NPT cross sectional flow area, the process of sizing the holes for the cooling sleeve progressed. Each hole was a proportion of the NPT inlet area based upon the respective percentage of cooling flow quantified by heat rejection for the cooling channel over the total heat rejection for the nozzle segment. To consider the orifice effect of the hole distribution, a discharge coefficient of 0.61 to 0.63 was added to the hole sizing process- this means that the hole sizes in the cooling sleeve should be 1.63 times calculated area of the cooling sleeve based upon direct separation of the NPT inlet area. An example of the hole sizing modification is shown in Figure

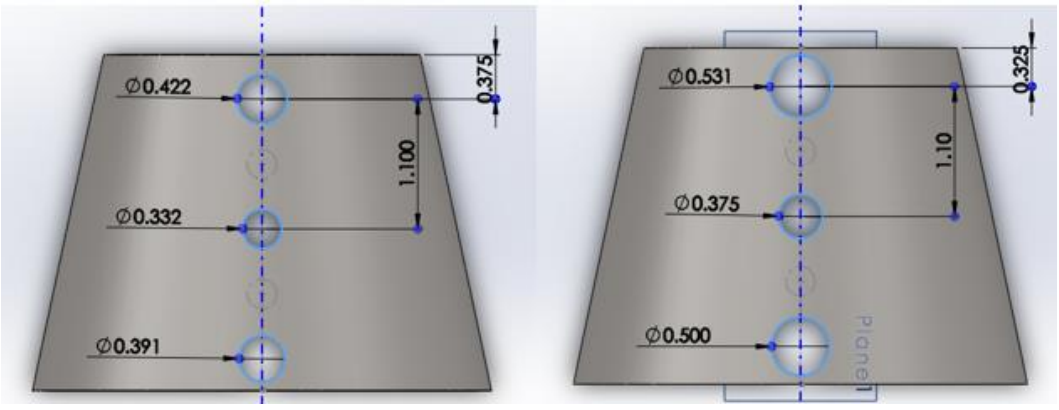

Figure 5.8: Mach 4 Cooling sleeve without and with discharge coefficient applied to the hole sizes.

5.8 for the Mach 4 cooling sleeve, and in Figure 5.9 for the Mach 6 cooling sleeve.

There was further consideration of the hole sizing due to location of the holes with respect to the NPT inlet location. The holes directly below the inlet were undersized

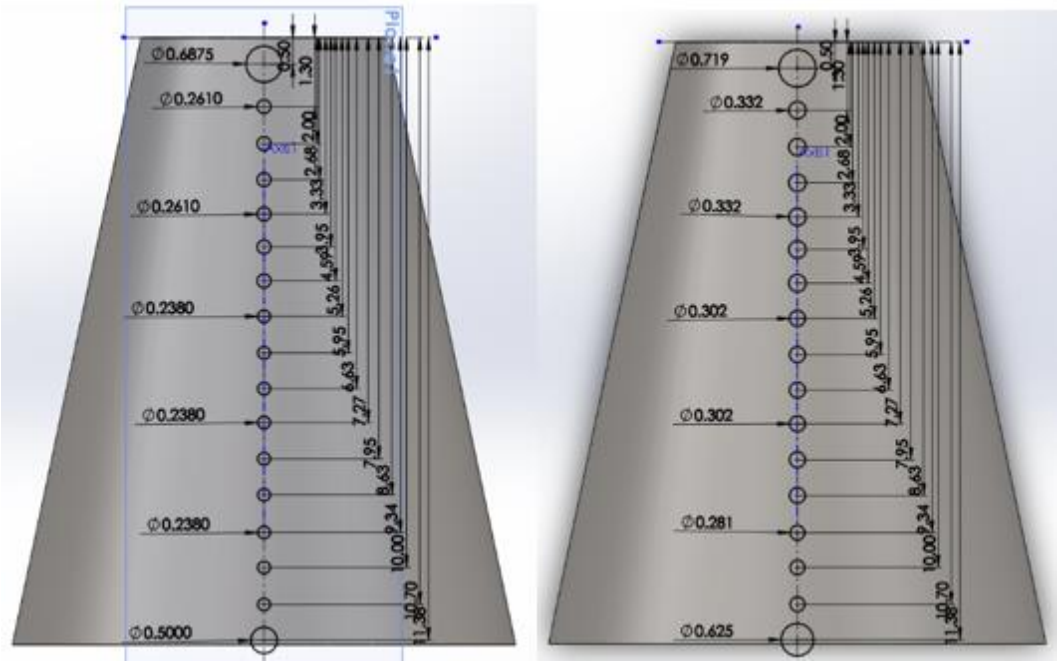

Figure 5.9: Mach 6 sleeve hole sizing without and with discharge coefficient.

by approximately 50% due to the flow being directed into these holes; this was a method to ensure appropriate distribution of the flow to all segments, regardless of location with respect to the inlet ports. The process of refining these values was performed case by case in the Flow Simulations, while independently monitoring the disparity of the flow rate distribution. The example of the Mach 4 nozzle iteration spreadsheet is shown in Table 5.4. As can be seen, the ideal mass flow rate percentage of available flow was defined based upon the heat rate (heat flux times surface area) of the nozzle segment. The hole sizing was then quantified based upon

a percentage of the inlet area, and once the discharge coefficient was applied the nearest standard drill bit size was chosen for each hole.

Table 5.4: Mach 4 hole sizing iteration spreadsheet.

MACH 4			
Segment #	M4 S1	M4 S2	M4 S3
IDEAL Mdot/Mdot throat	0.529	0.471	
HOLE NAME	Mach 4 Hole 1	Mach 4 Hole 2	Mach 4 Hole 3
Ideal (mdot/mdotsegment)	**0.353**	**0.333**	**0.314**
Iterated Hole Diameter (in)	0.531	0.368	0.516
Equivalent Drill Bit	17/32	U	33/64
SIMULATION SOLUTIONS			
Mass Flow Rate (kg/sec)	0.330	0.332	0.276
Percentage of Mass Flow Rate(%)	0.352	0.354	0.294
Error/Disparity (%)	**-0.003**	**0.062**	**-0.062**
Temperature Outlet (K)	296.67	295.93	297.06
Outlet Mass Flow Rate (kg/sec)			
ΔT (K)	3.475	2.728	3.863
MODIFICATIONS TO BE MADE			

After the simulation was run, the mass flow rate through each hole was analyzed, compared to the ideal mass flow per channel, and then suggestions of modifications were made for the next iteration. The Mach 6 hole sizing spreadsheet is shown in Table 5.5.

Table 5.5: Mach 6 hole sizing iteration spreadsheet.

MACH 6																					
Segment #	M6 S1	M6 S2				M6 S3			M6 S4			M6 S5				M6 S6				M6 S7	
IDEAL Mdot/Mdot throat	0.527	0.437				0.371			0.329			0.306				0.298				0.189	
HOLE NAME	M6H1	M6H2	M6H3	M6H4	M6H5	M6H6	M6H7	M6H8	M6H9	M6H10	M6H11	M6H12	M6H13	M6H14	M6H15	M6H16	M6H17				
Individual Hole Mdot/Mdottotal	0.215	0.059	0.059	0.059	0.050	0.050	0.050	0.045	0.045	0.045	0.042	0.042	0.042	0.040	0.040	0.040	0.077				
Segment Mdot/Mdottotal	0.215	0.178			0.151			0.134			0.125			0.121			0.077				
Iterated Hole Diameter (in)	0.71875	0.332	0.332	0.332	0.332	0.332	0.332	0.2969	0.2969	0.2969	0.302	0.302	0.302	0.28125	0.28125	0.28125	0.5625				
Equivalent Drill Bit	23/32	Q	Q	Q	Q	Q	Q	19/64	19/64	19/64	N	N	N	9/32	9/32	9/32	9/16				
Mass Flow Rate (kg/sec)	0.561	0.218	0.127	0.138	0.129	0.137	0.246	0.085	0.118	0.121	0.101	0.116	0.133	0.154	0.082	0.100	0.264				
Percentage of Hole Mass Flow Rate	0.198	0.077	0.045	0.049	0.046	0.048	0.087	0.030	0.042	0.043	0.036	0.041	0.047	0.054	0.029	0.035	0.093				
Percentage of Segment Mass Flow Rate(%)	0.198	0.171			0.181			0.114			0.124			0.119			0.093				
Error (%)	-0.076	-0.040			0.199			-0.146			-0.005			-0.022			0.214				
Temperature Outlet (K)	295.390	294.948	294.960	295.172	295.836	294.943	295.052	295.743	295.614	295.174	296.362	295.125	295.840	295.155	294.887	294.868	295.713				
Mass Flow rate Outlet (kg/sec)	0.603	0.150	0.157	0.157	0.156	0.160	0.162	0.107	0.098	0.122	0.121	0.122	0.126	0.111	0.107	0.100	0.272				
Hole DELTA T	2.190	1.748	1.760	1.972	2.636	1.743	1.852	2.543	2.414	1.974	3.162	1.925	2.640	1.955	1.687	1.668	2.513				
SEGMENT Delta T (Bulk)	2.190	1.828			2.072			2.292			2.575			1.775			2.513				

For the Mach 6 segment, since most of the segments contained three holes, the individual and combined flow rates were quantified, but the error was calculated per cooling channel, not per hole directly. The iteration tables shown in 5.4 and 5.5 are the final iteration of a process that occurred 5 times for the rocket nozzle data.

Before proceeding further, it was determined by the research group of Dr. Maddalena that the radiative effects of the flow exiting the nozzle and of the high-temperature test articles required strong cooling in the flange around the nozzle. Initially two methods of mounting the flange to the test section were considered, both shown in Figure 5.10. First it was considered to have a cooling flange bolt on

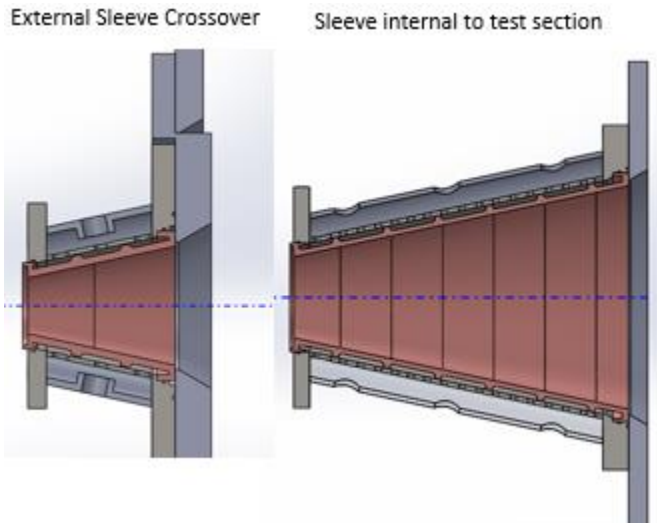

Figure 5.10: Cooling Flange Design Options.

from the outside of the test section and then slip inside to the front of the nozzle. The second design was a flat plate design mounted interior to the test section- this design allowed for relatively simple geometry for machining, The external-

crossover design made bolting the assembly to the test section easy, but the complex geometry of the crossover, and cooling the interior flange would be difficult. The fully internal design made the bolting of the flange difficult (must be internally supported while bolts from outside are tightened), but the manufacturing for a plate flange is simple and can be done by any 3 axis CNC mill. After these considerations, the fully internal cooling flange design was chosen and integrated into the nozzle assembly. The Mach 4 and Mach 6 configurations are shown in Figure 5.11. An interface flange from the test section is located between the cooling flange and the

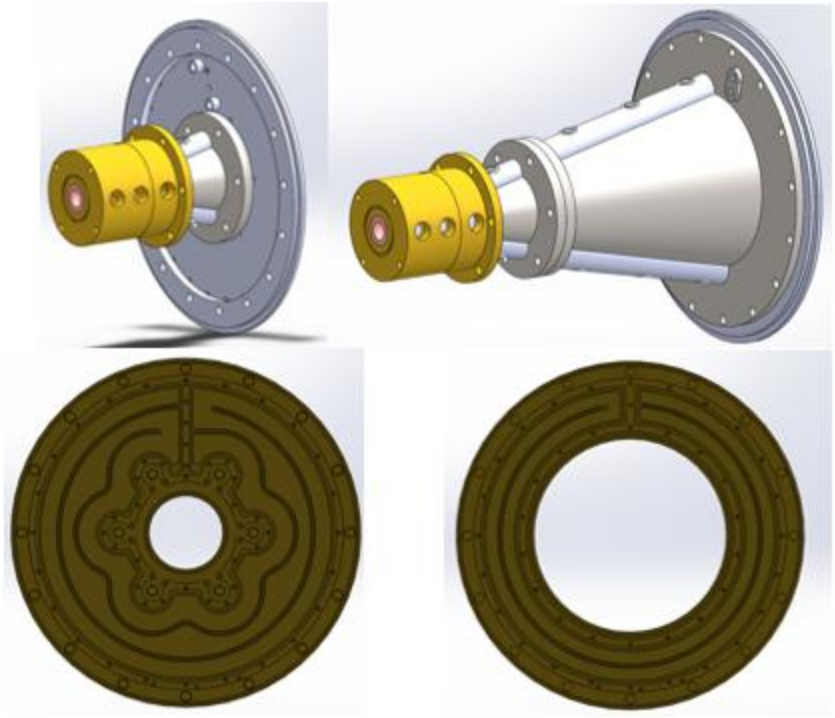

Figure 5.11: Cooling Flange Design for Mach 4 and Mach 6 nozzle configurations.

cooling sleeve on both the Mach 4 and Mach 6 flange. With the design of the

cooling flange, the nozzle assembly design was completed, and remained relatively unchanged until the finalization of the design.

With the initial flow distribution defined, the flow simulation analysis was progressed, and the first flow simulation was run with the rocket nozzle heat flux.

The resulting flow distribution plot is shown for the three stages in Figure 5.12. As can be seen, there is evidence of circulation in several of the channels, and

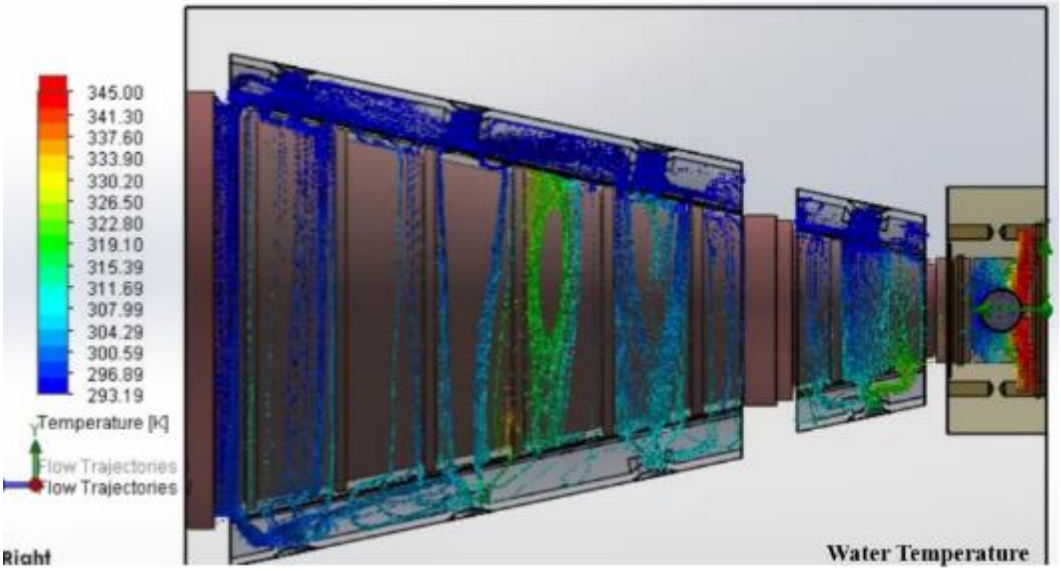

Figure 5.12: Initial Nozzle Flow Simulation Flow Patterns showing fluid temperature.

excessive heating within the nozzle segment. This circulation must be avoided due to the high heat flux within the flow in the nozzle. It is also evident that the flow distribution within the cooling channels is limited, something that must be iterated. The nozzle throat segment, which shows the highest fluid temperature rise, is shown in a focused image in Figure 5.13. As can be seen the fluid around the ring of the intersection with the plenum body, the fluid furthest from the main flow and

experiencing the lowest velocity, heats up significantly. The fluid temperature

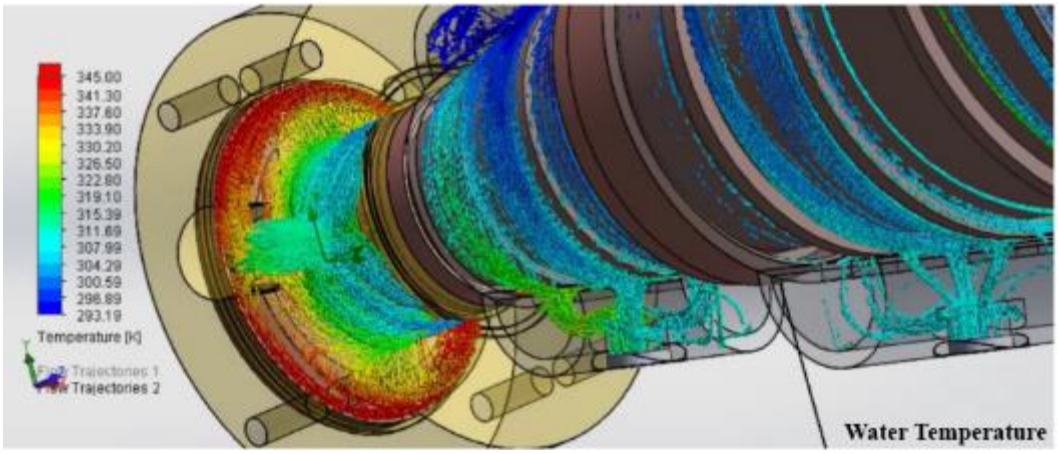

Figure 5.13: Close-up of nozzle throat segment flow distribution plot.

shown does not directly represent the surface temperature at the interface of the cooling fluid and the internal nozzle bodies. The surface temperature at the cooling fluid interface is shown in Figure 5.14. It is evident in the figure that the surface

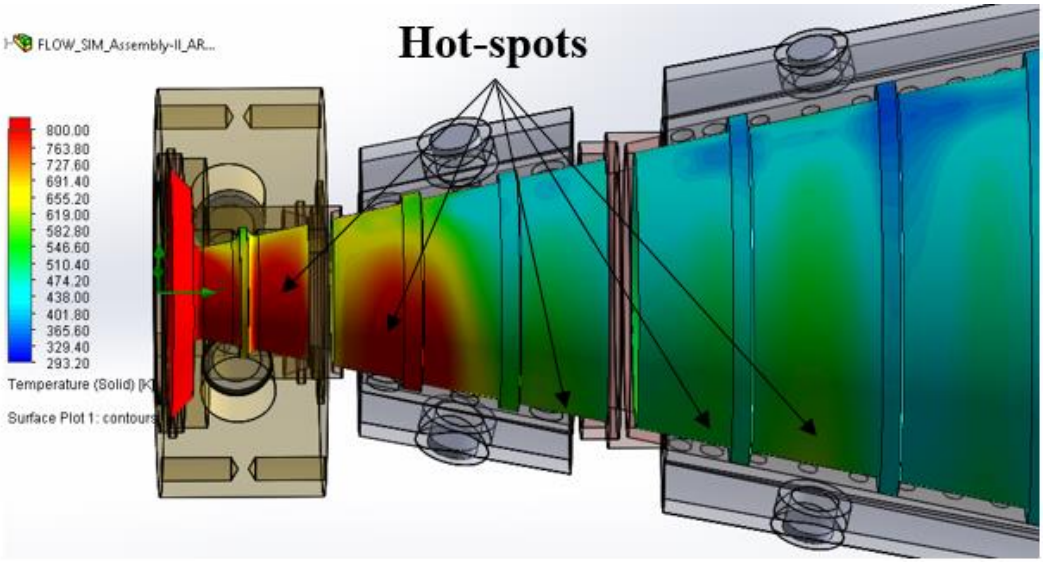

Figure 5.14: Cooling Fluid Interface Surface temperature plot on internal nozzle bodies.

interface temperature is much higher than the flow temperature shown in the

cooling fluid flowpatterns, and 800 K along the nozzle throat and Mach 4 segments is concerning to say the least due to the effect of temperature on yield strength of materials. The non-uniformity of the flow can also be seen in this image, causing hot-spots on the surface in regions of circulation or low flow rate, especially circumferentially towards the bottom of the segments. This is the only disadvantage to the cooling sleeve design that was chosen, the flow will heat up along its path and the cooling effect is not axisymmetric. The pressure drop of the segment was also checked, and is shown in Figure 5.15. The pressure drop can be seen to be approximately 30 kPa, which approximately matches the original experimental characterization pressure drop of the Mach 1.8 nozzle.

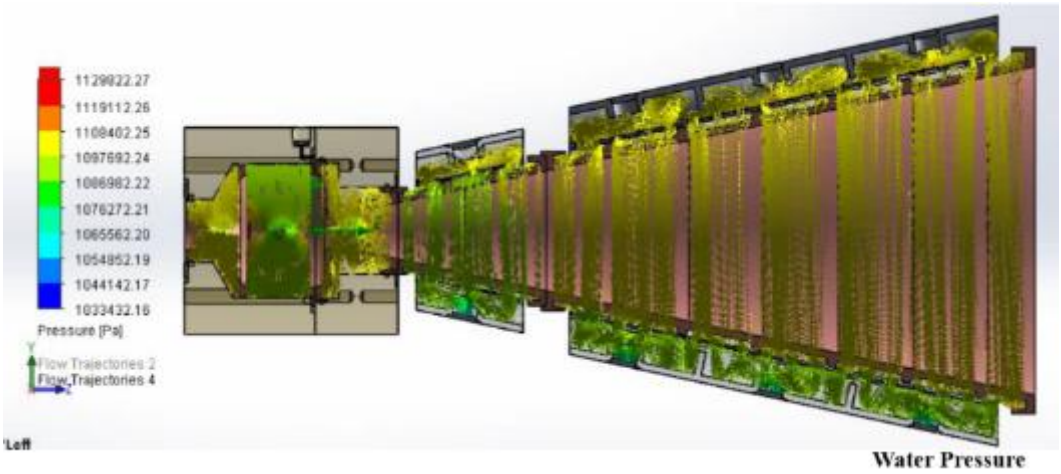

Figure 5.15: Flow distribution plot of fluid pressure within nozzle cooling system.

Once the Flow simulations were iterated for the original rocket nozzle heat fluxes to the final holes positions shown in Tables 5.4 and 5.5, the system was exported into Solidworks Simulation for FEA analysis- the actual thermal and pressure solutions from the Flow Simulation were imported into the FEA simulator.

This process allows for direct thermo-structural analysis of the system from the flow simulation conditions. The results for temperature and pressure from the are mapped from the flow simulation mesh to the FEA mesh, where spacial approximations are used to match the cartestian mesh of the flow simulation to the tetrahedral mesh of the FEA solver. Along with fixtures and fasteners, the simulation of the complete nozzle assembly was performed, and will be discussed for the final nozzle system below. The initial Simulation results are shown in Figure 5.16 for the Factor of Safety plot. Originally, the internal bodies were modeled as pure copper, and preload values for bolts were overestimated, and the system was

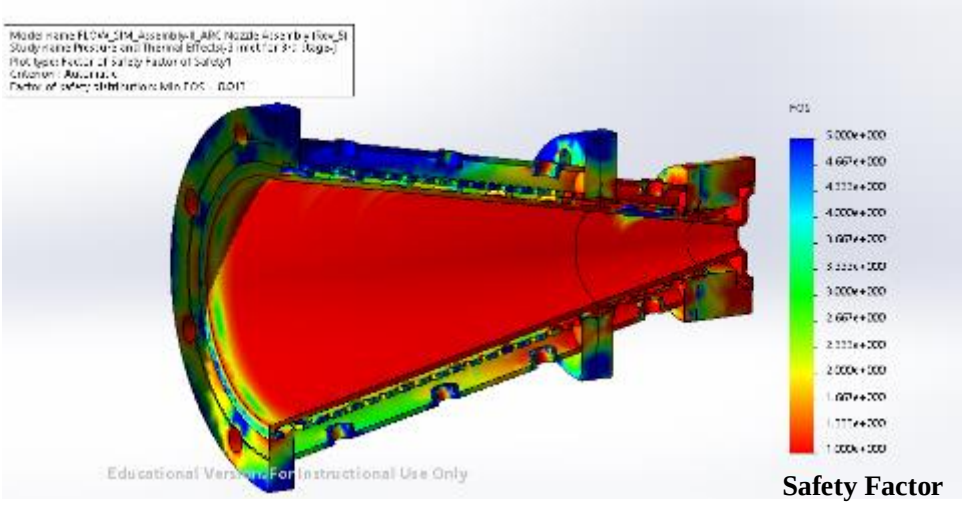

Figure 5.16: initial Solidworks Simulation results showing Factory of Safety Plot and failure of most components.

indeterminately fixed such that no thermal expansion was possible within the system. As such, most of the system showed results of significant failure. The

displacement plot of this simulation is shown in Figure 5.17. As can be seen, the indeterminate fixture prevented either end of the system from moving, but there

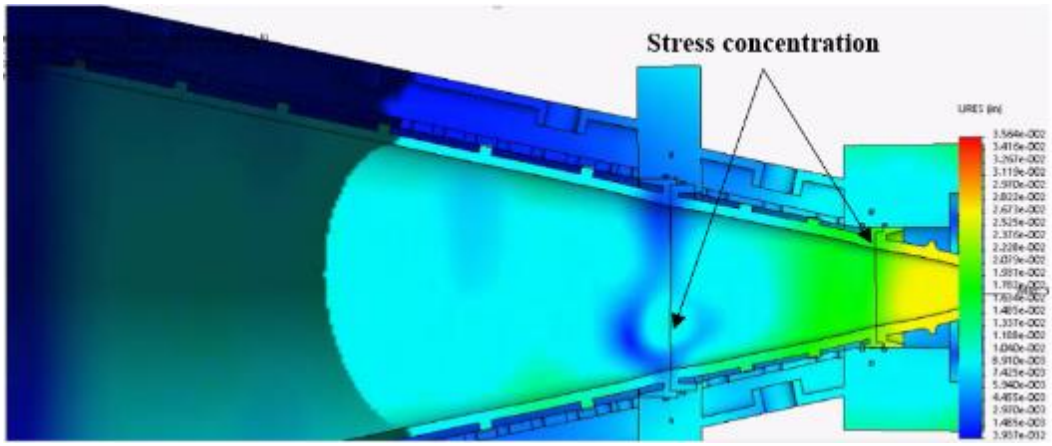

Figure 5.17: Displacement plot of initial FEA Setup.

were still significant defomration in the nozzle internal body segments. Two stress concentrations due to the uneven heating of the nozzle bodies are identified by the variable displacement within the regions. After this simulation, fixtures and bolting configurations were investigated further and corrected to more accurately model the intended system.

At this point, a non-equilibrium, chemically reacting simulation of the nozzle flow was completed by Dr. Serhat Hosder and his research group at the Missouri Univeristy of Science and Technology. The temperature and mass fraction plots of the simulation are shown in Figure 5.18. The plot is such that the valu of z=0 at the centerline of the exit plane of the nozzle. As can be seen, the mass fraction of the species converge shortly after the throat segment and remain stable until the nozzle exit- this results in frozen flow, where the Dahmkohler number, the

ratio of the flow time scale to the chemical time scale, approaches 0. The left plot features the Mach number, the translational temperature and vibrational

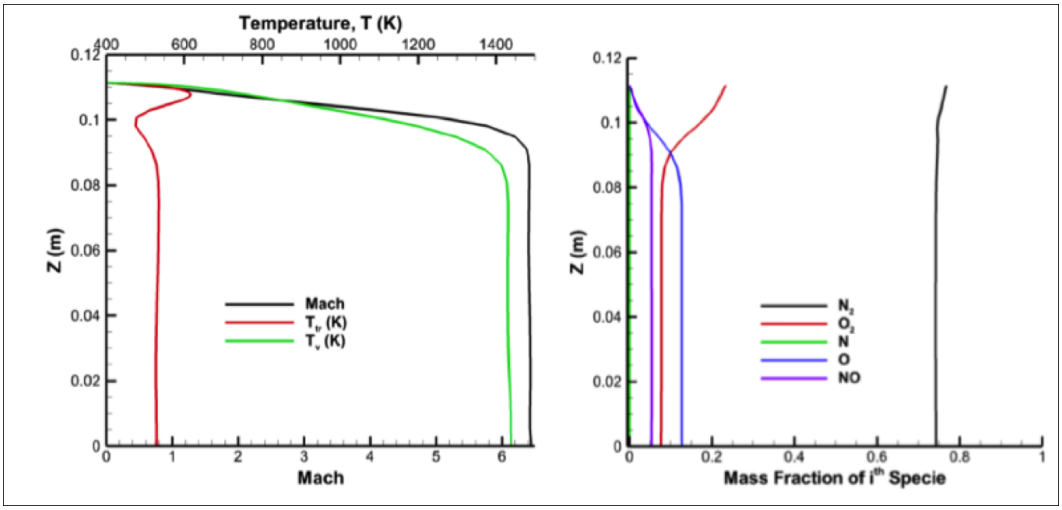

Figure 5.18: Nozzle CFD output for non-equilibrium, chemically reacting flow, Mach number temperatures and mass fractions [15].

temperature of the flow as functions of the axisymmetric distance from the nozzle exit. As it can be seen, the marked difference between vibrational and translational temperature shows a non-equilibrium flow. The mass fraction plot show that the flow freezes after the throat, a typical scenario in these type of flows. From this simulation, an axi-symmetric heat flux was generated for the analysis of the flow simulation iteration for the finalized system. The Mach 6 heat flux provided is shown in Figure 5.19. The heat flux curvature closely follows the power law decay of the original, but the curve is not nearly as steep, and the peak heat flux is about 5 times lower near the throat segment. The curve is broken down into two curves- the analytical plenum segment, which was approximated from the experimental

flow analysis performed on the nozzle, and the heat flux curve supplied by the nozzle simulations. The increasing slope towards the nozzle exit is a result of incorporating the radiative effects from the flow interaction with an hypotetical test article in front of the nozzle, the calculations of which were performed by the

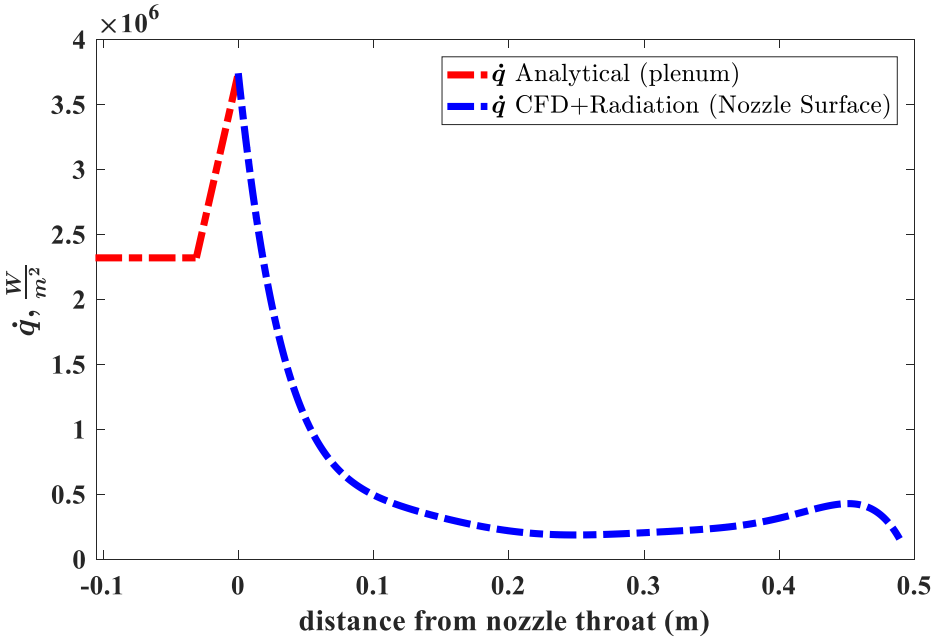

Figure 5.19: Mach 6 Axisymmetric Heat Flux curve output but Dr. Hosder's research group.

research group of Prof. Maddalena and are the reason for the active cooling flange.

After review of the simulation results and verification that the nozzle heat fluxes provided for the model were accurate, the analysis of the nozzle assembly progressed in the same process as the design for the rocket nozzle heat flux. First, the heat flux was broken down into segments equivalent to those shown in Figure 5.6. The average of the heat flux within this range was taken, and the values were applied to the flow simulation setup as shown in Figure 5.20. A uniform surface

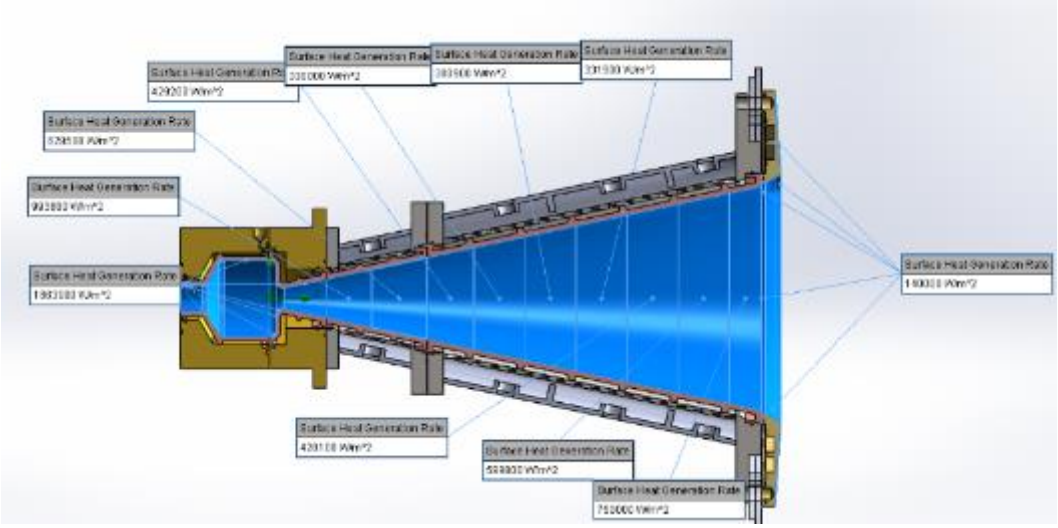

Figure 5.20: Heat Flux Values applied to segments for re-iteration of cooling hole sizing process.

heat flux was also initially applied to the nozzle cooling flange while radiative analysis was completed by the research group. From the heat flux segments, the previous iteration process was re-implemented, the initial iteration of which is shown below in Table 5.6. From the initial analysis, it became evident that the positioning of the NPT ports needed to be shifted further downstream on the Mach 6 segments to accommodate a higher heat flux towards the exit. Since the techniques necessary to make adjustments had alread been investigated and practiced in the previous iteration process, this iteration process took only three iterations from initial design (the final design of the rocket nozzle iterations) to the final hole placement and sizing along the cooling manifolds for the Mach 4 and

Mach 6 segments. The final results of the iterative process, which became the final hole sizing design for the nozzle system, is shown in Table 5.7.

Table 5.6: Initial hole sizing iteration for CFD heat flux input.

HOLE SIZING WITH DISCHARGE COEFFICIENT DR. HOSDER HEAT FLUX ITERATION 1																														
	MACH 4				MACH 6																									
Segment#	M4 S1	M4 S2	M4 S3	Segment#	M6 S1	M6 S2			M6 S3				M6 S4				M6 S5				M6 S6				M6 S7					
IDEAL Mdot/Mdot throat	0.529	0.471		IDEAL Mdot/Mdot throat	0.083	0.079			0.087				0.111				0.163				0.256				0.220					
HOLE NAME	Mach 4 Hole 1	Mach 4 Hole 2	Mach 4 Hole 3	HOLE NAME	M6H1	M6H2	M6H3	M6H4	M6H5	M6H6	M6H7	M6H8	M6H9	M6h10	M6h11	M6h12	M6h13	M6h14	M6h15	M6h16	M6h17								
Flow Breakdown	2/3 Segment1	1/3 segment 1, 1/3 segment 2	2/3 segment 2	Individual Hole Mdot/Mdottotal	0.083	0.026	0.026	0.026	0.029	0.029	0.029	0.037	0.037	0.037	0.054	0.054	0.054	0.085	0.085	0.085	0.220								
Initial (mdot/mdotsegment)	0.353	0.333	0.314	IDEAL Mdot (kg/sec)	0.237	0.075	0.075	0.075	0.082	0.082	0.082	0.105	0.105	0.105	0.154	0.154	0.154	0.243	0.243	0.243	0.625								
Percentage Considering Geometric Location with respect to inlet and outlet ports (1st attempt)	0.397	0.250	0.353	Segment Mdot/Mdottotal	0.083	0.079			0.087			0.111			0.163			0.256			0.220								
Ideal Mdot(kg/sec)	0.347	0.333	0.320	SEGMENT IDEAL Mdot (kg/sec)	0.237	0.226			0.246			0.315			0.463			0.728			0.625								
Ideal Starting Hole Diameter (in)	0.524	0.416	0.494	Ideal Starting Hole Diameter (in)	0.688	0.186	0.186	0.186	0.194	0.194	0.194	0.220	0.220	0.220	0.266	0.266	0.266	0.334	0.334	0.334	0.537								
Drill Size Used (in)	0.53125	0.413	0.5	Actual Hole Size Used	0.6875	0.332	0.332	0.332	0.332	0.332	0.332	0.302	0.302	0.302	0.302	0.302	0.302	0.302	0.302	0.302	0.6875								
Equivalent Drill Bit	17/32	Z	1/2	Equivalent Drill Bit	11/16	Q	Q	Q	Q	Q	Q	N	N	N	N	N	N	N	N	N	11/16								
SIMULATION SOLUTIONS																														
Mass Flow Rate (kg/sec)	0.330	0.305	0.292	Mass Flow Rate (kg/sec)	0.521	0.186	0.142	0.131	0.138	0.123	0.120	0.179	0.114	0.118	0.114	0.115	0.113	0.166	0.143	0.109	0.294								
Percentage of Mass Flow Rate(%)	0.356	0.329	0.315	Percentage of Mass Flow Rate(%)	0.184	0.162			0.135			0.145			0.121			0.148			0.104								
Error (%)	0.008	-0.013	0.005	Error	121.1%	104.4%			56.1%			31.1%			-25.8%			-42.3%			-52.8%								
Temperature Outlet (K)	296.848	295.842	296.988	Temperature Outlet (K)	295.66	295.09			295.85			294.98			295.45			294.99			295.19								
DELTA T	3.648	2.642	3.788	DELTA T	2.464	1.897			2.652			1.780			2.253			1.794			1.989								
MODIFICATIONS TO BE MADE	NONE! FINAL				DECREASE	DECREASE			DECREASE			LEAVE			INCREASE SLIGHTLY			INCREASE											

Table 5.7: Final hole sizing iteration values.

HOLE SIZING WITH DISCHARGE COEFFICIENT ITERATION 3- FINAL RUN OF DR. HOSDER HEAT FLUX AND RADIATION																													
	MACH 4				MACH 6																								
Segment #	M4 S1	M4 S2	M4 S3	Segment #	M6 S1	M6 S2				M6 S3				M6 S4				M6 S5					M6 S6					M6 S7
IDEAL Mdot/Mdot throat	0.529	0.471		IDEAL Mdot/Mdot throat	0.083	0.079				0.087				0.111				0.163					0.256					0.220
HOLE NAME	Mach 4 Hole 1	Mach 4 Hole 2	Mach 4 Hole 3	HOLE NAME	M6H1	M6H2	M6H3	M6H4	M6H5	M6H6	M6H7	M6H8	M6H9	M6h10	M6h11	M6h12	M6h13	M6h14	M6h15	M6h16	M6h17
Ideal (mdot/mdotsegment)	0.353	0.333	0.314	Individual Hole Mdot/Mdottotal	0.083	0.026	0.026	0.026	0.029	0.029	0.029	0.037	0.037	0.037	0.054	0.054	0.054	0.085	0.085	0.085	0.625
Iterated Hole Diameter (in)	0.531	0.368	0.516	Segment Mdot/Mdottotal	0.083	0.079			0.087			0.111			0.163			0.256			0.220
Equivalent Drill Bit	17/32	U	33/64	Iterated Hole Diameter (in)	0.71875	0.332	0.332	0.332	0.332	0.3125	0.302	0.3125	0.302	0.302	0.302	0.302	0.302	0.2812 5	0.2812 5	0.2812 5	0.5156
				Equivalent Drill Bit	23/32	Q	Q	Q	Q	Q	N	N	N	N	N	N	N	9/32	9/32	9/32	33/64
SIMULATION SOLUTIONS																													
Mass Flow Rate (kg/sec)	0.330	0.314	0.289	Mass Flow Rate (kg/sec)	0.447	0.105	0.091	0.194	0.101	0.126	0.130	0.096	0.105	0.177	0.090	0.122	0.129	0.134	0.181	0.189	0.416
Percentage of Mass Flow Rate(%)	0.354	0.337	0.310	Percentage of Hole Mass Flow Rate	0.158	0.037	0.032	0.068	0.036	0.044	0.046	0.034	0.037	0.063	0.032	0.043	0.045	0.047	0.064	0.067	0.147
Error	0.002	0.010	-0.013	Percentage of Segment Mass Flow Rate(%)	0.158	0.138			0.126			0.133			0.120			0.178			0.147
Temperature Outlet (K)	296.67	295.93	297.06	Error	0.895	0.732			0.456			0.203			-0.262			-0.307			-0.333
Outlet Mass Flow Rate (kg/sec)				Temperature Outlet (K)	295.49	295.09	294.81	295.70	295.36	294.96	294.88	296.42	295.21	295.54	295.68	295.09	295.75	295.56	294.97	295.39	295.37
DELTA T	3.475	2.728	3.863																		
				Hole DELTA T	2.290	1.891	1.609	2.503	2.161	1.758	1.684	3.221	2.007	2.336	2.483	1.893	2.554	2.356	1.770	2.187	2.166
				SEGMENT Delta T (Bulk)	2.290	2.130			1.846			2.470			2.300			2.082			2.166

While the error in certain segments is still high, especially towards the Mach 6 inlet side, the overall thermal distribution within the system is acceptable- the reason this is the case is that the hole sizing analysis did not consider the junctions between the segments, areas to which more flow is required due to the contact interfaces between the Mach nozzle segments being thicker and the material near them less effectively cooled. While the goal was to match the ideal distribution, by monitoring the thermal plots it became evident the system had been converged to within necessary levels of uniformity. The direct comparison of the first and last iteration of the process is shown in a series of image comparisons below. First, the cut plot view showing the right plane of the system in Figure 5.21 shows the temperature variation along the nozzle body. The surface temperature of the Mach 6 nozzle originally varies by approximately 100K, but in the finalized design the the temperature varies by approximately 50K. The surface plot of the two cooling

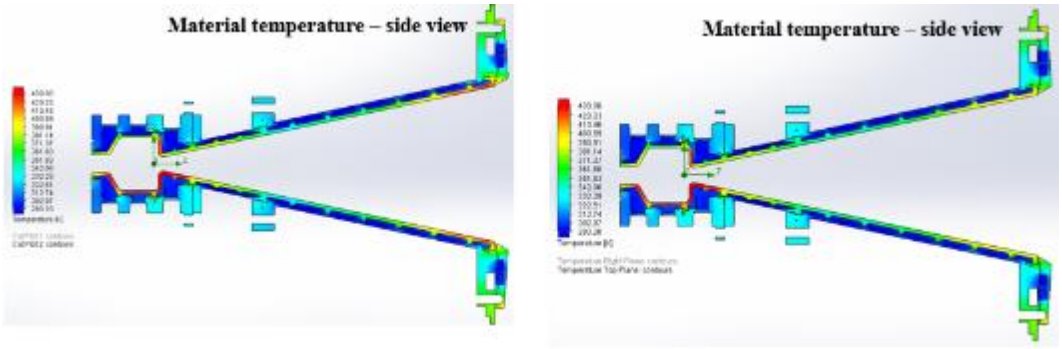

Figure 5.21: Sectional temperature plot of original iteration (left) and final iteration (right).

fluid surfaces, shown in Figure 5.22, shows a an obvious decrease in temperature variation along the Mach 6 segment, with the end of the segment averaging 375K as opposed to 425K in the original simulation shown on the left. The temperature of the cooling fluid was also affected, as shown in Figure 5.23, where the

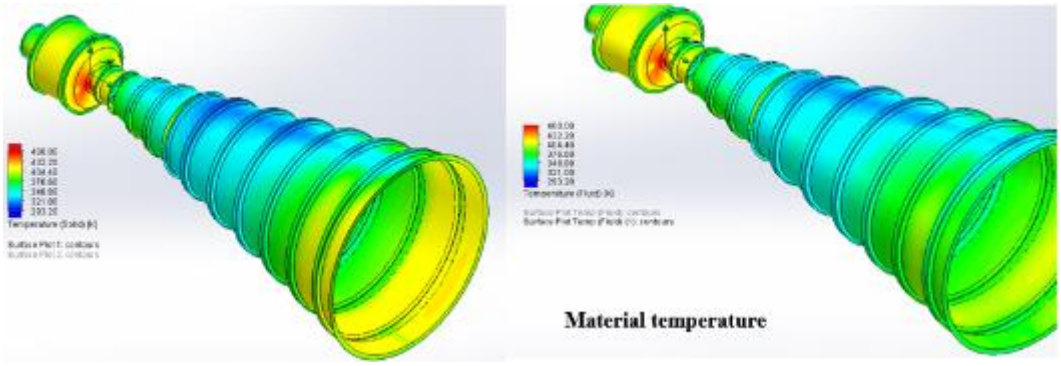

Figure 5.22: Surface temperature plot of original iteration (left) and final iteration (right).

temperature rise in the original water is shown to exceed 17 K in the bulk fluid flow, but in the final simulation only 10 K temperature rise is shown. Isolating on the exit fluid flow of the Mach 6 segment, which is shown in Figure 5.24, the fluid

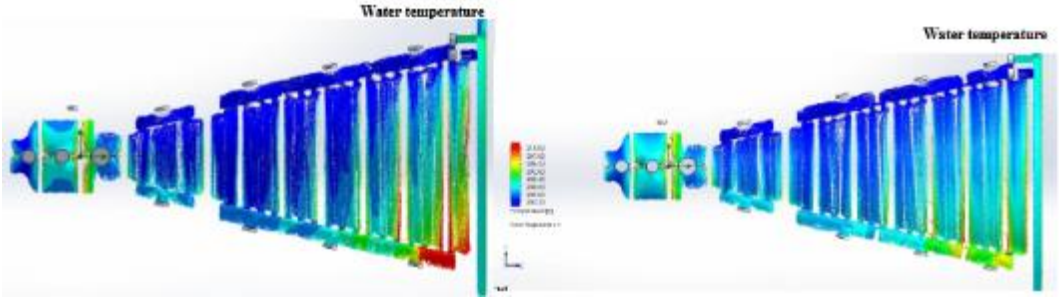

Figure 5.23: Side View Flow distribution temperature plot, comparison between first (left) and final iteration (right).

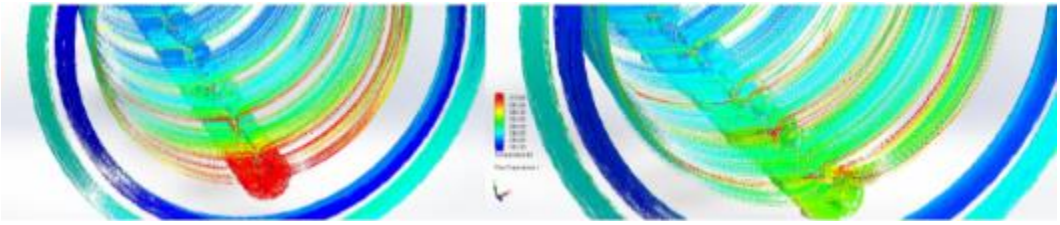

Figure 5.24: Flow distribution plot Mach 6 exit zoom of initial (left) and final and final iteration (right) showing fluid temperature difference.

simulation shows a significant decrease near the Mach 6 nozzle exit, where in the original iteration the fluid is nearly all above 310K, but for the final iteration only small traces of fluid achieve this temperature due to the increased flow rate to this segment. Once this decrease in temperature was achieved, the system was considered acceptable within design criterion, and fluid simulation progressed for the Mach 4 nozzle assembly.

The heat flux curve used for the Mach 4 assembly analysis is shown in Figure 5.25. The Mach 4 nozzle assembly was not iterated in the same fashion

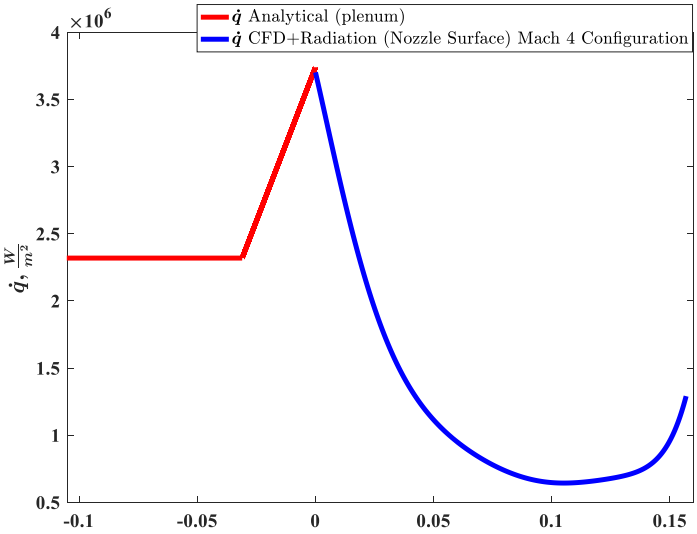

Figure 5.25: Mach 4 assembly axisymmetric heat flux curve for analysis.

because the iteration had already been performed on the cooling segment. As it can be seen, the radiative heat flux plays a larger role and as such the system was simulated to ensure that the component temperatures were acceptable. In this case, instead of breaking down the heat flux into segments, the original heat flux curve shown was directly implemented within the flow simulation as a function of distance from the throat- this creates a more realiztic heat flux, since the averaging method used for the hole iteration process asssumes the averaged value of the heat flux over the segment as opposed to a variable heat flux. The flow simulation cut plot for the Mach 4 nozzle is shown in Figure 5.26. As can be seen, the flow simulation showed higher temperatures in the Mach 4 segment in this case than in the previous simulations. The temperatures however are still not as high as the

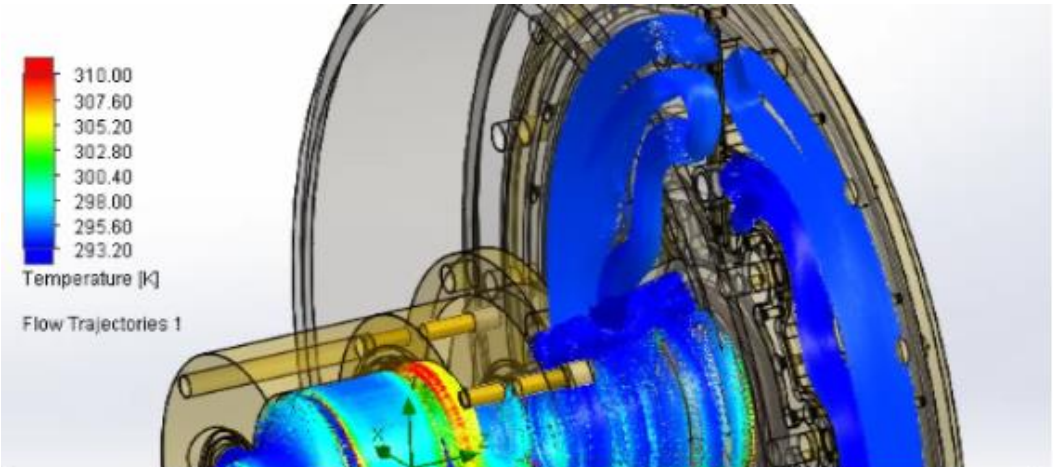

Figure 5.26: Flow distribution temperature plot of Mach 4 simulation.

nozzle throat segment. Because the nozzle and plenum segments have already been tested without failure, as long as there is a margin between termperatures of the downstream segments and those of the original segments, the analysis was

accepted. In this case, the material is still more than 100K below the temperature of the nozze throat. From the flow distribution plot shown in Figure 5.27, it is also

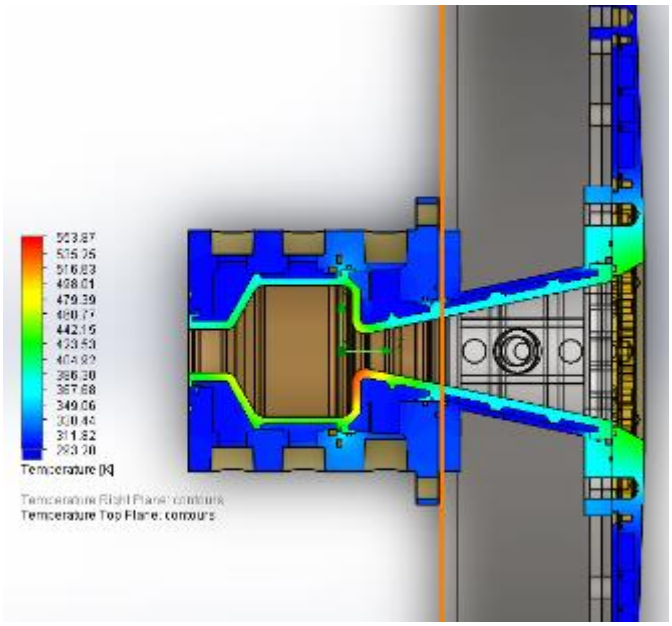

Figure 5.27: Mach 4 Flow Simulation Section Temperature Plot.

evident that the cooling fluid within both the Mach 4 segment and the Mach 4 cooling flange are not at risk of reaching local boiling (cavitation).

For the final simulations and FEA analysis, the heat flux curve as shown in Figure 5.19 was implemented instead of the segmented heat flux method, to ensure that the expected heat flux distribution would not cause unexpected variations. Furthermore two separate mock manifolds were modeled to consider the distribution of the cooling fluid based upon a parallel network, like what will be used within the model. The flow distribution of the resultant simulation is shown in Figure 5.28. The total pressure of the inlet manifold was applied based upon calculations performed by Prof. Maddalena's team, but was slightly lower than the

original applied total pressure from previous simulations. The total flow rate was applied to the outlet side equivalent to the expected flow rate within the network due to pressure losses of each primary manifold system. The resultant surface temperature on the cooling fluid interface is shown in Figure 5.29. While the value is slightly higher than the original system due to the flow distribution, the uniformity of the temperature plot verified the validity of the design. The flow simulation was then run for a variety of cases of pressure and flow rate that were

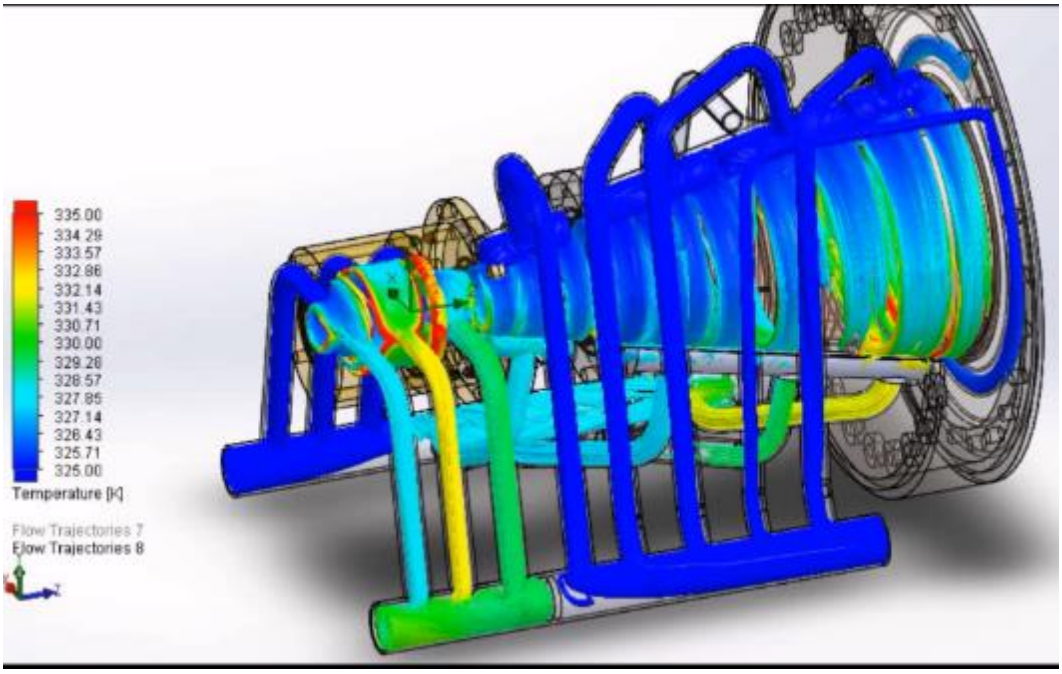

Figure 5.28: Finalized nozzle Flow Simulation fluid distribution plot with manifolds.

quantified by Dr. Maddalena's research group. These cases created an operational map for the cooling fluid system, within which any point of operation of flow rates and pressures were considered acceptable. All of the cases run in this method showed no significant increase in temperature of the solids or fluids that generated

a concern for further analysis. Once the flow simulation was finalized, the results were exported into Solidworks Simulation. After multiple iterations of the simulation setup and a series of failures, the final FEA setup was completed, and incorporated all bolting geometry, thermal and pressure loads from the simulation, external and internal pressure loads, and only two fixtures to constrain the model.

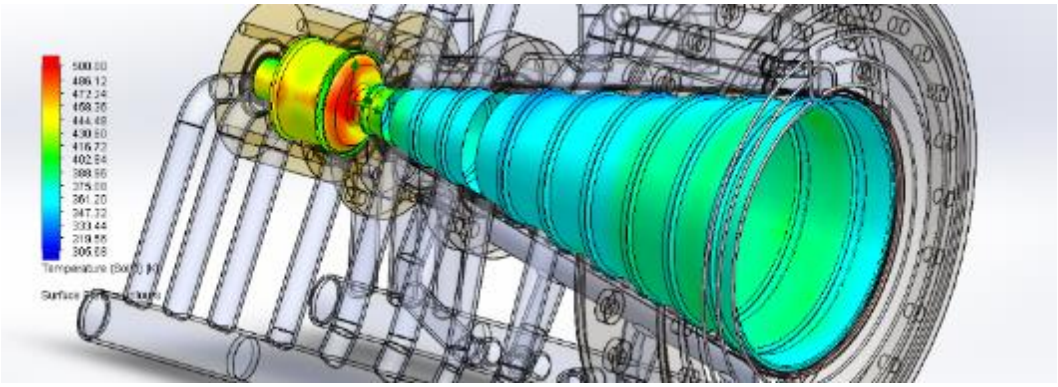

Figure 5.29: Finalized Nozzle Assembly Surface temperature plot at nozzle fluid interface.

Figure 5.30 shows the collection of all of the fixtures, pressures and fasteners incorporated into the final FEA. The top left image shows the application of the vaccum within the interior segments of the system. The top right shows the fixtures used to lock the degrees of freedom of the model, specifically a fixed geometry along the border of the large cylinder, where the system will connect to the test section, and a roller-slider fixture to prevent gravitational effects from pulling down on the plenum and connected bodies. Due to the problems with the previous indeterminate fixture setup of the first simulations, compression springs were added to the outer ring of the cooling flange to allow for thermal expansion of the internal

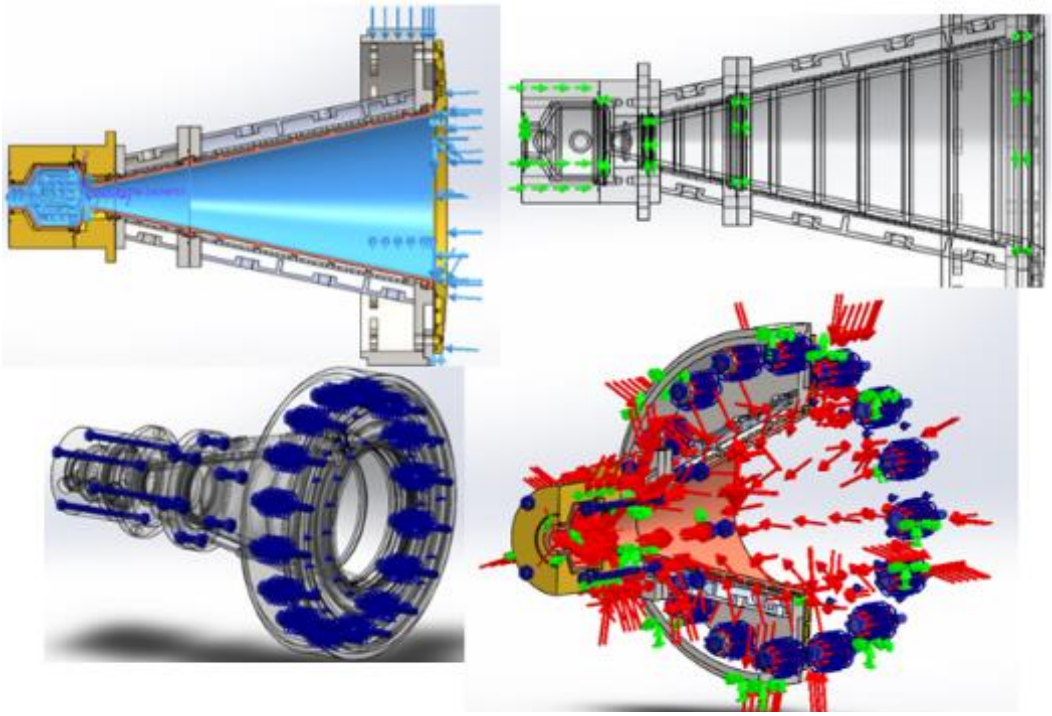

Figure 5.30: Combined images of all added pressures, fixtures, fasteners of the finalized FEA.

nozzle bodies, while maintaining the necessary thrust loading to keep the nozzle bodies in contact. The simulation was run with these settings, and the results showed that while there were local areas near fasteners and fixtures that approached the yield strength of the respective materials of the assembly (this is expected in the solver and is ignored), overall the system shows structural integrity for the worst-case scenario of operation. The side sectional view of the stress plot of the FEA is shown in Figure 5.31. The local stresses near the fixture point along the test section cylinder can be largely ignored due to the increased stresses near fixed geometry points. Figure 5.32 shows the stress plot of the system with a higher yield strength to show that the stresses in the cylinder of the test section, and within the bolting

points, are still safely below the yield strength of stainless steel, which is

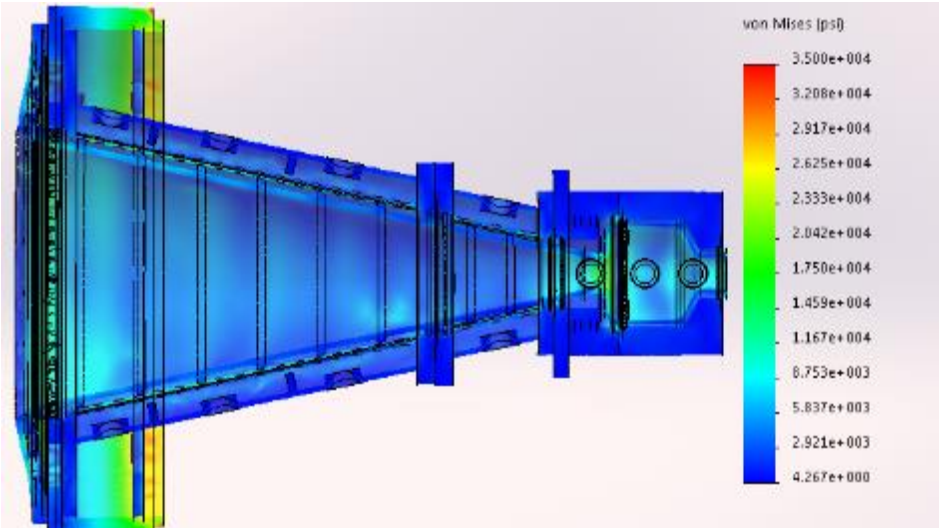

Figure 5.31: Side Sectional View of Nozzle Final FEA results.

approximately 50 ksi. Zooming in on the interface between the plenum and throat segment in Figure 5.31, which is shown in Figure 5.33, we can see localized stresses due to the contact pressure between these two components, and the heating they

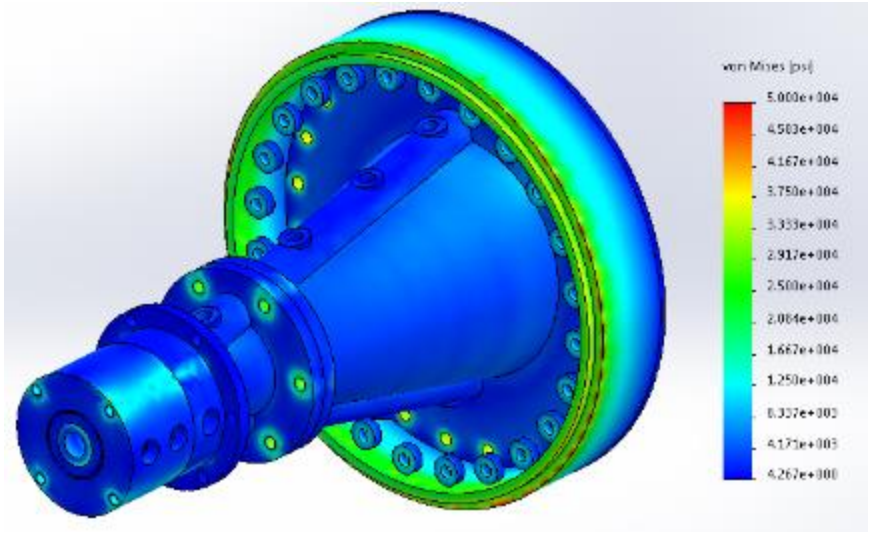

Figure 5.32: Stress Plot of Full Nozzle Assembly with increased yield strength scale.

experience. Figure 5.33 shows these contact stresses, which do match real world

deterioration on the current nozzle throat segment. From analysis of this pitting, it

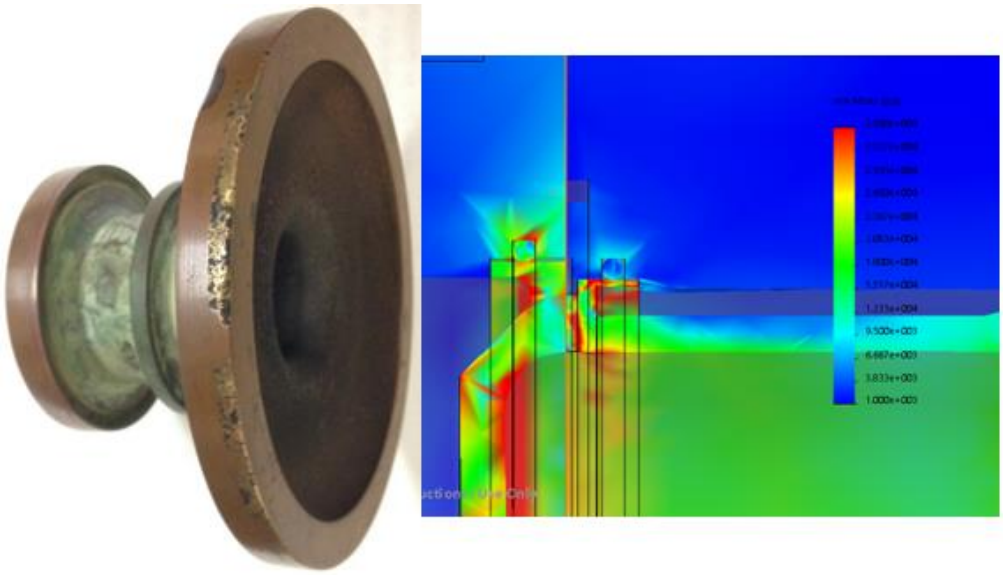

Figure 5.33: Nozzle throat segment showing material deterioration near plenum/throat contact interface, and FEA showing high stresses at the same location.

is due to the extremely high sustained temperatures during operation, and the pressures of the working fluid that are applied to either component. Overall, these two components are known to be wear parts at maximum facility operation, but considering that the facility has been operated at that level before and the internal components survived, degradation of this segment over time did not limit the completion of the system and its release to manufacturing

Chapter 6

Low-Reynolds Number Hypersonic Diffuser Analysis

The development of the diffuser for the AHWT-II Upgrade was critical for the functionality of the facility. While the internal geometry may seem relatively simplistic, the convergence angle, throat diameter and overall length, and divergence angle and exit diameter were critical for the recovery of pressure before the fluid enters into the vacuum manifold. The system, before the arc-jet is started, will be pumped down to a very low pressure by the vacuum pump system. Upon starting the system however, the diffuser serves to allow for recovery of the pressure of the fluid. The vacuum pumps work to remove volumes of fluid, but the pressure and resultant density of the fluid are directly related to the efficiency of the pumping system- a lower pressure at the vacuum manifold inlet results in less gas removal from each cycle of the vacuum pump, and thus the higher the pressure, the more fluid mass is removed with each pump cycle.

The entire purpose of the diffuser system is to reduce the flow to subsonic speed as efficiently as possible. Hypersonic diffusers at low-Re currently represent a significant challenge and only a very limited number of publications on the topic is available in literature. . This system was probably the most critical design for the facility functionality; for example, even a slight increase in the pressure recovery of the diffuser due to its geometry results in a reduction in the number of (very expensive) pumps necessary to maintain a specific backpressure.

The preliminary analysis of the diffuser geometry based on an extensive analysis of available literature as well as decisions on specific design aspects was performed by the research group of Prof. Maddalena. The convergent and divergent angles and dimensions, along with the throat diameter and length, were chosen by the research groups as previously stated. Then the geometry was passed to the research group of Dr. Hosder at Missouri University of Science and Technology for non-equilibrium, chemically reacting CFD analysis. The CFD simulation was performed over several months for three initial backpressure boundary conditions, 10 mbar, 30 mbar, and 50 mbar. The inlet boundary condition for each was the exit results of the Mach 6.5 Nozzle. The initial results returned to Dr. Maddalena's research group were analyzed and then broken down for simulation based upon the segments of the diffuser. The diffuser design that was sent for analysis is shown in Figure 6.1 Below. The throat and exit segments were each broken down into three segments for manufacturability and flexibility of future facility modifications. As can be seen in Figure 6.1, the throat length is 150 inches and the total diffuser length is 256 inches, approximately 6.5 m long. \For the CFD analysis, the entire diffuser, along with test section, the computational domains were modeled with several grid topologies, such that the exit conditions of the diffuser served as the inlet boundary condition and the initial outlet boundary conditions were the three backpressure values mentioned above [15]. Furthermore, a wall temperature boundary condition

within the flow was defined for the diffuser body at 400 Kelvin, which will become important in discussion on the thermal plots of the cooling system analysis.

Pressure and Mach number plots for the three backpressure cases generated are shown in Figure 6.2. As it can be seen on the left plots the shock train travel upstream as the backpressure is increased. For our cases, the

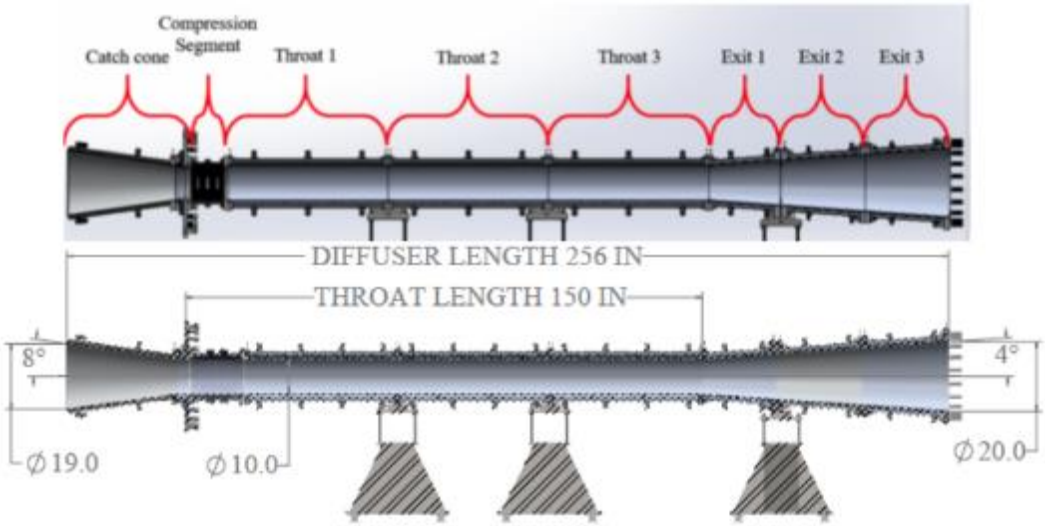

Figure 6.1: Primary Diffuser Dimensions and segment breakdown provided for internal CFD fluid analysis [15].

maximum backpressure probed in the simulations is 50 mb (the inspection of the plots suggests that an higher backpressure can be maintained).

The following work is based on the 50 mb case. The normal shock location is critical when analyzing the heat flux, since it is the location of the maximum heat flux within the system for all pressure cases, as is evident in Figure 6.3. For the

higher back-pressure case, 50 mbar, the higher pressure of the fluid results in a larger heat flux at the wall. This is also evident in the final results of the non-

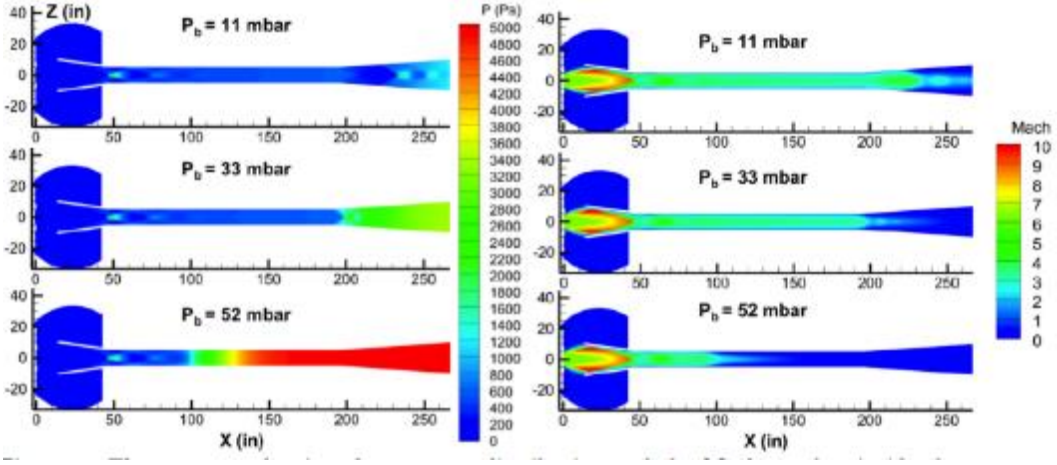

Figure 6.2: Plot of Mach number (right) and Pressure (left) within the fully catalytic simulation for all three backpressure cases [15].

catalytic and fully catalytic simulation cases shown in Figure 6.3. The results of the 50 mbar case show a drastic heat flux within the throat segment. There is a caveat to this heat flux curve however; the heat fluxes shown in Figure 6.3 were based upon a stable wall boundary condition holding the wall temperature to 400 K. This means that if the heat flux would result in a local position of the throat to exceed 400 K, the heat flux will decrease- as such the wall temperature will stabilize somewhere just above 400 K.

The outputs from the simulations also included the plot of the translational and vibrational temperature of the fluid along the system, as shown in Figure 6.4. In this case it is evident that the translational temperatures of the fluid (right) are slightly higher than the vibrational temperatures of the fluid, and in both cases the

temperatures rise drastically after the normal shock, which is expected. This is the

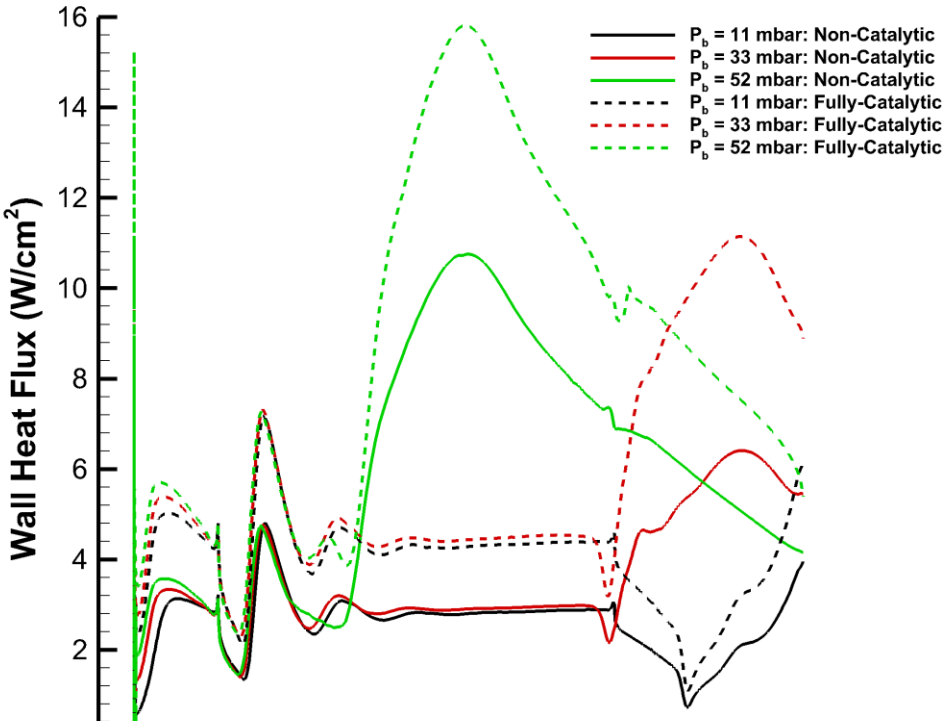

Figure 6.3: Non-Catalytic and Fully Catalytic Heat Flux results from non-equilibrium, chemically reacting CFD simulation for three backpressure conditions [15].

reason for the significant heat flux spike seen in Figure 6.3.

Due to a setting that was used by default in external hypersonic aerothermodynamics the initial set of simulations used super-catalytic wall as boundary conditions instead of a fully-catalytic wall.

The fully-catalytic condition is the correct one. The initial simulations were run with the super-catalytic case and the thermal management system was shown to be adequate with a large range of operation conditions. Upon the discovery of the heat flux increase in the fully catalytic case, approximately 50 percent, the

simulations were re-run and many concerns developed in the cooling capacity of the system due to unwanted flow effects within the cooling system design requiring iteration to reduce cooling fluid circulation within the jackets of the system, which will be discussed below.

The process of the cooling system analysis for the diffuser system followed the same process of the nozzle design system, except due to the size of the system the individual segments were simulated instead of the assembly. The material for

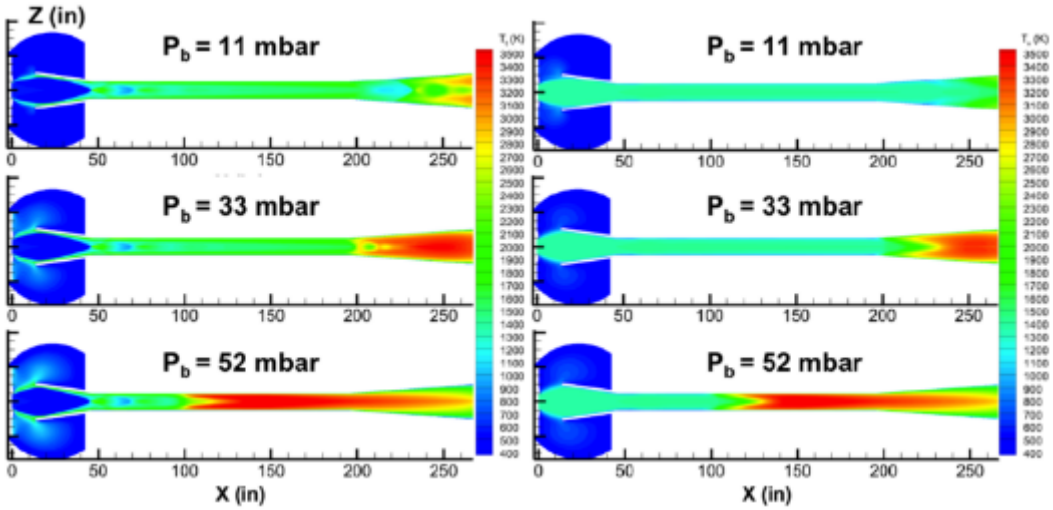

Figure 6.4: Translation (left) and Vibrational (right) Temperature profiles for the Fully Catalytic CFD simulation condition [15].

the catch cone bodies was debated based upon cost, structural integrity and thermal conductivity. Due to the potential for considerable localization of peak heat flux due to shockwaves in the diffuser, the decision was made to make the diffuser segments out of aluminum. This decision considered both thermal conductivity and cost of materials. The only concern posed was the yield strength of the material for

the segments, due to the necessity of welding in the designs. Aluminum yield strength drastically decreases due to welding, and without proper heat treat the system would be incapable of handling high pressure. After discussion with the manufacturer, the decision was made to centrifugally cast the interior bodies and flanges as one piece and cut and weld the external cooling sleeves. This results in a much larger surface area of welding away from any locations of high heat flux, such as the internal body, which improves the yield strength in areas of concern.

For the setup of the cooling fluid simulations, the decision was made to connect the diffuser in series after the anode/cathode and nozzle. The cooling fluid passes through the upstream nozzle system, then is passed into a parallel manifold running along the length of the diffuser that distributes it to the individual ports of the diffuser assembly. Due to being downstream of the nozzle the inlet temperature will be the outlet temperature from the upstream system, and the inlet pressure will be the outlet pressure from the system- from analysis of the research group of Prof. Maddalena, the pressure out of the arc-heater system is not sufficient to fulfill the requirements of the diffuser manifold network and as such, a pump must be included prior to the diffuser coolant manifold to boost the fluid pressure. As such, the inlet pressure of the system is then dictated by the pump choice, which after analysis from the research group was chosen to be 9 atm. From this determination the inlet pressure and temperature and the mass flow rate through the diffuser

system were defined. The boundary conditions input into each of the assembly segments are shown in Table 6.1.

Table 6.1: Input boundary conditions for Flow Simulation of diffuser assemblies.

	Catch Cone	Throat segment	Exit segment 1	Exit segment 2	Exit segment 3
Mass Flow (GPM)	9.69	32.61	21.68	21.74	21.74
Total Pressure (kPa)	6.080	9.032	9.032	9.032	9.032

The final breakdown of the fully-catalytic heat flux curve applied to each segment is shown in Figure 6.5. There was no initial heat flux curve available before receiving the heat flux from the simulation of the diffuser, so once the heat

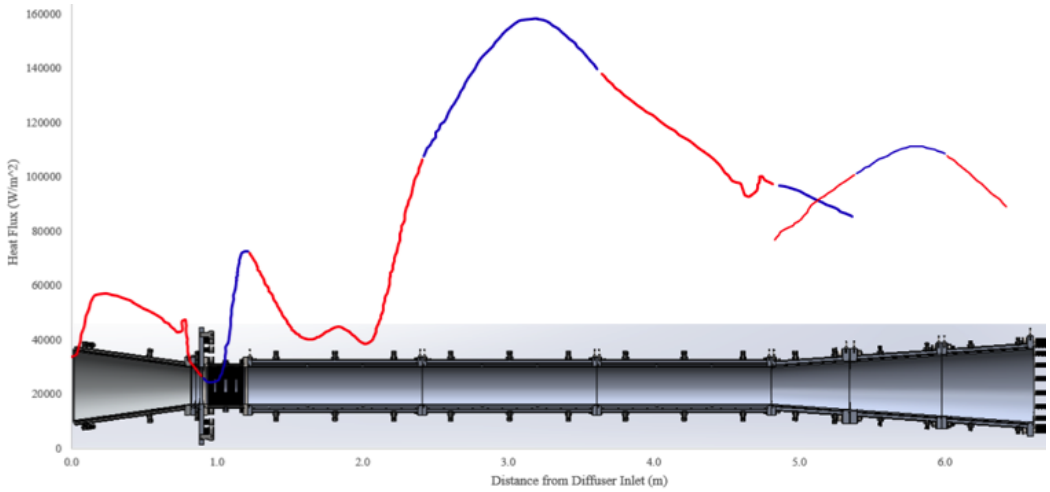

Figure 6.5: Heat Flux curve breakdown in Figure 6.3 superimposed onto diffuser segments (including both 50mbar case for upstream components and 30 mbar heat flux for exit segments) [15].

flux plot shown in Figure 6.3 was presented, the simulations began, starting with the catch cone. Early on in the analysis of the catch cone it became evident that due to the large surface area and convergence angle, the thrust generated by the cooling

fluid pressure on the catch cone inner surface would be over 25,000 lbf which could cause failure of the catch cone segment. As a result, the pressure for the catch cone

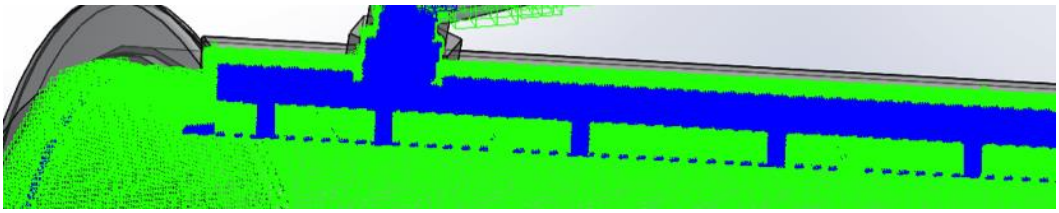

Figure 6.6: upper manifold mesh of catch cone in Flow Simulation analysis [15].

segment was reduced to 6 atm, which will require a pressure reduction from the input system. The simulation of the catch cone progressed with the catch cone assuming this lower input pressure, and the Flow simulation was set up and the system was meshed. Due to the size of the system, the mesh refinement within the system was concentrated near the fluid inlet and outlet manifold and along the solid/fluid interface on the inner catch cone body. An example of the fluid and partial mesh near the fluid manifold is shown in Figure 6.6. As can be seen, there are a high number of partial cells due to the scale of the system and the total number of cells allowed for the simulation- as such many of the cells in the analysis are partial cells as discussed in Chapter 4. The total number of cells for the diffuser segments, including the catch cone, varied between 2.5 to 5 million cells. The initial results of the Catch Cone are shown below in Figure 6.7 and 6.8.

From Figures 6.7 and 6.8 it is evident that significant flow stagnation occurs within the catch cone body, resulting in a high temperature location on the body

near the catch cone entrance. This locally high value is of some concern due to

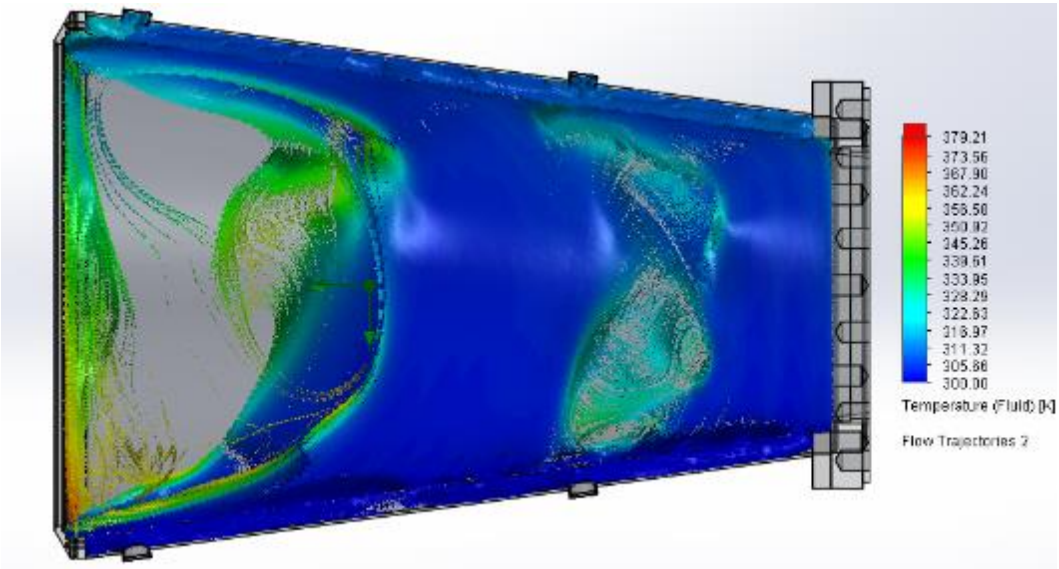

Figure 6.7: Initial Flow distribution of Catch cone Flow Simulation.

non-uniformity of the system, but the temperature of the interior surface is still well below the boiling point of the fluid within the cooling channel, so there is no

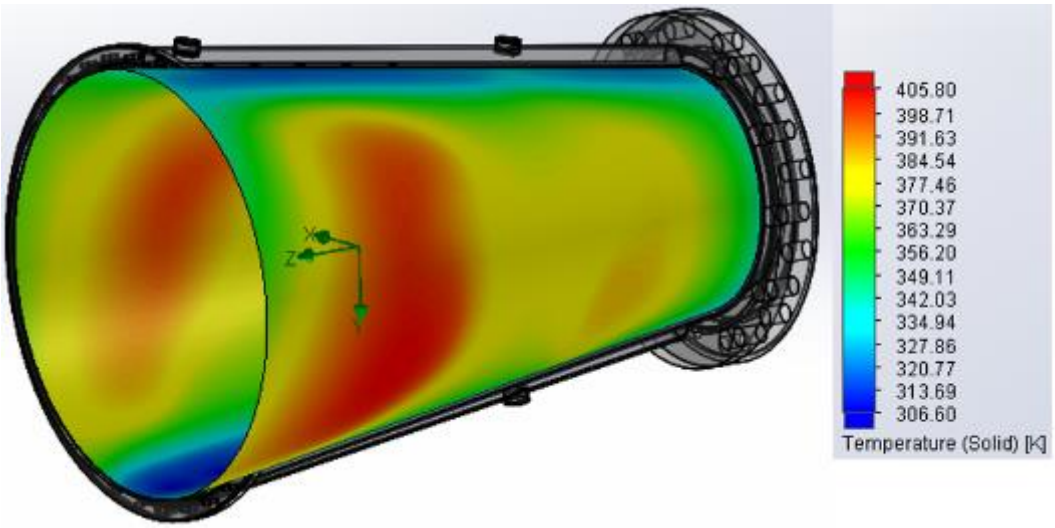

Figure 6.8: Initial Catch Cone Flow Simulation internal surface temperature.

concern of boiling at this point. Furthermore, at this location where the internal

surface is above 400K the heat flux will decrease, due to the discussion above of the imposed wall surface temperature. Multiple iterations were performed with the original super-catalytic (referred to as non-catalytic above) heat flux, and the hot

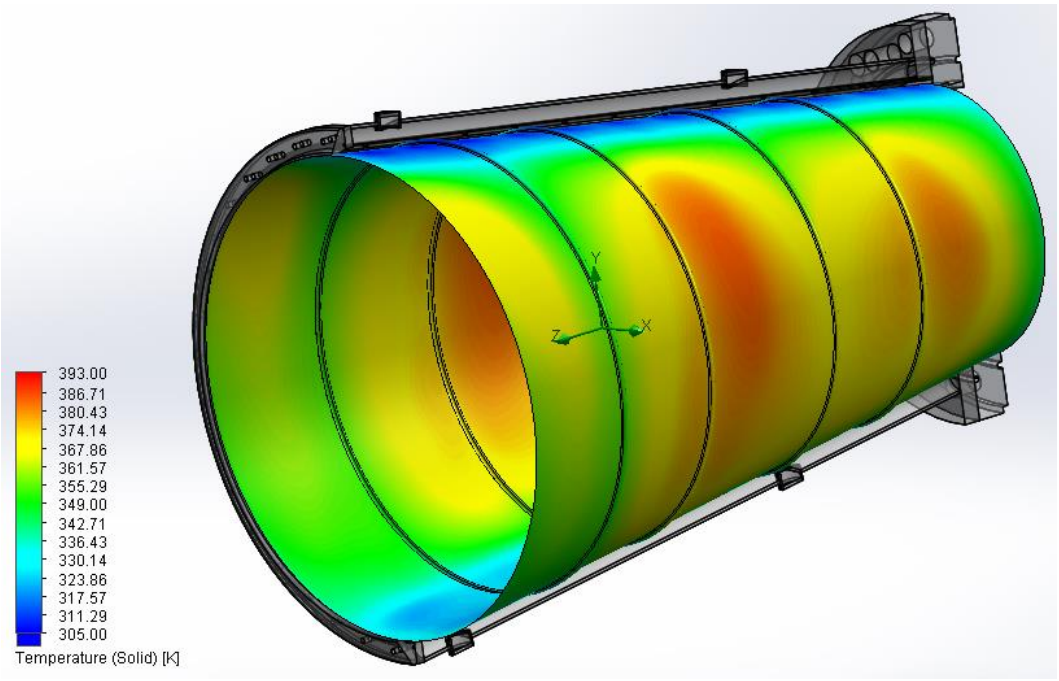

Figure 6.9: Surface Temperature of Final Iteration of Catch Cone Cone with original (super-catalytic) heat flux.

spots were reduced until the surface temperature decreased to below 400 K. An example of one of the final iterations of the flow simulation with the initial heat flux values is shown in Figure 6.9. The simulation of the throat segments was also underway before it was realized that the fully-catalytic simulation, which was completed after the super-catalytic resulted in a higher heat flux. The surface temperature plot of the cooling fluid interface with the interior body of the original

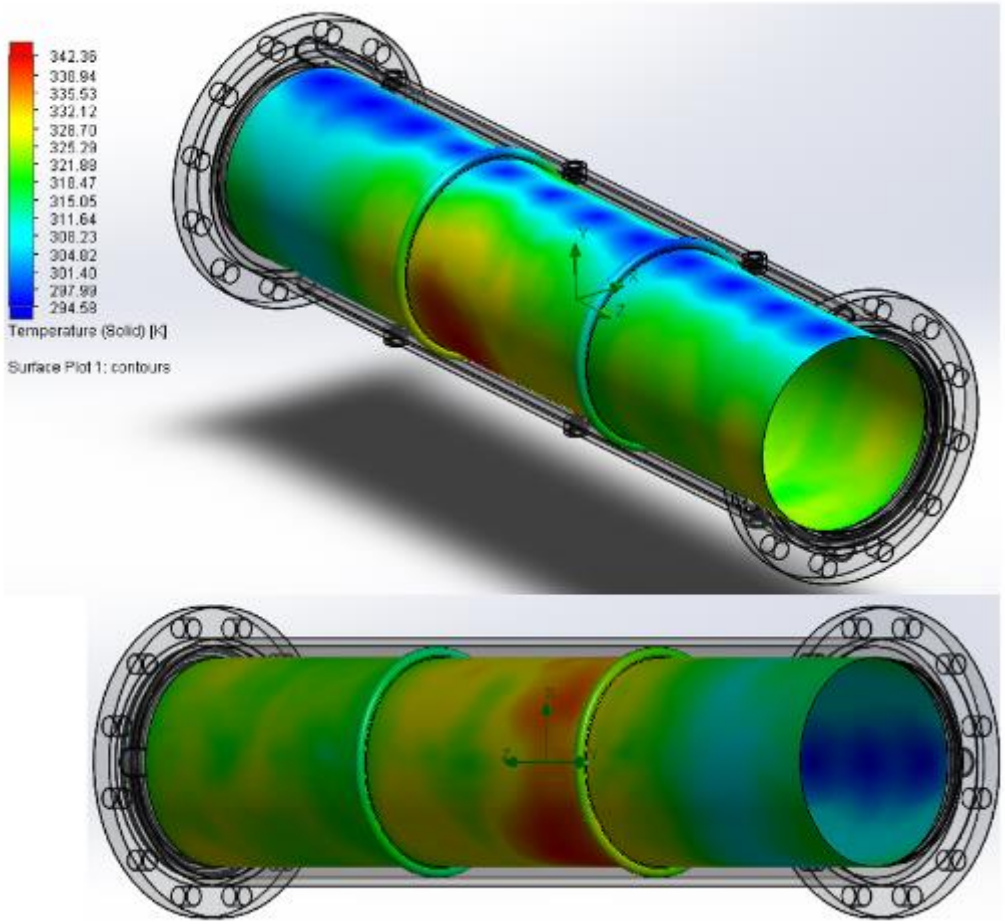

Figure 6.10: Original Throat segment Flow Simulation showing the cooling fluid interface surface temperature from the original non-catalytic heat flux shown in Figure 6.3.

throat segment simulation is shown in Figure 6.10. While there is a local hot spot due to fluid circulation within the segment, the surface temperature shown here, which represents the highest possible temperature of the cooling fluid, is only 345K, which is near 100 K below the boiling point of water at 9 atm pressure. Since at the time this circulation was acceptable, the simulations were not progressed further.

Shortly after the completion of the throat Flow Simulation shown in Figure 6.10, it was determined that the fully-catalytic heat flux case was the worst-case scenario, and therefore was the heat flux case that needed to be simulated. The Flow simulations again began with the catch cone, the initial result of which is shown in Figure 6.11. It is evident that the increased heat flux significantly changed the

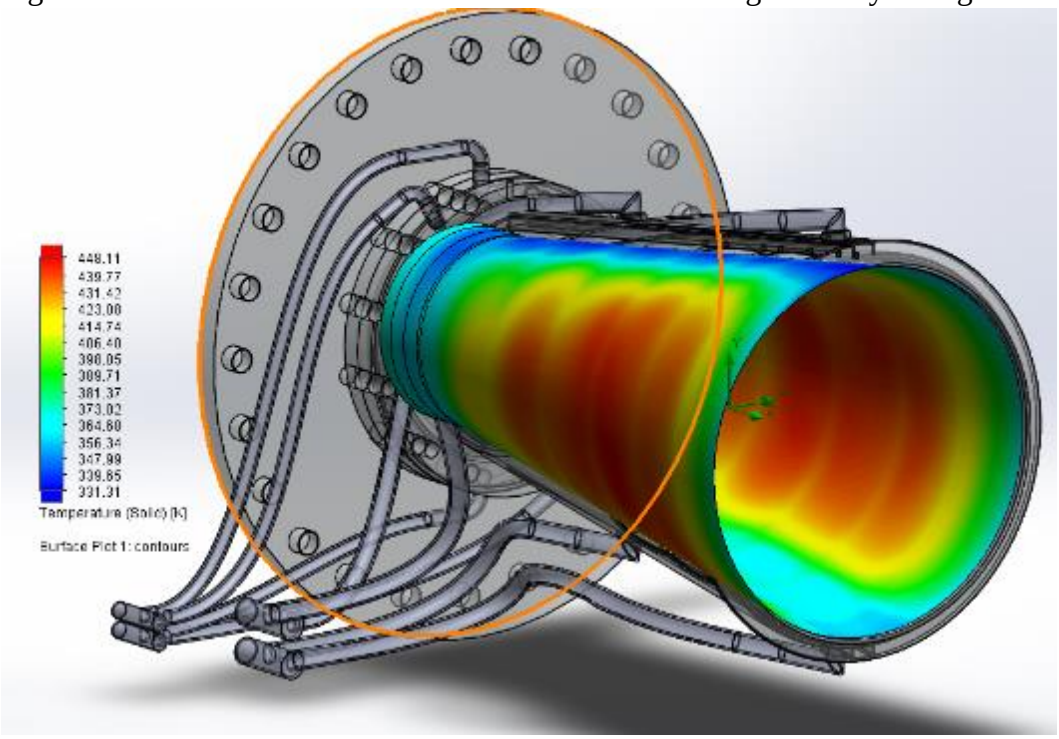

Figure 6.11: Initial Iteration of the catch Cone with Fully-catalytic heat flux implemented.

results of the system, such that the maximum surface temperature of the inner body interior surface increased to nearly 450 K. This is significantly higher than before and results in temperatures at the cooling fluid interface to reach the boiling point of the fluid. As such, since the circulation of the fluid had previously been evident, the simulations of the catch cone progressed and focused on the elimination of a large portion of the cooling fluid circulation. It should again be noted that for any

point on the interior body of the diffuser, the heat flux above 400 K decreases, and as such the recorded temperatures for this simulation in places above 400 K were higher than they would be in experiment because the applied heat flux to the interior surface of the diffuser components is not variable. The throat simulation was also re-run for purposes of determining how great of an issue the increased heat fluxes were, and the results of the interior surface plot on the throat segment for the peak heat flux in Figure 6.3 are shown in Figure 6.12. the maximum temperature within the throat segment, the location of the greated increase in heat flux between the super-catalytic and fully-catalytic simulations, shows a maximum temperature rise of over 100 K. The maximum surface temperature is above the boiling point for the

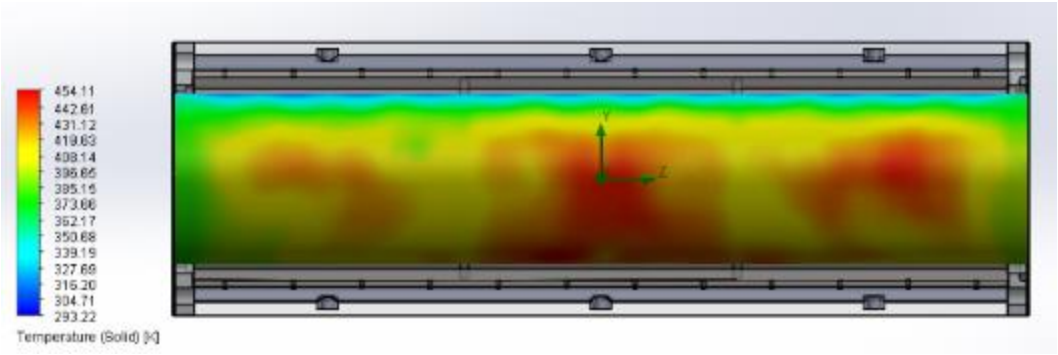

Figure 6.12: Diffuser Throat Initial Flow Simulation with Updated Fully-catalytic Heat flux.

flow in the throat segment, which is 9 atm, and as such there were significant concerns with the problem of circulation within the segment that needed to be addressed.

Many attempts were made after the increased heat flux to modify the system geometry, but due to concerns with toleances in manufacturability and other

concerns, the system designs progressed with the inclusion of rings to be welded to the inner body to establish cooling channels similar to the nozzle. Furthermore hole sizing and position of the segments was iterated based upon the consideration that for simulations in which the interior surface temperature was greater than 400 K, the body would see a reduction in the heat flux in real flow conditions, and as such as long as these internal surface temperatures were kept at or below the boiling point of the fluid, the system was considered acceptable, even with circulation contidions. Based upon this consideration, the individual assemblies were iterated within time constraints to acceptable conditions. The catch cone simulations progressed until the results shown in Figure 6.13. The circulation present within the system is still evident, but the surface temepratures are below 400K, which

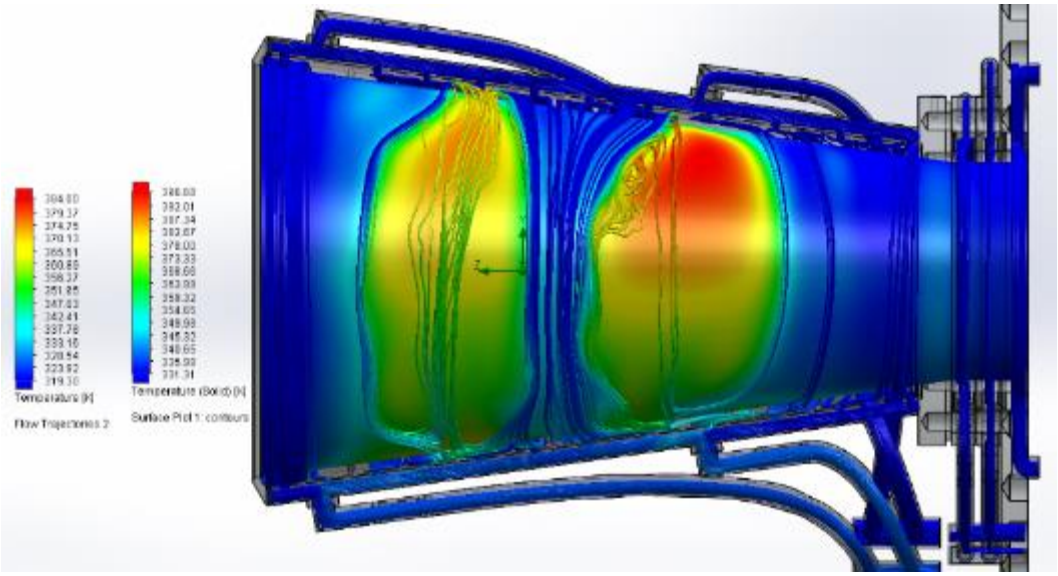

Figure 6.13: Final Flow Simulation of Catch Cone with fully-catalytic heat flux.

means that the fluid within the system will not reach above the boiling point, which

is 20K higher. Figure 6.13 was the result of a series of iterations attempting to adjust the hole sizing of each hole along the manifold to distribute flow more effectively based upon prior simulation results, but no matter the hole sizing and distribution, there were still some circulation regions present in all bodies.

The simulations then progressed to the exit segments,which at the time had yet to be simulated. The heat flux curve shown in 6.5 shows a combination of the 30 mbar and 50 mbar cases. As such, depending on the actual back pressure in operation the peak heat flux could be anywhere along the system representing the line connecting the two peak points on this curve. As a result to consider a scenario that allows for the location of the shock and the resulting peak heat flux to range anywhere between these points, a linear plot was constructed between these two vertex, and the exit segment simulations were run using this consideration. The original fully catalyitic plots of both the 50 mbar case and the 30 mbar exit segment cases is shown in Figure 6.14, along with the linear segments representing the applied heat fluxes for each of the exit segments. This is a somewhat unrealistic case due to the cumulative heat rate into the segment being less than the linear plot, but the simulations were progressed with the caveat that as long as the simulation results showed temperatures at or below the boiling point of the system, the simulation was considered acceptable. Beginning with Exit segment 1, the simulation was run with the linear heat flux. The results were not encouraging, with the temperature of the inner surface in most places exceeding 450K as shown in

Figure 6.15, but some of this was due to circulation within the cooling cavity. The simulations were iterated until the flow distribution across the body was uniform,

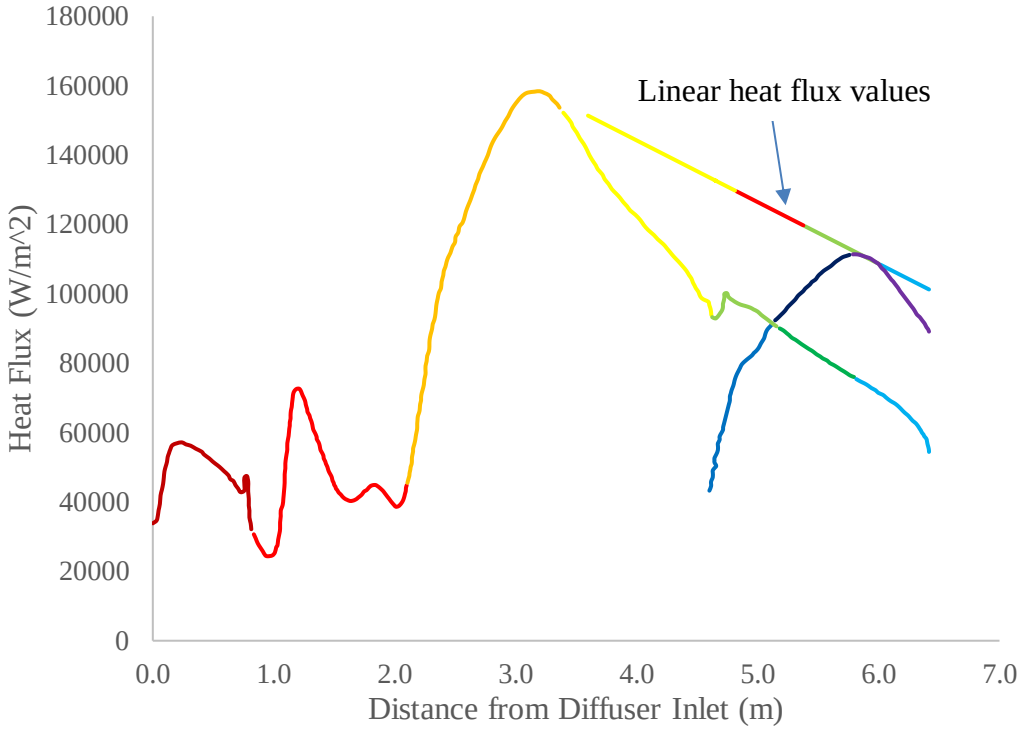

Figure 6.14: Final Heat Flux Plots for all conditions of Flow Simulations.

and once this was the case, the fluid temperature was shown to be below the boiling point- since this is the highest heat flux of the exit segments and is unrealistic, the fluid temperature plot shows that the temperatures along the inner surface were acceptable with consideration to the excessive applied heat flux. Mentioning again that if the internal surface temeprature exceeds 400K, the heat flux in the segment decreases, and as such as long as the flow remains below boiling, there is still an acceptable safety factor for fluid boiling. The final fluid simulation flow

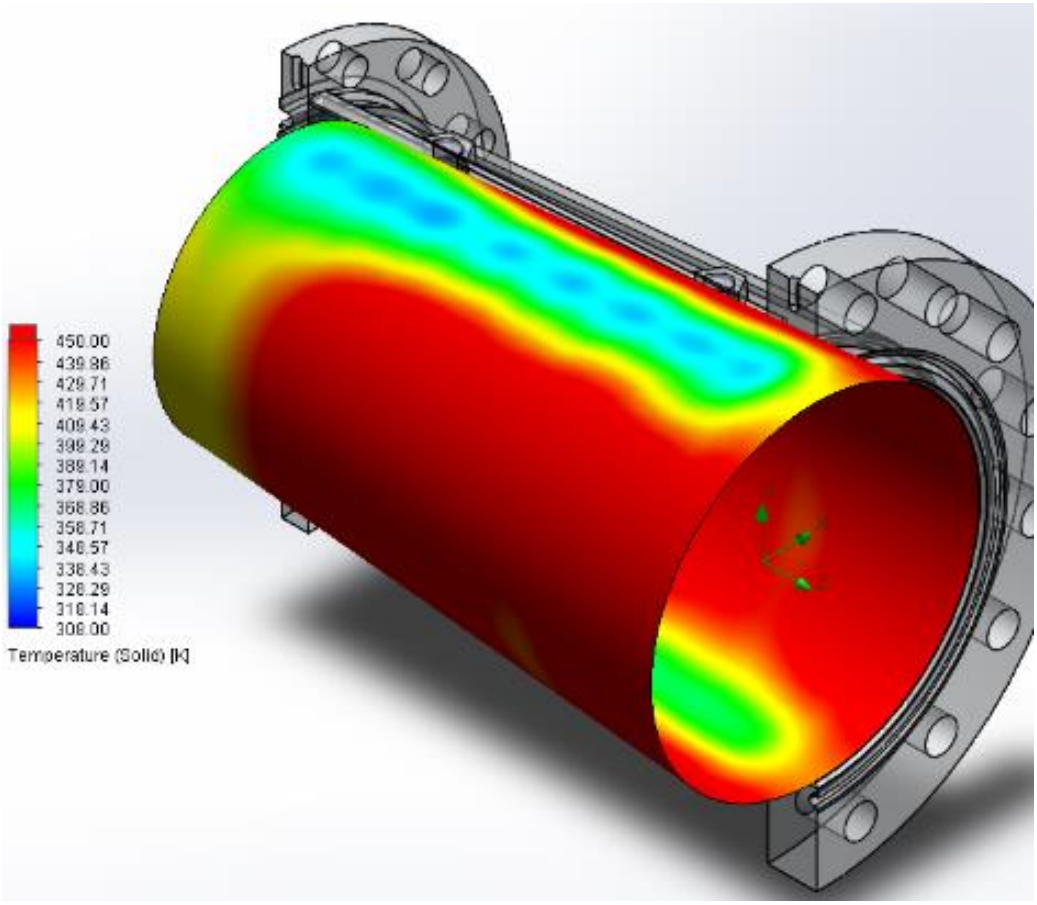

Figure 6.15: Initial Linear Heat Flux Simulation showing the most of the interior surface above 450 K.

distribution is shown in Figure 6.16. As can be seen, the fluid pathlines somewhat follow the geodetic lines of the conical body, but the flow remains attached to the ends and there is no circulation present within the flow. The actual worst case scenario heat flux in this segment would be at least 20 percent less than the case shown (due to the curvature of the peak heat flux as opposed to a linear plot), which in the worst case scenario necessistates a slight increase in the fluid flow to this segment alone. Next the Exit segment 2 simulation was run, and the results of the

interior surface plot, shown to the left in Figure 6.17, show that only small portions

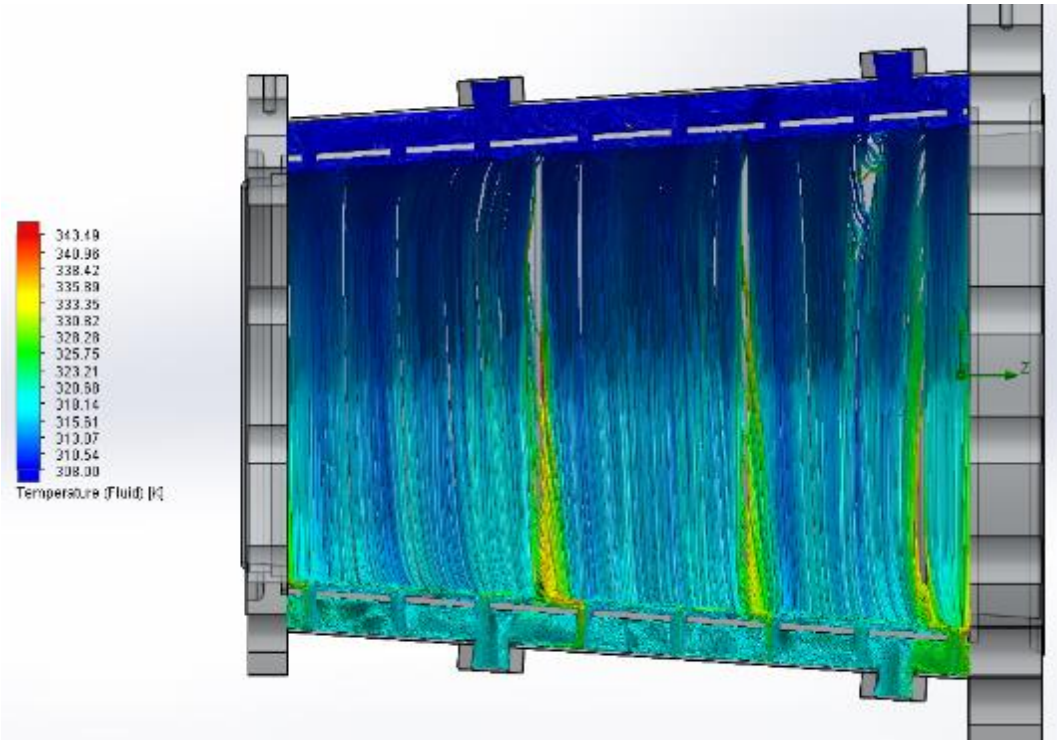

Figure 6.16: Flow distribution plot of exit segment 1 showing no circulation within the body.

of the surface temperature exceed 400 K, and the fluid interface shown on the right maintains temperatures well below boiling, near 370 K at maximum. The images shown in Figure 6.17 are the result of the iteration process concluding with stable flow through the cooling sleeve with no signs of circulation. The flow distribution side plot is shown in Figure 6.18 below, where it is evident there is no circulation and the bulk fluid flow is well below boiling point. Because of the results show in Figure 6.17 and 6.18, the Exit segment 2 assembly was considered acceptable for design conditions. The simulation process then proceeded to Exit segment 3, which considering the lower heat flux and similar mass flow rates, was not expected to

result in considerable concern. The flow simulation for exit segment 3 progressed,

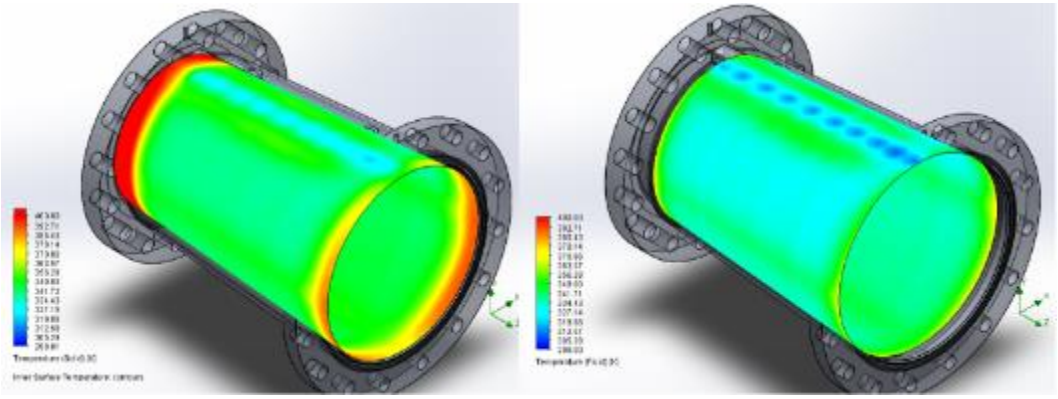

Figure 6.17: Internal Surface temperature plot (left) and exit fluid interface temperature plot plot for Exit segment 2 Flow Simulation.

but due to the size of the segment it was difficult to get the fluid flow to follow the

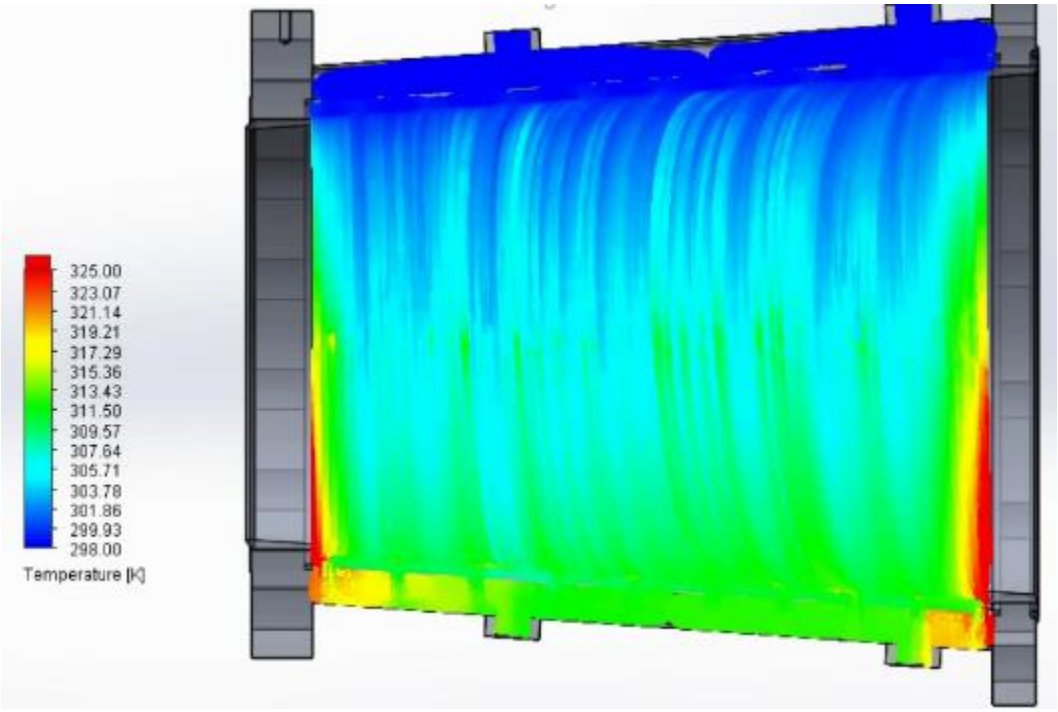

Figure 6.18: Flow distribution plot of Exit Segment 3 cooling fluid.

geodetic lines. The resultant fluid flow is shown in Figure 6.19. Although the fluid temperature is high, the simulation results showed that this was due to the low speed

of the fluid, and the fluid temperature of the system was below 400 K, as in exit segment 2.

From these flow simulations, all three exit segments were considered complete from an analysis standpoint based upon the iterated results. Next attention

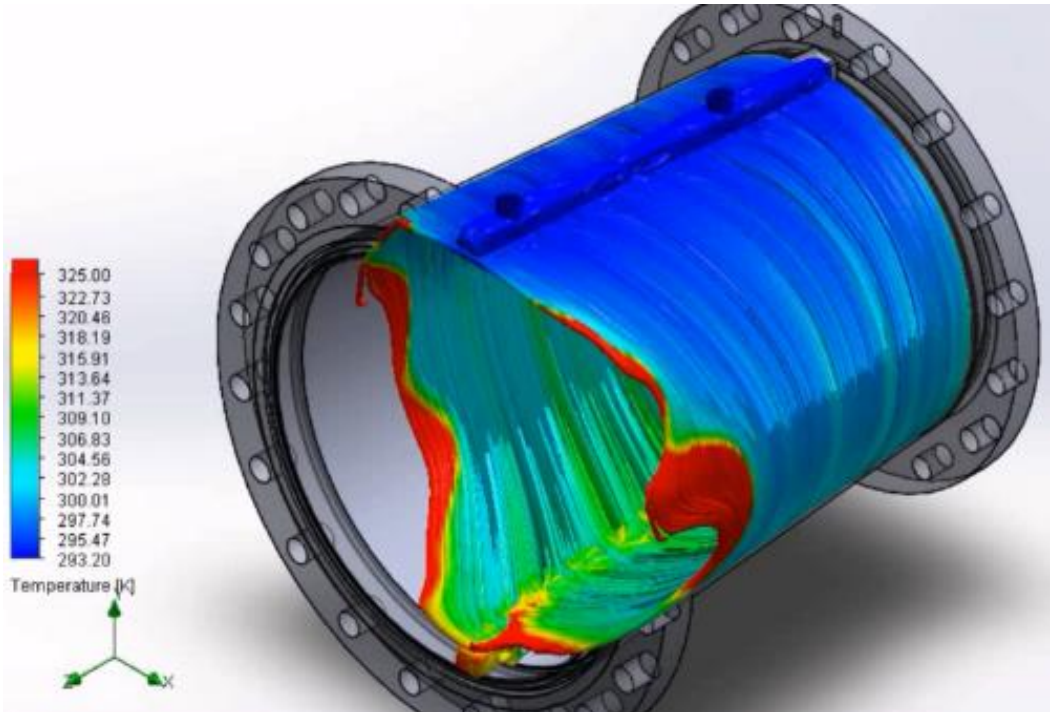

Figure 6.19: Exit segment 3 Flow distribution showing separation form exit flange.

returned to the throat segment, which was expected to have the largest circulation issues. For manufacturing savings, the throat segment was designed to use two off-the shelf schedule pipes for the main bodies. As such, the cooling channel dimension was much larger than the other conical segments, resulting in an increase in the area ratio between the inlet ports and the cooling channel cross sectional area. This resulted in significant circulation within the cooling channels, causing the

internal temperature of the system to drastically increase. The initial simulation of the body is shown in Figure 6.12 and from there the system was iterated repeatedly, and eventually another inlet and exit NPT port were added to assist in flow distribution, bringing the total to 4. Furthermore, to consider the worst case scenario, the heat flux of the diffuser throat segment was modified during analysis to balance around the peak heat flux point; the applied heat flux for the final throat design is shown in Figure 6.20. This is the worst case senario possible for the system considering the location of the shock within a specific segment, not split between two as shown in Figure 6.14. In this case, the temperature of the segment

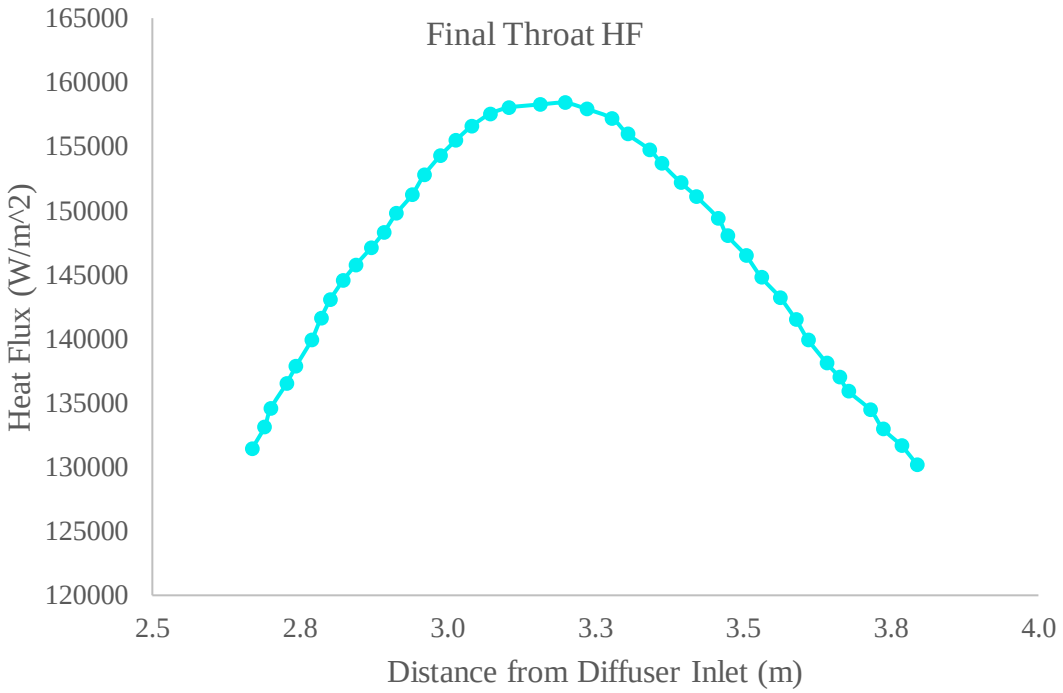

Figure 6.20: Final Heat Flux curve applied to the throat segment.

was again intended to be minimized along with the circulation. The final flow

distribution of the throat segment, after nearly a dozen iterations involving modification of hole sizing in the manifold, is shown in Figure 6.21. AS can be

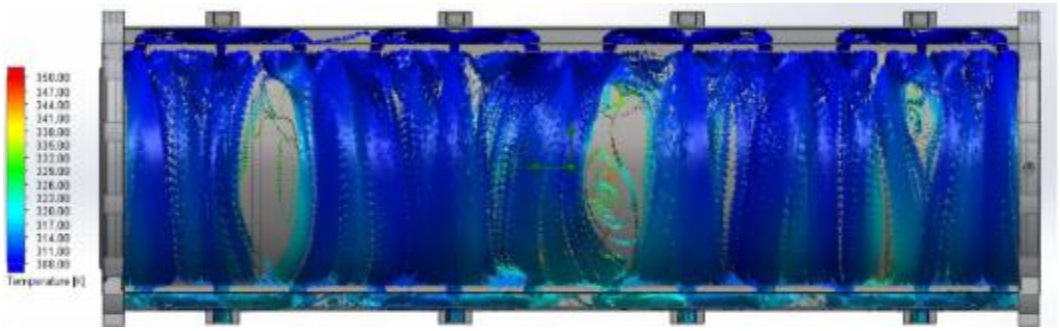

Figure 6.21: Throat segment Flow distribution final Flow Simulation.

seen, there are still regions of circulation within the throat segment, but they are much smaller and the overall flow distribution is far closer to the intended system than the initial simulation. The surface temperature on the inner body of this flow simulation, shown in Figure 6.22 and compared at the same temperature range as Figure 6.12 (also shown in Figure 6.22) shows that the surface temperature on the internal body of the throat was reduced to a maximum of 415 K for the worst case scenario, which is well within range of the goal.Since the heat flux will decrease for surfaces above 400K, and the boiling point of the 9 atm fluid is near 445 K, overall the throat simulation was concluded, and the flow simulation of the diffuser were complete.

The structural analysis of the individual segments was the last thing to be considered, however due to geometry and manufacturing design of the system the only assembly of concern that will be discussed in this Thesis is the catch cone. The

combination of the length, 8 degree convergence angle at 6 atm results in a thrust

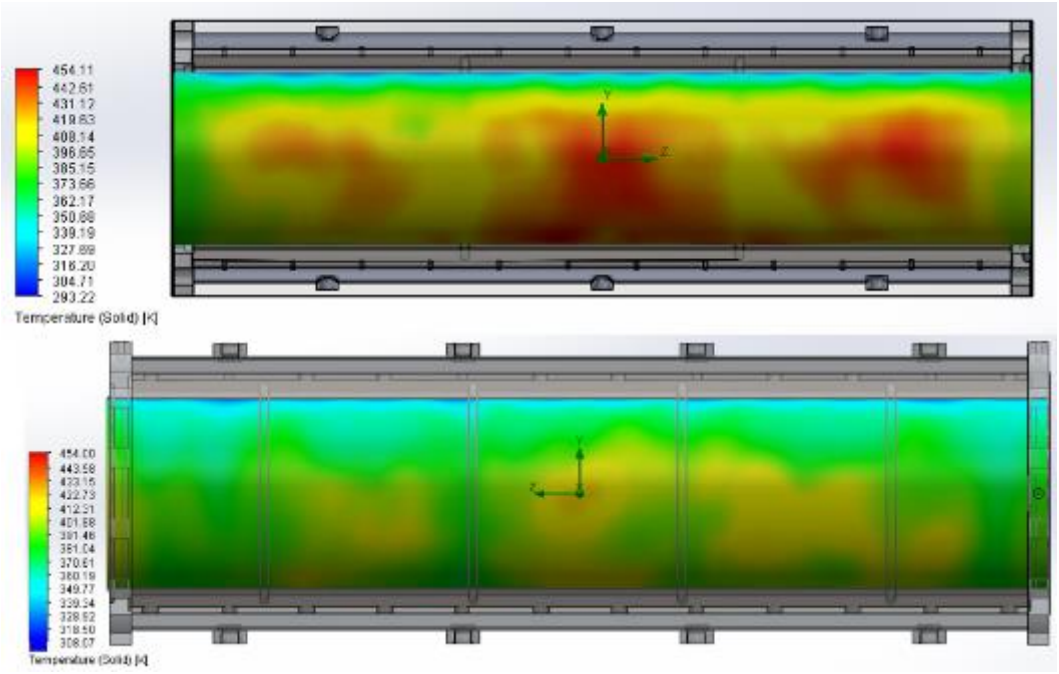

Figure 6.22: Surface Plot Comparison of initial and Final Fully-catalytic Flow Simulation.

loading condition of more than twice the other segments, even at higher pressures. As such, the only segment that was simulated within the time constraints was the catch cone. The simulation setup follows that of the nozzle, and the resultant FEA plot of the catch cone, considering both thermal and pressure loads for the 6 atm case is shown in Figure 6.23. As can be seen in the Figure, the majority of the cone is well below the yield strength of the aluminum, and at maximum the stress of the system is less than 25 ksi, approximately two thirds of the yield strength of the material. Even with consideration to the slight degradation of yield strength with increase in temperature, for aluminum with a temperature rise of approximately 100 K, the yield strength only decreases by 10-15%, resulting in a total Factor of Safety

of at least 1.25. As a result, the worst case scenario is that the simulation sees 1.25 FOS at minimum, so for normal operation the system is considered structurally

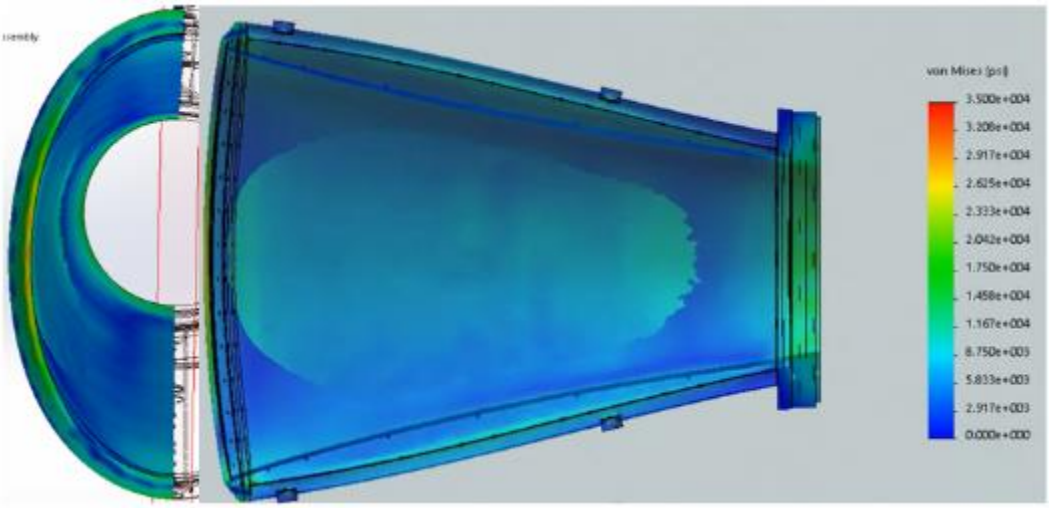

Figure 6.23: FEA results of the Catch Cone shown at 20-times actual deformation.

acceptable. The deformation of the catch cone was also checked to make sure that significant discplacement would not occur, causing possible spillage from the catch cone. The resultant displacement, shown in Figure 6.24, shows that a maximum of 2.6 mm of displacement occurred in the body, stretching into a slightly ovular shape. Due to the inlet diameter being approximately 480 mm, a deformation of less than one half percent was also considered acceptable. Beyond this, the other systems were not structurally examined due to time constraints within design, but the size, angles and temperatures of the segments resulted in the knowledge that the throat segments and exit diffuser segments would result in a lower stress state than the catch cone during operation. As such, the analysis was considered completed

for the diffuser system, and the finalized machine drawings of the system were sent

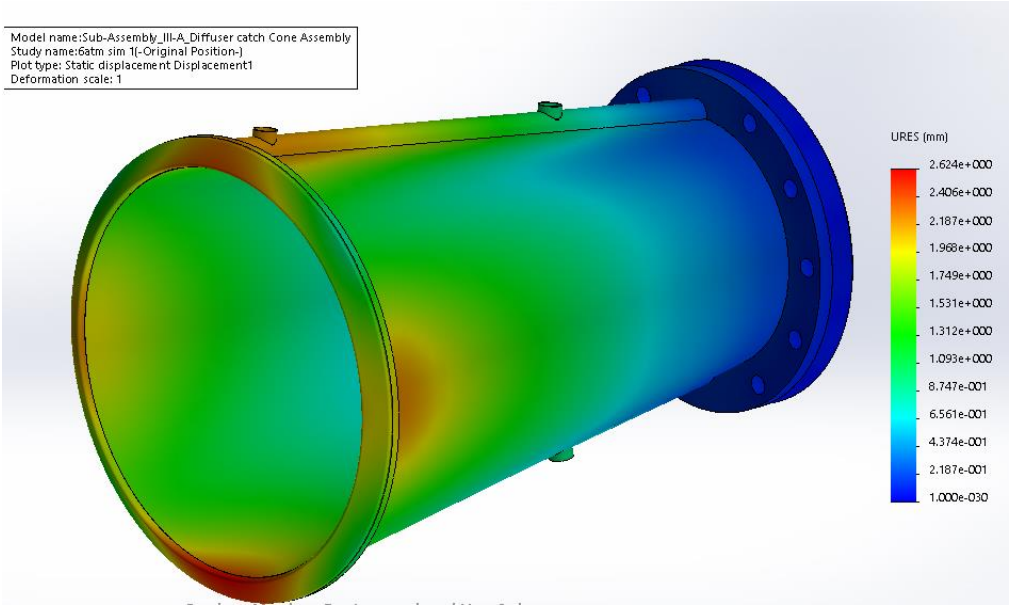

Figure 6.24: Resultant Displacement of the catch cone based upon thermo-structural analysis

out for final quote and manufacturing. The method of centrifugal casting that will be used for the conical segments of the assembly further reduces any structural concerns due to thrust loading, because the internal body along with the flanges for the catch cone and exit segments will be cast as one solid piece, not welded.

Chapter 7

Conclusion

Upon completion of the diffuser analysis, the nozzle and diffuser systems were considered finalized and the machine and assembly drawings were developed and the submitted for manufacturing. The manufacturing drawings of the nozzle and the diffuser included assembly drawings quantifying explicit assembly welding and tolerance criterion, as well as individual part drawings for each component of the system with machining part tolerances and material specifications. The manufacturing of these systems is currently underway. Both the nozzle and the diffuser assemblies will be hydrostatically tested and vacuum tested within the operation limits of the facility. This testing requirement of the system is part of the Purchase Order, insuring the proper manufacturing of the assemblies before delivery.

Upon the completion of all manufacturing of the independent systems for the facility, the assembly of the facility will be commence. Once the full arc-heated facility is assembled, the initial shakedown of the facility will occur. The initial shakedown and subsequent characterization of the facility will be required for full validation of the analysis of the facility systems, both internal flow characteristics and cooling system characteristics. Upon initial operation the flow rates and pressures within the independent fluid lines will be quantified. The temperatures of the independent assemblies will be monitored to verify design constraints used

during the analysis presented in this Thesis. Once confirmation of design constraints has been met for the final system, hypersonic flow testing will commence.

References

[1] “Armstrong Fact Sheet: X-15 hypersonic Research Program”. 28 February, 2014. Online. https://www.nasa.gov/sites/default/files/ec88-0180-1.jpg [Accessed 15 May, 2017].

[2]”X-15 Contributions to the X-10”. Online.URL: https://history.nasa.gov/x15conf/contrib.html [Accessed 15 May, 2017].

[3] Frank Lu and Dan Marren, Ed. “Advanced Hypersonic Test Facilities”, Progress in Astronautics and Aeronautics, Vol. 198. Chapter 2. American Institute of Aeronautics and Astronautics, Reston, VA. 2002.

[4] Carlo Purpura, Eduardo Trifoni and B. Van-Ootegem. “D2.3:Ground Facilities for TPS Qualifications”. CIRA Technical Note CIRA-CF-11-0926, 2011.

[5] Carlo Purpura, Federico De Filippis, Edigio Graps, Eduardo Trifoni and Raffaele Savino, “The GHIBLI plasma wind tunnel: Description of the new CIRA-PWT facility”, *Acta Astronautica*, Vol. 61, pp 331-340, 2007.

[6] Raymond Mitten and Bennie Cocke Jr. “Description and Initial Calibration of the Langley 20-inch Hypersonic Arc-Heated tunnel”. NASA Technical Note NASA-TN-D-4653, 1963.

[7] Jennifer Inman, Brett Bathel, Craig Johansen, Paul Danehy, Stephen Jones, Jeffrey Gragg, and Scott Splinter. "Nitric Oxide PLIF Measurements in the Hypersonic Materials Environmental Test System (HYMETS)", *49th AIAA Aerospace Sciences Meeting*, Orlando, Florida, 4-7 January, 2011.(2011-1090)

[8] Stefano Gulli, Cody Ground, Matthew Crisanti, and Luca Maddalena. "Teflon Probing for the Flow Characterization of the 1.6MW Arc-Heated Wind Tunnel of the University of Texas at Arlington", *51st AIAA Aerospace Sciences Meeting,* Grapevine, TX, 7-10 January, 2013.(2013-0273)

[9] Cody Ground, Luca Maddalena, and Valerio Viti, "Computational Analysis and Characterization of the UTA 1.6 MW Arc-Heated Wind Tunnel Facility", *51st AIAA Aerospace Sciences Meeting,* Grapevine, TX, 7-10 January, 2013. (2013-0907).

[10] Chris Roseberry, “Arc-heated Gas Flow Experiments for Hypersonic Propulsion Applications,” Doctoral Dissertation, Department of Mechanical and Aerospace Engineering, The University of Texas at Arlington, Arlington, TX, 2005.

[11] “Technical Reference, Solidworks Flow Simulation 2015”. Dassault Systems, 2015. Included with Software Package.

[12] “Advanced Boundary Cartesian Meshing Technology in Solidworks Flow Simulation”. GoEngineer. Online. URL: http://www.goengineer.com/wp-content/uploads/2014/04/Enhanced-Boundary-Cartesian-Meshing-Technology-in-SolidWorks-Flow-Simulation.pdf [Accessed 9 May, 2017].

[13] Automation Creations, Inc. (2009). *MatWeb, Your Source for Materials Information* ,URL: http://www.matweb.com/. [Accessed 5 May, 2017].

[14] Arvel Witte and Edward Harper, “Experimental Investigation of Heat Transfer Rates in Rocket Thrust Chamber”, *AIAA Journal*, Vol.1, No.2. February 1963.

[15] Andrew J. Brune, Serhat Hosder, David Campbell, Stefano Gulli, and Luca Maddalena, "Numerical Analysis of an Actively-Cooled Low-Reynolds Number Hypersonic Diffuser", *21st AIAA International Space Planes and Hypersonics Technologies Conference*, Xiamen, China, 6-9 March, 2017. (AIAA 2017-2363)

Biographical Information

David Campbell is an aerospace engineer with focuses in hypersonic analysis, conjugate heat transfer, thermo-structural analysis and manufacturing. His goal for the future is to take part in progressing mankind beyond this planet, specifically in sending humans to Mars.

David Campbell started his undergraduate career at the University of Texas at Austin in Aerospace Engineering. While he had significant interest in the topics, family obligations, employment and distractions resulting in academic struggles. After taking some time off, he made the decision to move to finish his undergraduate career and transferred to the University of Texas at Arlington. He excelled in coursework and found himself wanting for intellectual challenges. He joined the Formula Society of Automotive Engineering team, UTA Racing, and learned about design, analysis and manufacturing. After moving up the team structure quickly, he found himself to be the chief engineer and manufacturing lead. At the same time he had begun working at the university's Mechanical and Aerospace Engineering machine shop. An associate professor in Aerospace Engineering at the university approached David about an opportunity to develop a budgetary assembly for a grant proposal for the upgrade to the university arc-heated wind tunnel. He accepted and over four months developed a first order system encompassing the nozzle, test section and diffuser assemblies of the arc-heater facility upgrade. David oversaw the modeling, manufacturing drawings and budgetary quotes for these systems.

Upon completion of the budgetary approximation and grant submission, David continued his undergraduate education and served as the geometry lead and member of the aero-thermal team for a Senior design project to reverse engineer the X-15 and develop a single stage, VTOHL sub-orbital commercial craft. He continued with the UTA Racing team as chief engineer and succeeded at taking the combustion vehicle for competition in placing 12th out of 120 teams. At this time the facility grant was approved, and David immersed himself in the design, conjugate heat transfer and thermo-structural analysis of the nozzle and diffuser for the arc-heater. This project was intense and progressed over two years, while David worked toward and completed his master's degree in Aerospace Engineering. Upon completion of design and analysis, complete assemblies of the nozzle, test section and diffuser were finalized and detailed drawings and a bill of materials was developed for each system for final budget and manufacturing. The facility manufacturing is underway as of this writing.

His future goals are to develop himself in aerodynamic analysis, specifically in hypersonics, and to take part in the final design and analysis of extra-planetary manned systems.